

FREQUENCY AND TIME DOMAIN ANALYSES OF SENSOR  
SIGNALS IN A DRILLING PROCESS AND THEIR  
CORRELATION WITH DRILL WEAR

BY

ALI NOORI-KHAJAVI

Bachelor of Science  
in  
Mechanical Engineering  
Amirkabir University of Technology  
(Tehran Polytechnic)  
1975

Master of Science  
in  
Structural Engineering  
Amirkabir University of Technology  
(Tehran Polytechnic)  
1982

Submitted to the Faculty of the  
Graduate College of the  
Oklahoma State University  
in partial fulfillment of  
the requirements for  
the Degree of  
DOCTOR OF PHILOSOPHY  
December, 1992

SPRINT

Thesis  
1992D  
N818F

FREQUENCY AND TIME DOMAIN ANALYSES OF SENSOR  
SIGNALS IN A DRILLING PROCESS AND THEIR  
CORRELATION WITH DRILL WEAR

Thesis Approved:

*R Komanduri*

Thesis Advisor

*D.A. Lucca*

*J. Ellis*

*Keto A. Tey*

*Thomas C. Collini*

Dean of the Graduate College

**TO  
MY FATHER, MOTHER, AND WIFE  
THANK YOU FOR EVERY THING**

## PREFACE

Single sensors were investigated in the past for their potential for monitoring drill wear. Since, signals from different sensors may capture wear differently at different stages of its life, sensor fusion concept using multiple sensors was advanced recently. In this investigation, this concept was explored in drilling using four sensors, namely, thrust, torque, and strains in the X-direction (along the cutting process) in the Y-direction (perpendicular to the axis of the drill) on the table of a CNC milling machine. The signals were analyzed in the time and frequency domains. In the time domain mean and variance and in the frequency domain power spectral density (PSD) of sensor signals were calculated. For the calculation of PSD periodogram averaging, proposed by Bartlett and improved by Welch, was used. All sensor signals were sampled during the period when the industry recommended cutting speed and feed were used. For accelerating drill wear, the cutting speed was increased to twice the recommend speed.

The Power Spectral Density (PSD) of sensor signals showed good correlation with drill wear while in the time domain no significant changes in mean and variance of sensor signals between a sharp and worn tool were found. Normalized PSD diagrams of each sensor signal indicated that the parameters of the drilling process did not change and the only parameter that might change was the gain of the system. Also, the signal-to-noise ratio analyses in the frequency domain at different states of drill wear indicated that as the drill wear increases the noise also increases. Three pattern classification techniques used in neural networks, namely, clustering, mapping, and decision surfaces were examined. It was shown that when noisy sensor signals were integrated (instead of using one sensor signal), using a neural network based the above techniques, it may actually result in the

deterioration of the correct classification or estimation of drill wear. Consequently, it appears that integration of the sensor signals under these conditions may not be appropriate and/or advantageous.

I wish to express my sincere appreciation to all people who assisted me in this research. In particular, I would like to thank my advisor Professor R. Komanduri, without whose help, guidance and encouragement this research would not have been possible. I am also thankful to my committee members Professors D. A. Lucca, E.A. Misawa, and K. Teague and my very close friend Dr. Shiraishi of Ibaraki university in Japan, for constantly providing help during this project. The help rendered by Mr. Mouli and Mr. Panneerselvam is gratefully acknowledged. Lastly I would like to thank my parents and my wife for their understanding and patience.

The project was supported by a grant from the Oklahoma Center for Integrated Design and Manufacturing (OCIDM). The author is grateful for this support.

## TABLE OF CONTENTS

Chapter	Page
I. INTRODUCTION.....	1
II. LITERATURE REVIEW OF THE DRILLING PROCESS.....	7
2.1 Cutting Process in Drilling.....	7
2.2 Drilling Geometry.....	11
2.3 Drill Wear and Failure.....	16
2.3.1 Drill Wear.....	16
2.3.2 Temperature Distribution Along the Cutting Edge.....	22
2.3.3 Drill Wear Mechanisms.....	24
2.4 Monitoring of the Drilling Process.....	26
2.5 Sensor Integration Approaches to Tool Wear Monitoring.....	38
2.6 Problem Definition.....	44
III. REVIEW OF PARAMETER ESTIMATION AND PATTERN RECOGNITION AND THEIR APPLICATION TO METAL CUTTING....	46
3.1 Parameter Estimation.....	48
3.2 Pattern Recognition.....	49
3.2.1 Clustering Technique (Nearest Neighbor Classifier).....	50
3.2.2 ART 2 Neural Network.....	51
3.2.3 Kohonen's Self Organizing Maps.....	56
3.2.4 Back Propagation (BP) Neural Network (Multi-layer Perceptron).....	59
3.2.4.1 Function Approximation Using Multi-layer Perceptron.....	64
3.3 Application of Pattern Recognition in Tool Wear Monitoring.....	64
3.3.1 Classification Using Clustering Technique.....	65
3.3.2 Classification Using Mapping Technique.....	67
3.3.3 Classification Using Decision Surfaces.....	67
3.4 Tool Wear Estimation Using Mapping Technique.....	70
3.5 Conclusions.....	72
IV. REVIEW OF SIGNAL ANALYSIS.....	73
4.1 Spectral Estimation.....	73
4.2 Mean and Variance of Periodogram.....	77
4.3 Data Windowing.....	82
4.4 Smoothing the Periodogram.....	88
4.4.1 Welch Method.....	91

Chapter	Page
4.5 Conclusions.....	92
V. EXPERIMENTAL WORK AND DATA PROCESSING.....	94
5.1 Experimental Setup.....	94
5.1.1 Block Diagram of the Experimental Setup.....	99
5.2 Experiment Strategy.....	101
5.3 Vibration Analysis of the Experimental Setup.....	106
5.4 Analysis of Sensor Signals in the Time Domain.....	108
5.5 Analysis of the Sensor Signals in the Frequency Domain.....	108
5.6 Correlation of Wear With the Area Under the PSD Plots.....	135
5.7 Conclusions.....	141
VI. INVESTIGATION OF SENSOR INTEGRATION TECHNIQUE USING THE RESULTS OF THIS STUDY.....	143
6.1 Necessity of Application of Sensor Integration.....	145
6.2 Possibility of Using Mapping Technique for Drill Wear Evaluation.....	145
6.3 Possibility of Using Clustering, Decision Surfaces, and Mapping Techniques for Drill Wear Classification.....	169
6.4 Reevaluation of Some Previous Works on Sensor Integration Using Neural Networks.....	172
6.5 Conclusions.....	176
VII. CONCLUSIONS.....	177
7.1 Drill Wear.....	177
7.2 Correlation of the Sensor Signals With Total Corner Wear of the Drill.....	178
7.3 Parameters of the System.....	179
7.4 Sensor Integration.....	180
VIII. FUTURE WORK.....	182
8.1 Characteristics of the Actual Cutting Speed and Feed in the Time and Frequency Domains.....	182
8.2 Transfer Function of the Drilling Process.....	182
8.3 Drill Wear Pattern at Recommended Cutting Conditions.....	183
8.4 Monitoring Sensor Signals at Conventional Drilling Speed.....	184
REFERENCES.....	185
APPENDIX - EQUIPMENT SPECIFICATIONS.....	190



## LIST OF TABLES

Table	Page
3.1 Training Data Set.....	66

## LIST OF FIGURES

Figure	Page
2.1 Twist Drill Geometrical Specification [26].....	9
2.2 Schematic of Orthogonal Machining [27].....	10
2.3 Geometrical Parameters of Oblique Cutting [1].....	12
2.4 Variation of Drill Angles Along the Cutting Edge [26].....	14
2.5 Chip Formation in Drilling [26].....	15
2.6 Variation of Chip-Flow Angle with Angle of Obliquity for Drilling [26].....	15
2.7 Schematic of the Areas Where Tool Wear Commonly Occurs in Orthogonal Cutting [28].....	17
2.8 Characteristics of the Development of Wear With Cutting Time [1].....	18
2.9 Various Types of Drill Wear [18].....	20
2.10 Drill Wear at Margin [20,21].....	21
2.11 Temperature Distribution Obtained From Microhardness Method at the Corner of Drill [19].....	23
2.12 Temperature Distribution Obtained From Microstructural Change Method at the Corner of Drill. Drill material M33 [19].....	25
2.13 Histogram of Drill Life for 70 Drill Bits (0.3 mm Corner Wear) [18].....	27
2.14 Wear Results for Drilling Cast Iron With a 7.94 mm (5/16 inch) Drill Curve A Gives Radioactivity Measurements, Curve B the Optical Measurements [31].....	29
2.15 Repeatability of Flank Wear with Number of Holes Drilled [31].....	29
2.16 Flank Wear Versus the Number of Holes Drilled [6].....	31
2.17 Thrust Force Versus the Number of Holes Drilled [6].....	31
2.18 Torque Versus the Number of Holes Drilled [6].....	32

Figure	Page
2.19 Power Versus the Number of Holes Drilled [32].....	31
2.20 Plot of Drill Wear Versus the Number of Holes [32].....	34
2.21 Signature Waveform Pattern for a Sharp Drill [32].....	35
2.22 Signature Waveform Pattern for a Worn Drill [32].....	35
3.1 Classification of Patterns by Nearest Neighbor Concept (Clustering Technique) [49].....	53
3.2 Effect of the Threshold on Cluster Arrangements [49] .....	57
3.3 Major Components of ART2 Neural Network [53].....	55
3.4 Function of ART2 Neural Network for two Different Values of Vigilance Parameter a) $\rho = 0.95$ , b) $\rho = 0$ [50].....	57
3.5 Two Dimensional Array of Output Nodes Used to Form Feature Maps [44].....	58
3.6 Topological Neighborhoods at Different Times as Feature Maps are Formed [44].....	58
3.7 Four Frames for a Kohonen Self-organizing map Neural Network [55].....	60
3.8 Multi-layer BP Neural Network [54].....	61
3.9 Types of Decision Regions That can be Formed by Single- and Multi-Layer BP Neural Networks With one and two Layers of Hidden Units and two Inputs [44].....	63
3.10 Classification of Sensor Signals Based on Clustering Technique.....	66
3.11 Classification of Sensor Signals Based on Mapping Technique.....	68
3.12 BP Network Structure for Classification of Sensor Signals Using Decision Surfaces Technique.....	69
3.13 Modeling $w = f(T,M)$ .....	71
4.1 $x(t)$ and $x(t+\tau)$ Signals [56].....	75
4.2 Illustration of Fourier Analysis of Windowed Cosines with Rectangular Window [57].....	83

Figure	Page
4.3 Commonly Used Windows [57].....	86
4.4 Fourier Transforms (Log Magnitude) of Windows of Figure 4.3 [57].....	87
4.5 Data Segmentation for Periodogram Averaging [58].....	89
5.1 Experimental Drilling Setup.....	95
5.2 Sensor Signals From the Beginning to the end of Cutting Hole No. 2 of Drill AK.....	97
5.3 Block Diagram of the Experimental Setup.....	100
5.4 Plot of Wear vs. the Hole No. for Drill BL.....	103
5.5a SEM Photograph at Different Stages of Wear for Side A of Drill BL.....	104
5.5b SEM Photograph at Different Stages of Wear for Side B of Drill BL.....	105
5.6 Mean of Sensor Signals in the Time Domain for Drill BL.....	109
5.7 Variance of Sensor Signals in the Time Domain for Drill BL.....	111
5.8 Estimate of PSD of Sensor Signals of Hole No. 200 for Dill AR.....	114
5.9 Estimate of PSD of Sensor Signals Over 40 Holes (From Hole No. 200.to Hole No. 239) for Drill AR.....	116
5.10 Signal-to-Noise Ratio of Sensor Signals in the Frequency domain over 40 Holes (From Hole No. 200.to Hole No. 239) for Drill AR.....	119
5.11a Estimate of PSD of Sensor Signals Over a Number of Holes at the Same State of Drill Wear. (1) Set 1: From Hole No. 11 to 40, (2) Set 2: From Hole No. 41 to 80, (3) Set 3: From Hole No. 81 to 110, for Drill BL.....	123
5.11b Estimate of PSD of Sensor Signals Over Number of Holes at the Same State of Drill Wear. (1) Set 4: From Hole No. 121 to 150, (2) Set 5: From Hole No. 151 to 190, (3) Set 6: From Hole No. 191 to 220, for Drill BL.....	125
5.11c Estimate of PSD of Sensor Signals Over Number of Holes at the Same State of Drill Wear. (1) Set 7: From Hole No. 231 to 260, (2) Set 8: From Hole No. 261 to 300, (3) Set 9: From Hole No. 301 to 330, for Drill BL.....	127

Figure	Page
5.12 Estimate of PSD of Sensor Signals Over Number of Holes at Different States of Drill Wear. (1) Set 2: From Hole No. 41 to 80, (2) Set 5: From Hole No. 151 to 190, (3) Set 8: From Hole No. 261 to 300, for Drill BL.....	130
5.13 Calculation of the Area Under the PSD Using Trapezoidal Method.....	132
5.14 Normalized PSD (Frequency Range 20 to 380 Hz) of Sensor Signals Over Number of Holes at Different States of Drill Wear. (1) Set 2: From Hole No. 41 to 80, (2) Set 5: From Hole No. 151 to 190, (3) Set 8: From Hole No. 261 to 300, for Drill BL.....	134
5.15 Schematic of a Sharp and a Worn Drill bit.....	137
5.16 Plot of Wear Area vs. Change of Area Under the PSD for Drills BL, BO, BP and BQ.....	139
6.1a Signal-to-Noise Ratio of the Sensor Signals in the Frequency Domain Over 40 Holes (From Hole No. 41 to Hole No. 80), Corner Wear: 0.076 mm <sup>2</sup> , for Drill BL.....	146
6.1b Signal-to-Noise Ratio of the Sensor Signals in the Frequency Domain Over 40 Holes (From Hole No. 151 to Hole No. 190), Corner Wear: 0.28 mm <sup>2</sup> , for Drill BL.....	148
6.1c Signal-to-Noise Ratio of the Sensor Signals in the Frequency Domain Over 40 Holes (From Hole No. 261 to Hole No. 300), Corner Wear: 0.43 mm <sup>2</sup> , for Drill BL.....	150
6.2 Cross Correlation of the Estimate of Power of Sensor Signals Between 0 and 425 Hz, for Holes From 240 to 279, For Drill BO.....	153
6.3 Cross Correlation of Sensor Signals in Time Domain Between Holes 240 to 264 for Drill BO.....	158
6.4 2×2×1 BP Neural Network Used for the Computer Simulation of Equations 6.6a and 6.6b.....	166
6.5a Simulation of Equations 6.4a and 6.4b Using 2×2×1 BP Neural Network for Training Data Set.....	167
6.5b Simulation of Equations 6.4a and 6.4b Using 2×2×1 BP Neural Network for Testing Data Set.....	168

6.6 Two Dimensional Distributions of the Estimate of Power of Thrust Signal at 121.1 Hz and the Estimate of Power of Torque at 101.6 Hz for Each Hole of Set 1, Set 4, and Set 7 of Drill BL Shown in Figure 5.4.....	170
---	-----

## CHAPTER I

### INTRODUCTION

Metal cutting is one of the most important manufacturing processes. Its importance can be realized when one considers the total share of this activity in the national economy. In the United States, the yearly cost associated with the material removal process has been estimated at about 10% of total gross national product (GNP) [1]. According to Metcut Research Associates [2], the total annual labor and overhead costs of operating metal cutting machine tools in the United States, in 1984, was estimated to be approximately 125 billion dollars. To reduce these costs considerable efforts have been centered around automation of the metal cutting processes in the United States as well as in other countries.

The traditional symbol of automation is mechanized transfer line. Chronologically, this was the first example of automated production to appear. Its origins can be traced largely to the work of Henry Ford in the manufacture of automobiles. In his efforts to improve the methods of automobile manufacture for reduced cost, he achieved such significant advances in assembly line mass-production techniques that the feasibility and potential of these methods were not only demonstrated but became a model to the rest of the industry. This in turn, led to subsequent developments of fully automated transfer lines.

After the introduction of digital computers to manufacturing processes, new terms, like numerical control (NC), computer aided manufacturing (CAM) became a common usage to describe automation technology. Old words, such as mechanization have virtually disappeared from the technical vocabulary. Modern definition of automation, according to Groover [3] is the technology concerned with the application of complex mechanical, electronic, and computer-based systems in the operation and control of production.

Application of digital computer to metal cutting operations dates back to 1952, when the first NC machine tool was introduced [4]. Since then, the cost of microprocessors has decreased dramatically at the same time their computational power has increased significantly. In addition, the development of powerful but small size DC motors, led to in the reduction in the size of CNC machine tools. Inexpensive but powerful microprocessors and DC motors have contributed toward the development of industrial robots also. A combination of CNC machine tools, industrial robots, and other necessary automated systems has created a new production system known as flexible manufacturing systems (FMS). Although, the primary objective of FMS is batch production, advancements in this area can lead to economical mass-production of mechanical parts, which are produced by the traditional transfer lines.

Probably the biggest obstacle in the path of successful FMS is its dependence on unattended machining. FMS provides flexible automation for the production of different parts i. e., it is aimed at handling manufacturing of small lot, random shaped parts. Such a manufacturing practice can involve many unexpected problems, such as, random breakage of tools that hamper attempts at untended machining. Lack of adequate solutions to these problems are due to inadequate knowledge regarding the cutting process. In fact, we are far from a quantitative description of the complex machining process since the introduction of a theoretical model by Merchant some fifty years ago. Even today, the basic theory developed by Merchant [5] is invoked while addressing the cutting process.

Tool wear and tool breakage, for example, are some of the important aspects of the cutting process that are not well understood. The extent of tool wear has a strong effect on the surface finish and dimensional accuracy of the workpiece as well as on the machine tool vibration. Tool wear may lead to catastrophic failure of the tool as a result of high forces and this may finally damage the machine tool itself. Therefore, accurate monitoring of the tool condition and identification of the state of tool wear are important problems in machining, solutions to which can prevent unexpected events. Information regarding tool



condition is very important for a decision making system. The decision making system may be designed to optimize the cutting process by maximizing the metal removal rate (MRR) and minimizing the machine downtime (nonproductive time of machine). Downtime of a typical transfer line is about 25 to 35% of the total available time for production. Down time due to tool failure is estimated at a third of the total downtime [6].

In unmanned machining systems, the knowledge-base of an experienced human operator is transferred to a computer that monitors and controls the process. Sensors are devices that provide the required information regarding the ongoing process for a computerized monitoring system. Sensors, on one hand, should be accurate enough to gather reliable information and on the other be rugged enough to withstand harsh machining environment. The machine tool monitoring and control system must be able to interpret the received information and identify the relation between the sensor signals and such parameters as tool wear and breakage, surface finish, state of vibration etc. Success with such unmanned machining will depend to a large extent on the development of machine tool monitoring and control system involving adequate sensory devices [7].

Tool failure is a sudden event, which needs to be forecasted sufficiently in advance, so as to prevent any major damage to the workpiece and even to the machine tool. In contrast, tool wear is a slowly evolving phenomenon, and can be detected and identified by one or more sensor signals. For example, force, accelerometer, and acoustic emission (AE) sensors are some of the common sensors that have been investigated for monitoring the cutting process. Excellent reviews of tool wear sensors can be found in Micheletti [8] and Tlusty et al [9]. In the literature, the sensor signals are correlated more to the secondary parameters, such as shear-plane angle, chip-tool contact length, effective friction coefficient over the chip-tool contact area, the chip width etc. These parameters in turn are related to primary parameters, such as cutting speed, feed rate, and depth of cut using simple analytical models (for example, Merchant's [5] model). Due to the difficulties involved in the cause and effect relationships, no sufficiently accurate model was developed

thus far that enables the identification of the nature and location of the tool wear from a sensor signal.

The complexity of the machining process and the lack of sufficiently accurate model have led many researchers to seek alternate methods, such as pattern recognition techniques or artificial neural networks. Artificial neural networks mimic the computational architecture of a human brain in a crude way with a prespecified structure, have been successful in modeling many systems. Similar to a human brain, artificial neural network can receive signals from different sources (sensors). It is expected that this technique can integrate different sensor signals, remove irrelevant information, and use the most correlated ones during the learning process, similar to a human brain. The effort was aimed at investigating the feasibility of an artificial neural network to represent relationships between sensor signals and tool wear, surface finish, and component of cutting forces in turning. A hierarchically structured artificial neural network is commonly used to establish these relationships.

Kannatey-Asibu [10] explored the possibility of using pattern recognition technique for monitoring the condition of the tool in a cutting operation using acoustic emission sensing as a specific example. Dornfeld and Pan [11] used the event rate of the RMS of an AE signal along with the feed rate and cutting velocity in order to provide a decision on the chip form produced during a turning operation. Emel and Kannaty-Asibu [12, 13] used spectral features of an AE signal to classify fresh and worn tools. Back-propagation type neural network was used by Rangwala and Dornfeld [14, 15] for the classification of tool wear. Selected bands of the force and AE spectrum were used as inputs to the network and a high level of accuracy was reported in detecting tool wear.

Drilling is a common metal cutting operation. Estimates show that drilling accounts for nearly 40% of all the metal removal operations in the aerospace industry [16]. Drilling operation is conducted on a wide variety of machine tools including drilling machines, machining centers, milling machines, turning machines, and boring machines. Downtime

due to drill breakage is critical in the economics of the drilling operation. Breakage of a drill inside a hole can result in the part being rejected or in costly repair.

The objective of this investigation is to analyze the correlation between the four sensor signals, namely, thrust, torque, and strains on the machine table in the cutting direction (X-direction) and perpendicular to axis of the drill (Y-direction), in both frequency and time domains. Background information on the drilling process is presented in Chapter II. This includes the development of the relationships between various angles of the drill and the drilling parameters by comparing drilling process to oblique cutting. Review of literature, chiefly that of Soderberg et al [17], Kanai and Kanda [18] and Thangaraj and Wright [19], indicates that corner (margin) wear is the best criterion for monitoring drill wear and life. A review various techniques for monitoring drilling in particular and other cutting processes in general is also given in this chapter.

In Chapter III, a review of the parameter estimation and pattern recognition and their application to metal cutting is given. The neural network techniques used for pattern recognition proposes are classified into the following three categories. They are: pattern classification using mapping, clustering, and decision surfaces techniques.

A theoretical review of spectral estimation is given in Chapter IV. Periodogram, which is the square of the absolute of the Fourier transform, is a biased estimate of power spectral density (PSD) and its variance at each frequency is of the same order as its mean at the same frequency. It was shown that variance at each frequency may be reduced using either Bartlette or Welch methods.

In Chapter V experimental results of this investigation are presented. Sensor signals in the time domain did not show good correlation with drill wear. PSD of the sensor signals for all four sensor signals as well as the signal to noise ratio at each frequency are all calculated. The frequencies with maximum signal-to-noise ratio were selected. PSD of three sensor signals, thrust, torque, and strain in the X-direction

independently showed good correlation with drill wear. The correlation between strain in the Y-direction and tool wear was not as good as the other sensor signals.

Chapter VI deals with sensor integration techniques. It was shown that in the frequency domain, any two frequencies from one sensor or between two different sensors are uncorrelated. Signal to noise ratio analysis showed that noise increases with increase in drill wear. The integration of these uncorrelated noisy signals was investigated and concluded that sensor integration results in the deterioration of the drill wear estimation under the conditions of testing used.

## CHAPTER II

### LITERATURE REVIEW OF THE DRILLING PROCESS

The performance of a cutting tool is determined by the intensity of wear experienced by the tool in the removal of a certain amount of the work material within a given time. Hence, in order to determine the tool performance, it is necessary to monitor its wear while cutting is in progress. A reliable method of tool wear estimation/tool failure prediction is necessary, if damage to the machine and parts is to be avoided. Moreover, in an unattended machining environment, an effective control scheme or a monitoring strategy is necessary in the optimization of cutting conditions and in the prediction of the failure under a given set of operating conditions.

In recent years, research towards an understanding of the drilling process has established useful drill wear criteria [17, 18, 20, 21]. However, direct measurement of drill wear is not possible while cutting is in progress because the tool surfaces that are wearing out are hidden either by the workpiece or by the chip that is being produced. So, researchers have resorted to indirect means of measurement. Factors that are associated with the process, such as cutting forces, vibration, sound etc. have been used in the monitoring of drill wear [6, 22, 23, 24] with limited success.

#### 2.1 Cutting Process in Drilling

Drilling is a metal removal process for producing holes in components. The process involves feeding a rotating cutting tool along its axis into a stationary workpiece. A circular hole is therefore generated in the workpiece. The feed velocity (or feed rate) is usually small compared to the peripheral velocity of the drill. While precision work can be

conducted using a drill under very specified conditions, drilling is generally considered a roughing operation and the primary items of interest are usually long life and high penetration rate. In many, cases drilling is a preliminary operation to reaming, boring or grinding where final finishing and sizing takes place.

Figure 2.1 gives the geometrical specification of a twist drill. Cutting occurs on the straight edges (lips) and on the chisel edge at the tip of the drill. Distance between the straight cutting edges, called the web thickness, is necessary to protect the drill point and to stiffen the drill. The chips generated at the cutting edge travel up the drill axis along the flutes. It is important to realize that no cutting occurs at the drill periphery, except near the outer corner, which corresponds to the secondary or end cutting edge of a lathe tool. In order to reduce frictional forces between the drill and the hole, the drill diameter is decreased over a portion of its circumference leaving a short *land* or *margin* at the full diameter to support the drill against the hole. It is also found necessary to slightly reduce the diameter along the length of the drill to give further clearance. The point angle may be compared to the side cutting edge angle of a lathe tool, since it gives the drill gradual entry into the work, influences the chip-flow direction (with respect to the work), and alters the forces on the cutting edges. The drill flank is comparable to the clearance face of a single-point tool. The helix angle is an important variable which controls the slope of the drill face. If too large a helix angle is used the cutting edge can be weakened. It is, thus seen that the drill consists of the usual cutting elements although it is vastly different in appearance.

Since drilling is a complex three dimensional cutting process some researchers have simplified the drilling process to either orthogonal cutting [6] or oblique cutting [25]. In orthogonal cutting, the direction of relative motion between the tool and the workpiece is at right angle to the cutting edge of a wedge-shaped tool. Such a simple model of cutting is shown in Figure 2.2.

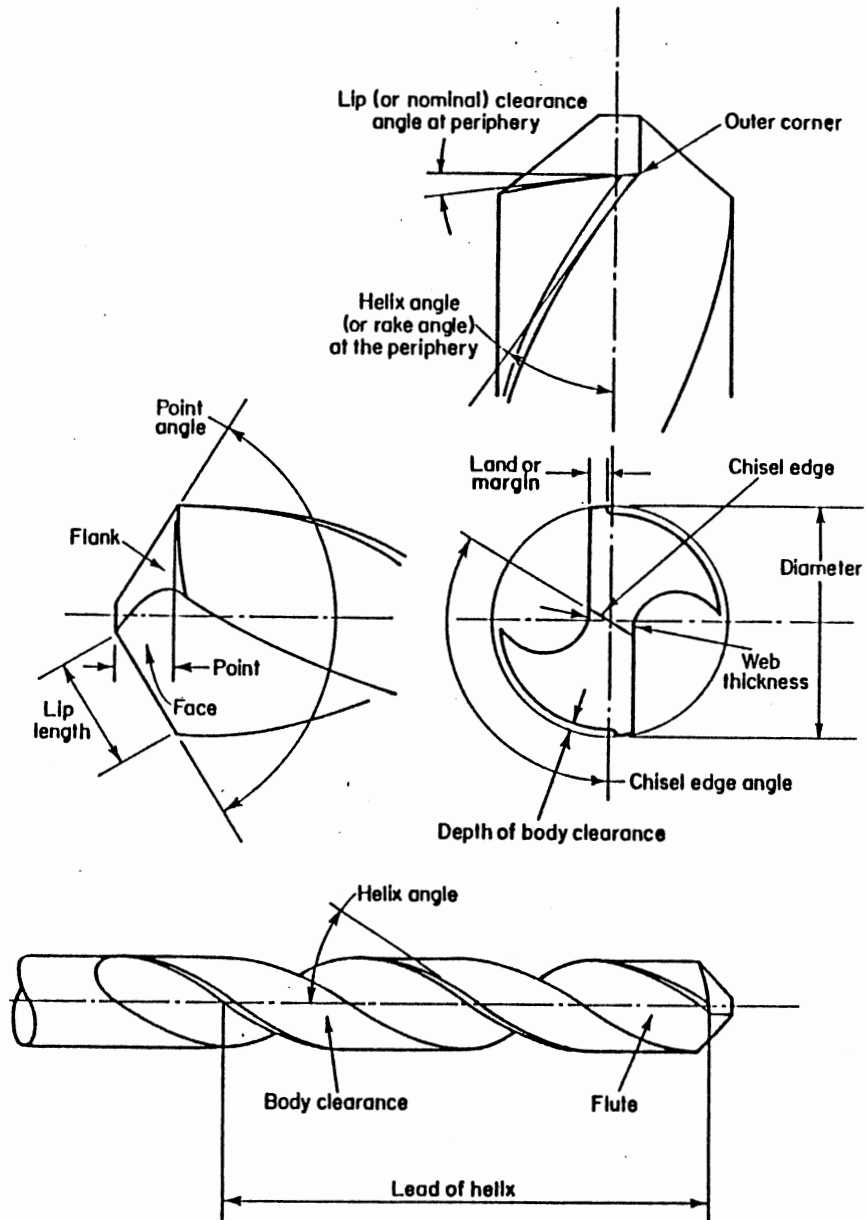


Figure 2.1 Twist Drill Geometrical Specification [26].

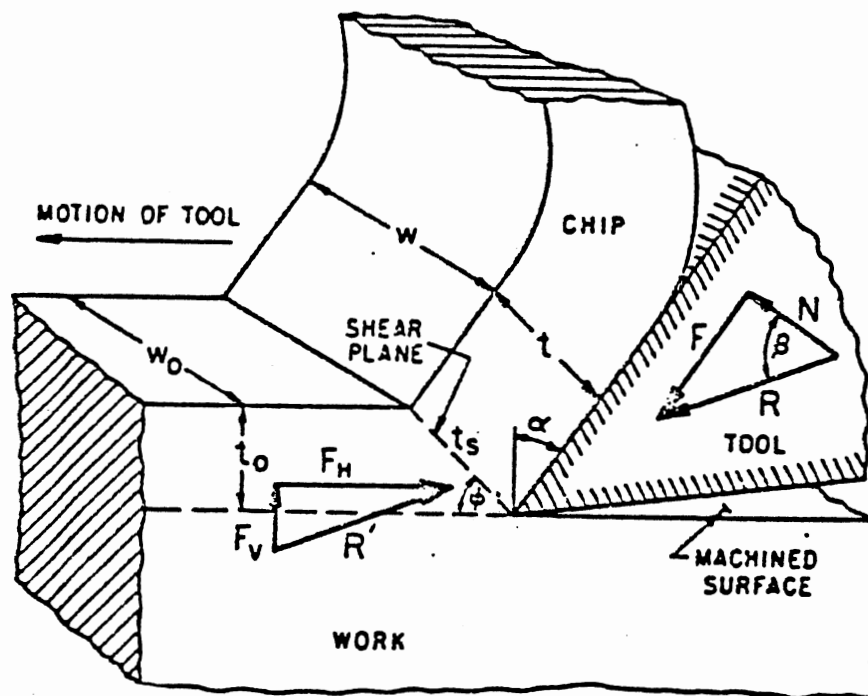


Figure 2.2 Schematic of Orthogonal Machining [27].



In oblique cutting, cutting edge is inclined to the velocity vector (Figure 2.3). Inclination significantly alters the chip flow direction and hence the performance of a tool. The effective rake angle  $\alpha_e$ , is a function of the geometry of the cutting tool and the direction of chip flow. In the next section geometry, of drill bit with respect to oblique cutting is presented.

## 2.2 Drilling Geometry

The important parameters of a drill are the following: diameter  $d$  ( $d = 2r$ ), helix angle  $\gamma_o$  (helix angle at outside diameter), point angle 'p', and web thickness 'W'. In this section relation between various angles at each point on the cutting edge and the drilling parameters is shown and the drilling process compared with oblique cutting. Helix angle is not constant along the radius of the drill and may be calculated as follows [26]

$$\tan \gamma = 2\pi rL \quad (2.1)$$

where  $L$  is the lead of the helix angle which is constant for a given drill. Therefore

$$\tan \gamma = (r/R)\tan \gamma_o \quad (2.2)$$

The nominal clearance angle ' $Cl$ ' is given by

$$\tan Cl = [ \sin \omega - \cos \omega \tan \theta ] \cot p \quad (2.3)$$

$$\text{Where } \sin \omega = W/r \quad (2.4)$$

The clearance at the periphery is denoted by  $Cl_o$ . The normal rake angle  $\alpha_n$  and normal clearance angle  $Cl_n$  are given respectively as

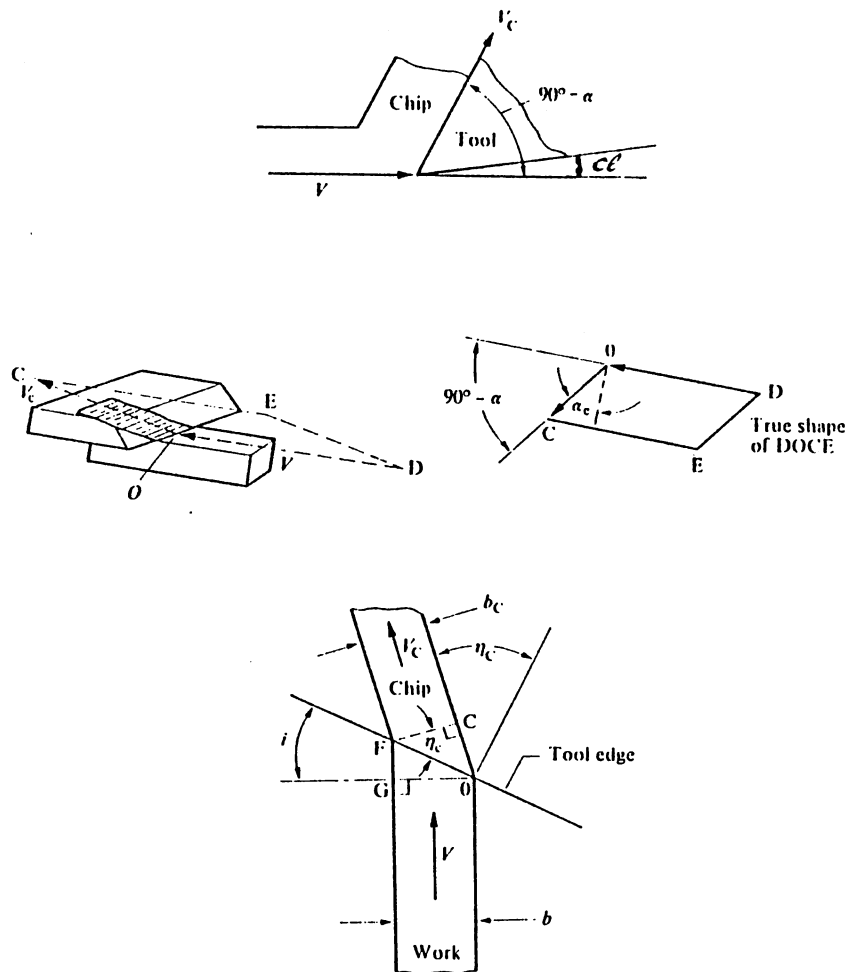


Figure 2.3 Geometrical Parameters of Oblique Cutting [1].

$$\tan \alpha_n = \frac{\tan \delta}{\sin p} [\cos \omega + \sin \omega \tan \omega (\cos p)^2] - \tan \omega \cos p \quad (2.5)$$

$$\tan Cl_n = \frac{\cos p [\sin \omega_1 \tan \omega - (\tan \omega_1 - \tan Cl_o \tan p)]}{\cos \omega_1 + \tan \omega (\cos p)^2 [\tan \omega_1 - \tan Cl_o \tan p]} \quad (2.6)$$

$$\text{where } \sin \omega_1 = W/R \quad (2.7)$$

The angle of inclination is given by

$$\sin i = \sin \omega \sin p \quad (2.8)$$

The variation of drill angles along the cutting edge is shown in Figure 2.4 [26].  $\eta_c$  is the chip flow direction along the rake face as for in oblique cutting.  $\alpha_e$  (equivalent rake angle) can be shown as [26]

$$\sin \alpha_e = \sin i \sin \eta_c + \cos i \cos \eta_c \sin \alpha_n \quad (2.9)$$

In all the above equations the effect of feed velocity is ignored. However, this approximation is generally acceptable [26].

The mechanics of the cutting process in drilling is rather complicated as  $\alpha_e$  and  $i$  change along the cutting edge. Figure 2.5 shows the cutting process along the cutting edge and chisel edge. Along the cutting edge, cutting is similar to conventional cutting while at the chisel edge it is more like an extrusion process. The variation of chip flow angle ( $\eta_c$ ) with respect to the variation of obliquity angle is shown in Figure. 2.6 [26]. This figure shows that  $\eta_c = f(i)$  and deviate from Stabler's rule, i. e.  $\eta_c = i$ . Hence Stabler's rule for drilling is not generally valid.

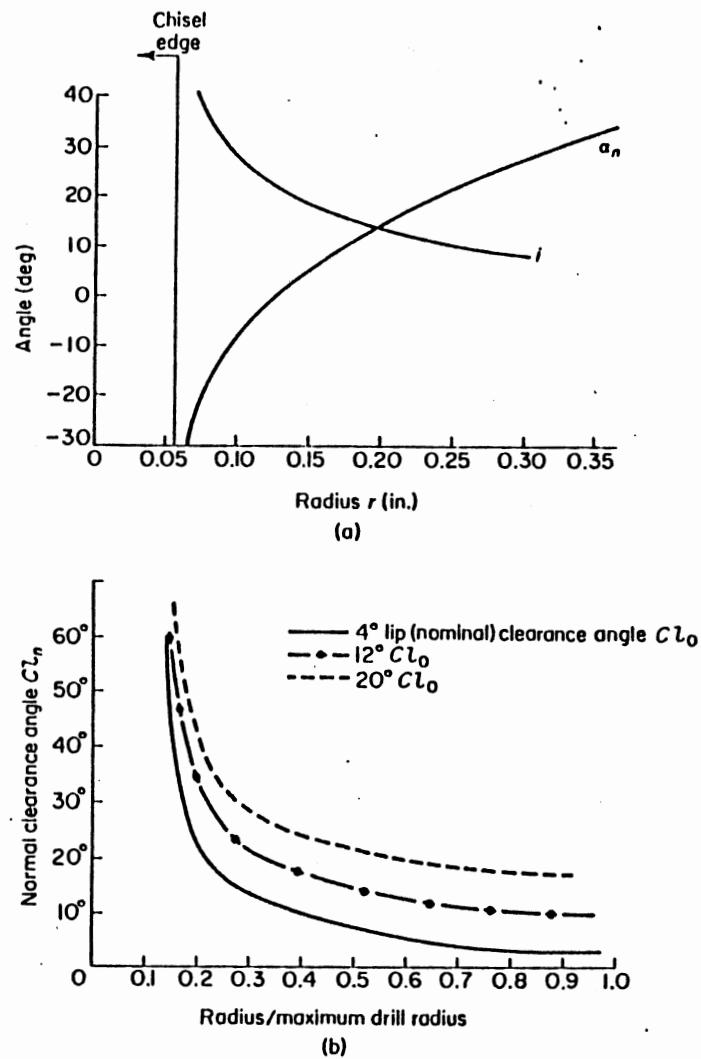


Figure 2.4 Variation of Drill Angles Along the Cutting Edge [26]: (a) Change in normal rake angle and angle of obliquity with radius: drill dia. = 0.75 in.,  $2W = 0.11$  in.,  $2p = 118^\circ$ , standard H.S.S. drill; (b) Change in normal clearance angle with radius and lip (normal) clearance angle.

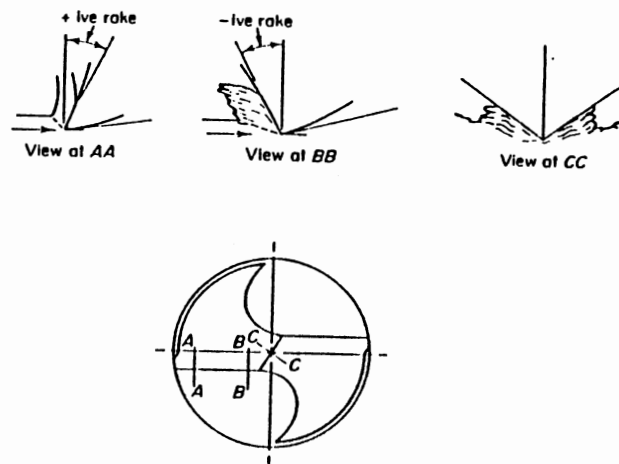


Figure 2.5 Chip Formation in Drilling [26].

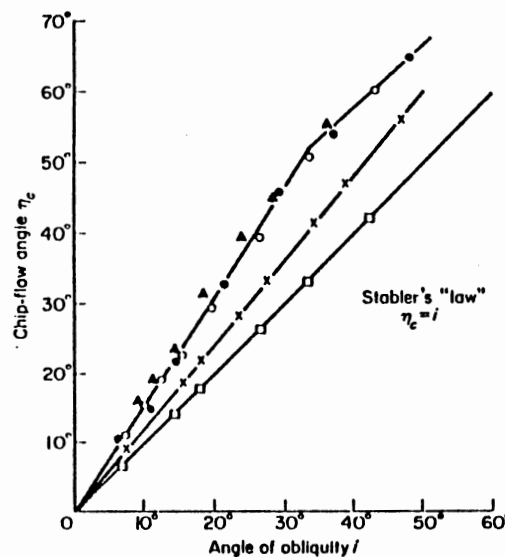


Figure 2.6 Variation of Chip-Flow Angle with Angle of Obliquity for Drilling [26].  
 ▲ = 98° point angle; ○ = 118° point angle; ● = 133° point angle; 3/4 in. drill;  $f = 0.013$  in./rev;  $N = 250$  rpm; work material AISI 3245 steel; fluid,  $\text{CCl}_4$ , x = 133° point angle; 3/4 in. H. D. twist drill;  $f = 0.013$  in./rev;  $N = 250$  rpm; work material, AISI 3245 steel; fluid, soluble oil.  
 □ = 118° point angle, 3/4 in. regular drill;  $f = 0.013$  in./rev;  $N = 200$  rpm; work material, Ti-150A; fluid, sulfurized oil.

The geometry of a typical general purpose drills is given in the following:

Helix angle =  $28^{\circ}$ - $32^{\circ}$                       Clearance angle =  $8^{\circ}$ - $12^{\circ}$

Point angle =  $118^{\circ}$

### 2.3 Drill Wear and Failure

Cutting tools used in metal removal operations perform under extreme conditions of temperature and stress. The inevitable consequence of these harsh conditions which accompany most conventional chip formation is tool wear. Figure 2.7 is a schematic of the areas where tool wear commonly occurs in orthogonal cutting, namely, flank and crater [28].

Wear on a given tool surface generally progresses in a series of three distinct stages as shown in Figure 2.8. During the initial stage, there is a rapid breakdown of the sharp cutting edge due to plastic deformation of the tool material. This is followed by a steady state stage where a nearly uniform wear rate occurs. Finally, in stage III, the presence of a large wear land drastically increases the temperature of the cutting edge causing rapid deterioration of the tool point.

Once the final stage of wear begins, catastrophic failure of the tool is imminent. It is often desirable from a manufacturing standpoint to replace the tool at some point prior to this final stage of wear. As wear progresses to this predetermined level, the tool is said to have reached the end of its useful life.

#### 2.3.1 Drill wear

In drilling, the wear pattern changes along the cutting edge from the margin to the chisel edge due to complex geometry of the drill bit and the cutting process. At the drill point, in addition to the flute (crater wear) and the clearance face (flank wear), the chisel edge and the margin are subject to wear. Kanai and Kanda [18] have classified drill wear into seven types: outer corner wear  $W$ , two types of flank wear  $V_B$  and  $V'_B$ , margin wear

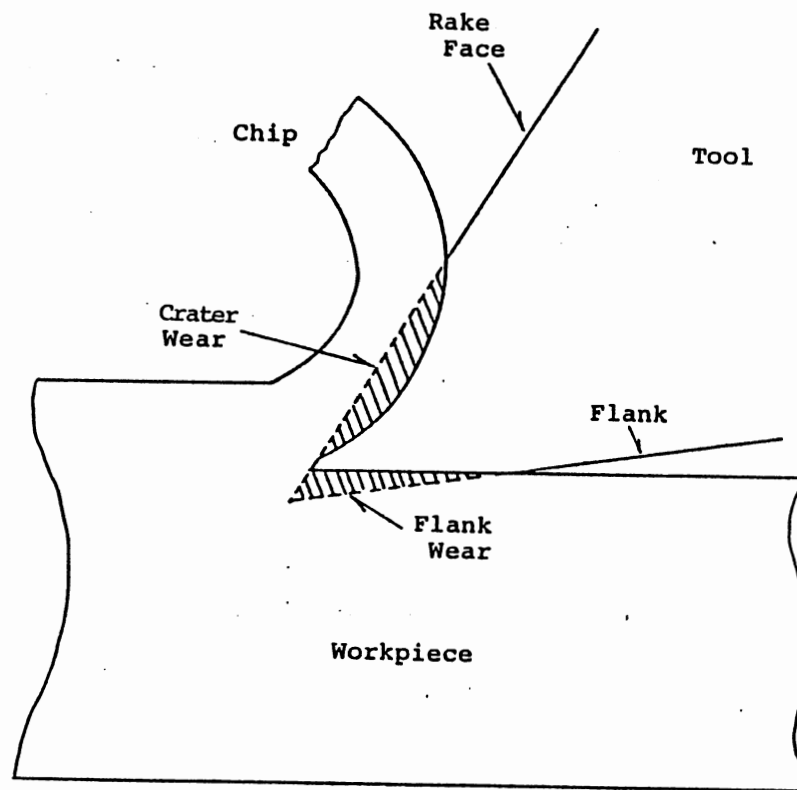


Figure 2.7 Schematic of the Areas Where Tool Wear Commonly Occurs in Orthogonal Cutting [28].

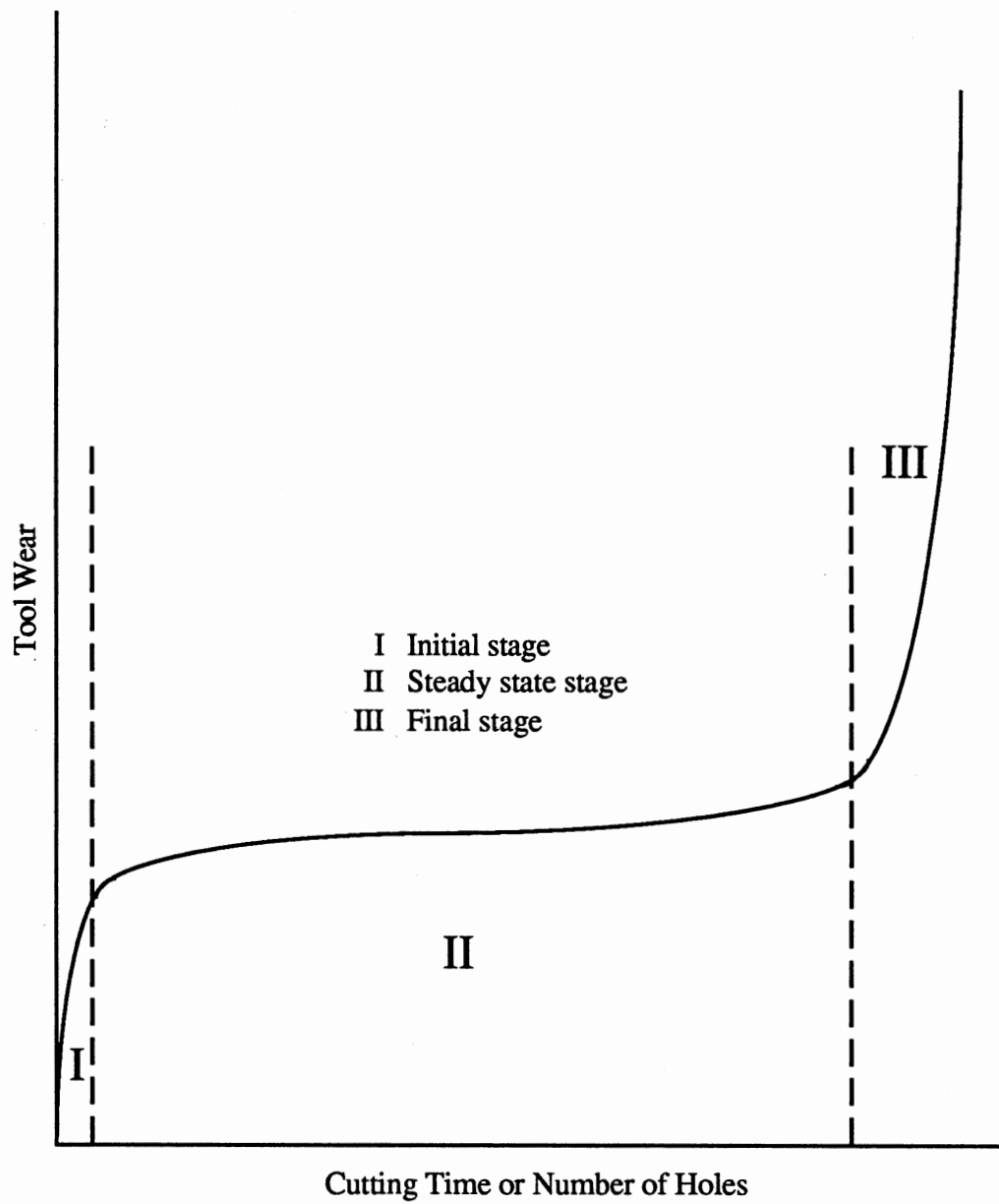


Figure 2.8 Characteristics of the Development of Wear With Cutting Time [1].



$M_w$ , crater wear  $K_M$  and two types of edge wear  $C_T$  and  $C_M$ . The degree of chipping at the cutting edges is also observed in terms of  $P_T$  and  $P_M$  as shown in Figure 2.9. It is reported [18] that of all the types of wear mentioned above, wear at the outer corner is recommended as a performance index for drill life. Kaldor and Lenz [21] and Lenz and Mayer [20] recommended that the following dimensionless parameter be used as a drill life criterion (Figure 2.10):

$$w = B/B_T \quad (2.10)$$

where  $B_T$  is the width of the margin of a new drill and  $B$  is the width of the wear land on the margin

Soderberg et al [17] also come to similar conclusion based on experimental data using an M2 high speed drills on a SIS 1672 steel (~AISI 1045) and a SIS 2541 steel (~AISI 4337) work materials. A majority of failed drills were found to exhibit severe plastic deformation. Examination of the failed drills, which had been stopped at the instance of suddenly appearing, violent noise, clearly showed that the deformation begins at the periphery (flank-margin corner) but rapidly spreads towards the center. They explained this phenomenon by the following mechanism: Increase in wear area leads to an increase in the thrust force in order to maintain constant contact pressure over the increased wear area. This also increases the frictional work and hence generates more heat resulting in temperature rise. The temperature rise is the fastest at the drill corner, where cutting speed is maximum and contact area (wear area) the largest. The temperature rise also accelerates with increasing corner wear. As long as the temperature is below 600°C (boundary of secondary hardening zone of a HSS drill bit material) it is harmless to high speed steel. Above 600°C, mechanical strength of the tool material at drill corner drops rapidly, local plastic deformation takes place, which in turn leads to sudden drastic increase in contact area and feeding force. Therefore, plastic deformation rate again is increased because of

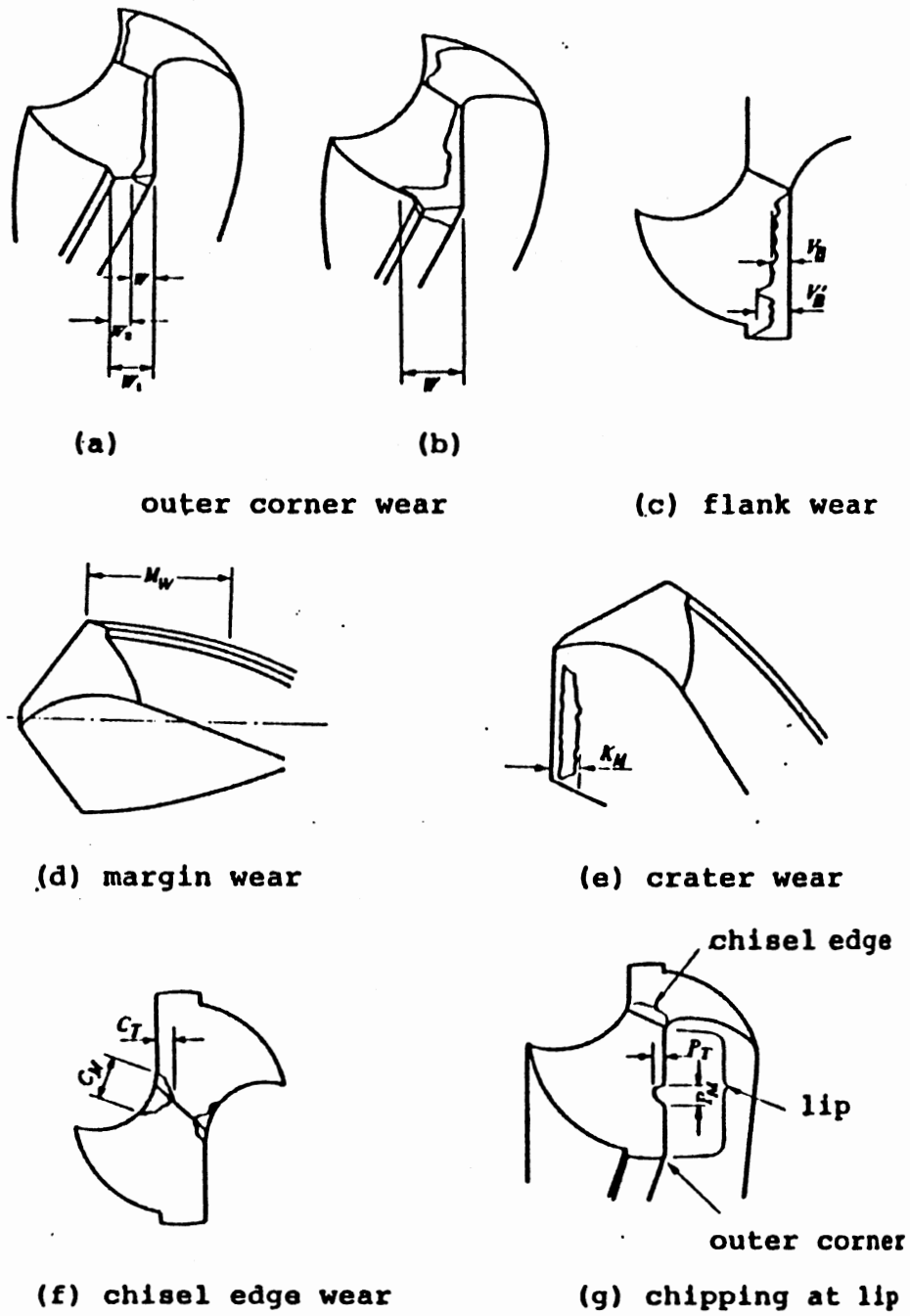


Figure 2.9 Various Types of Drill Wear [18].

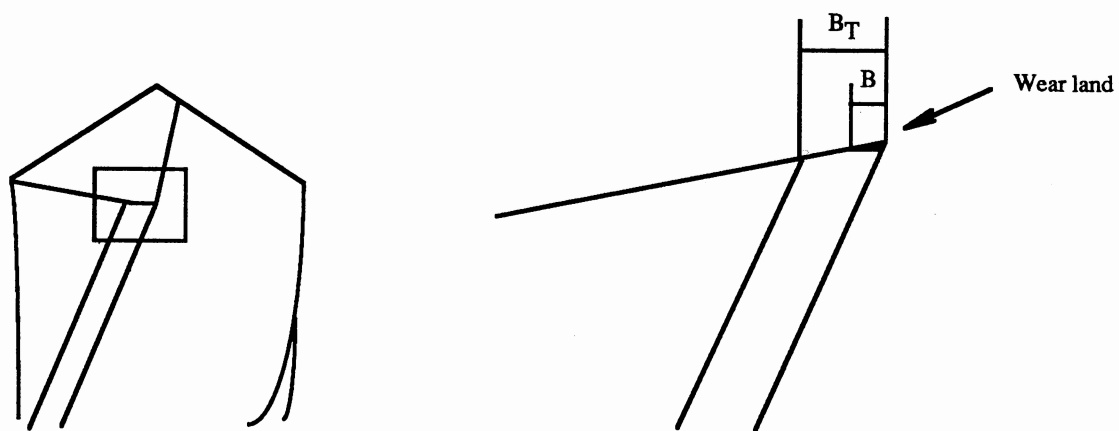


Figure 2.10 Drill Wear at Margin [20, 21]

higher temperature. At this stage wear area grows very rapidly until local seizure occurs at drill corner.

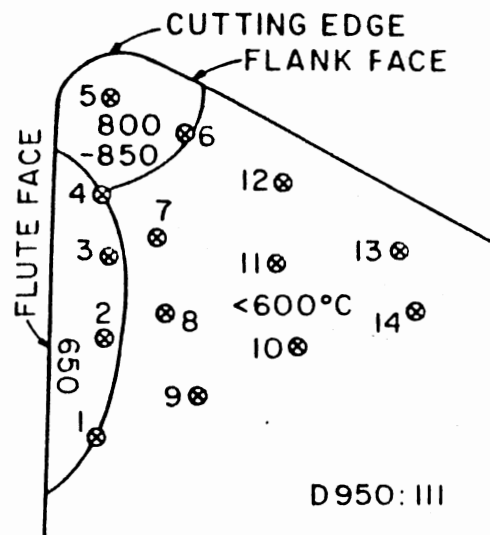
Soderberg et al [17] also found that flank width value for which drill failure is initiated decreases with increasing drilling speed confirming that drill temperature is determined by the combined effects of cutting speed and flank width.

### 2.3.2 Temperature distribution along the cutting edge

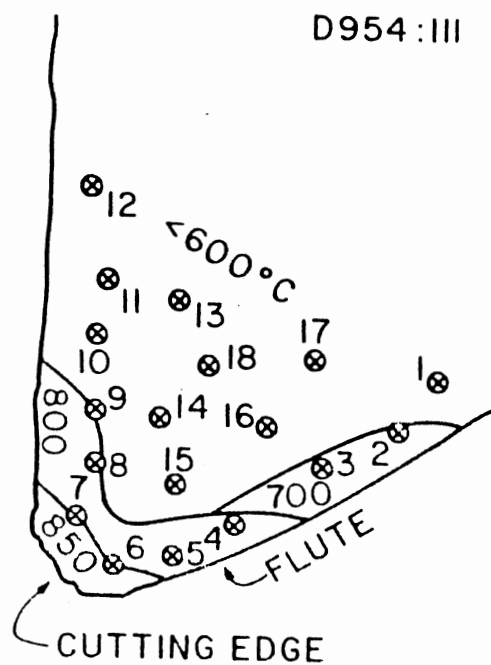
The determination of the temperature distribution in a cutting tool has been an area of interest to investigators of machining because of the strong correlation existing between temperature and the life of a cutting tool. Thangaraj and Wright [19] used an experimental technique based on the fact that certain high speed steels exhibit a loss of temper when heated above their secondary hardening temperature of approximately 600°C.

In order to correlate the microhardness at any point in a section of the drill to the temperature at that point, Thangaraj and Wright found it necessary to prepare a reference heat treatment chart. This was achieved by preparing very thin sections (about 1 mm thick) from a unused drill of the same grade that was being analyzed. One set of these specimens was submerged for sometime in a salt bath maintain at a specified temperature in the range 600-900°C. All specimens were water quenched, mounted in an epoxy resin, ground, and polished. The resulting specimens were subject to microhardness tests to prepare a reference hardness chart.

Using the above chart, Thangaraj and Wright determined the temperature at different points of drill bit. An 8 mm D950 and D954 (drill bit material) drill bits were used to cut 24 mm deep holes in SS1672-01 steel (AISI 1045) at 66 m/min cutting speed and 0.21 mm/rev feed rate. The drills used under these conditions were sectioned along a plane normal to the cutting edge. These sections were ground, polished, and microhardness tests were carried out on them. These were used to obtain the tool temperature distributions using the reference hardness chart. Figure 2.11. shows two examples of the temperature



(a)



(b)

Figure 2.11 Temperature Distribution Obtained From Microhardness Method at the Corner of Drill [19]. Drill material a) D950:III, b) D954:III

distributions obtained using this method. As seen, the temperature at the cutting edge near the margin of a drill is ~800-850°C.

Using the microstructure changes as a result of heating over the secondary hardening temperature developed by Wright and Trent [29], Thangaraj and Wright [19] measured the temperature of an 8 mm M33 drill bit used to cut 24 mm deep holes in AISI 1045 at 40 m/min cutting speed and 0.21 mm/rev feed rate. Figure 2.12 shows the distribution of temperature close to the margin on the flank face. It can be seen that the temperature near the margin is 900°C, which is well above the secondary hardening temperature of the work material (600°C).

### 2.3.3 Drill wear mechanisms

Optical microscopy of the flute surfaces of worn drills [19] showed different interactions between the chip and the drill at distinct regions along the length of the lip. For example in the vicinity of the chisel edge, the contact length is small and consists primarily of a sliding zone. Along the lip, farther away from the chisel edge, three zones (referred to as *a*, *b* and *c*) can be observed. Zone *a* is a region of sliding friction in the immediate vicinity of the lip. Zone *b*, which is towards the rear of zone *a* along the flute surface, is a region of sticking friction. Zone *c*, which is a continuation of zone *b* along the flute surface, is again a region of sliding friction. Near the margin of the drill the sliding zone (*a*) adjacent to the lip fades into a region where the tool material is found to undergo bulk plastic flow. Figure 2.12 shows that temperature in this region which is in the vicinity of 900°C. Such a high temperature is to be expected to be determined considering the fact that heat is generated not only due to plastic deformation in the primary and secondary cutting shear zones, but also due to rubbing contact between the margin and the drilled surface.

In summary, based on the works presented in this section, the flank wear at the margin appears to determine the end of useful life of a drill. Excessive wear at the intersection of the flank face and the margin leads to plastic collapse of this region. This

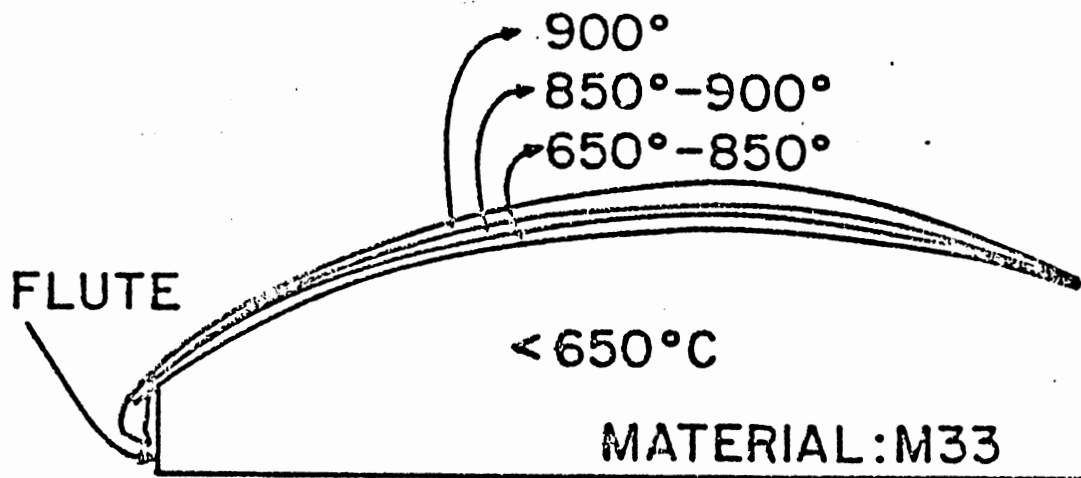


Figure 2.12 Temperature Distribution Obtained From Microstructural Change Method at the Corner of Drill. Drill Material M33 [19].

occurs because of the high temperatures generated ( $>600^{\circ}\text{C}$ ) due to an increase in the area of contact as a result of the wear.

## 2.4 Monitoring of the Drilling Process

As mentioned earlier, once the final stage of the wear begins (stage III of Fig. 2.8), catastrophic failure of the tool becomes imminent. From a production standpoint it is necessary desirable to replace the tool at some point prior to this final stage of wear. As wear progresses to this predetermined level, the tool is said to have reached the end of its useful life. Unfortunately, this is not an easy task. Figure 2.13 [18] shows the distribution of drill life (measured in number of holes drilled before failure) of a batch of 70, 6 mm drill bits, cutting 15 mm deep blind holes at 33.9 m/min cutting speed and 0.22 mm/rev feed rate. Tool material and work material were SKH 9 and S45C (Japanese standards) respectively. Wear at the outer corner is employed as a drill life criterion. Drilling was stopped when 0.3 mm wear was observed at the outer corner of a drill bit. From this figure it can be concluded that the number of holes generally can not be used as a drill life criterion.

One way to determine the drill life is to evaluate drill wear at the corner of a drill bit. This can be done directly, i. e. measuring drill wear periodically after cutting a predetermined number of holes. This method is known as off-line monitoring. In this, the drill is removed periodically from the machine tool for measuring wear or a measuring device should be installed on the machine to accomplish the same.

Liu [30] developed an automated visual inspection for determining the optimum drill life of a multifacet drill (MFD). For inspection, the drill bit is removed from the machine and paced on an instrument which replaces the human inspector and measures automatically the wear area of the drill flank. The drill bit is rejected when the wear area had exceeded some predetermined threshold.



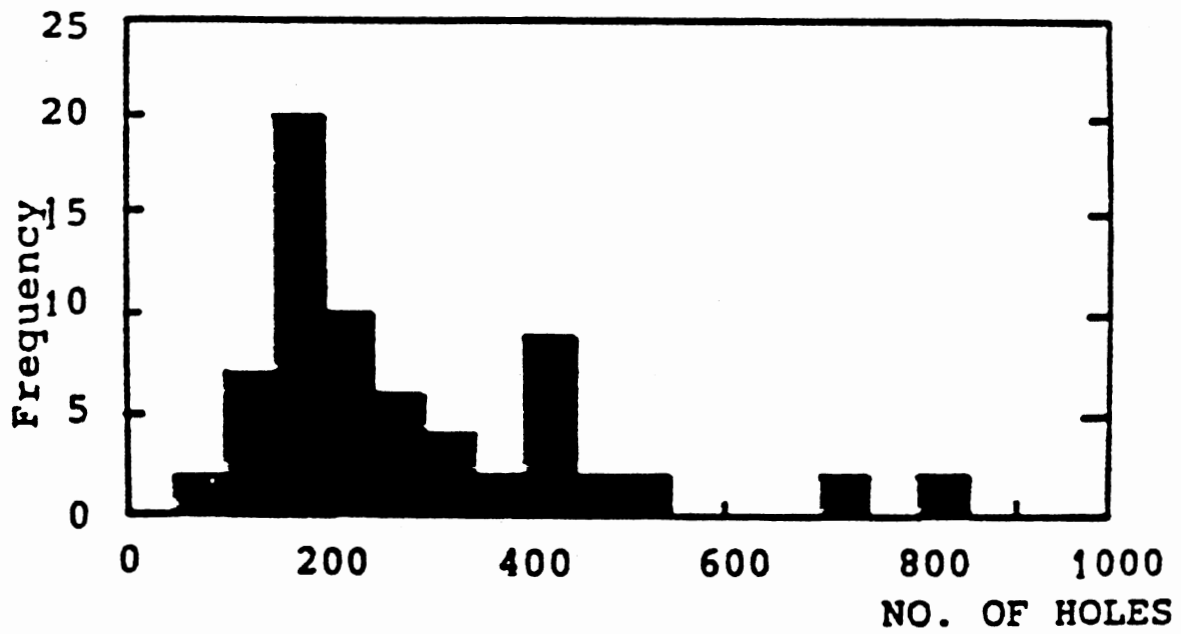


Figure 2.13 Histogram of Drill Life for 70 Drill Bits  
(0.3 mm Corner Wear) [18].

Amini and Winterton [31] determined wear during drilling by monitoring the radioactivity level of the tool that they had previously been exposed to the beam of charged particles in a cyclotron. Good correlation was found between the flank wear land inferred from the readings of radioactivity and microscopic measurements (see Fig. 2.14). Figure 2.15 shows that wear increases rapidly within the first few holes and further increase is gradual with increasing number of holes drilled. Toward the end of the useful life of a drill, wear begins to increase rapidly until the tool fails. Although this method can be used to continuously monitor the wear of a tool, it poses a potential safety problem and may not be practical in a production environment. Moreover it is an inconvenient and difficult technique especially for transfer-line applications. The other technique called, on-line monitoring, is similar to the response of an experienced machinist who decides when to change the tool or the machining conditions based on the signals received by his sensory devices such as his eyes (the color of the chip), ears (the noise) etc. In this method, different sensors, such as cutting force sensors (thrust and torque components for a drilling process), accelerometer for measuring vibration, acoustic emission sensors (AES) for measuring acoustic emission (AE) generated during drilling, strain elements for measuring the strains induced and so on may be used to obtain information regarding the cutting process.

On-line monitoring has received more attention because of the ease with which it can be used on shop floors specially in transfer lines. To study the effect of tool wear on process variables, such as torque, thrust and power, Subramanian and Cook [6] conducted a series of experiments using 13/32 in. high speed steel drills and Meehanite cast iron at a speed of 73.3 ft/min, a feed rate of 0.0065 in./rev. and hole depth of 1 in. It appears that Subramanian and Cook had used two fixtures: One is instrumented with a dynamometer. Holes were drilled in the workpiece in the first fixture till the drill attained certain stage of wear. It is then continued on the workpiece held in the second fixture which contained the dynamometer. This cycle was repeated till the drill failed. The results of their experiments

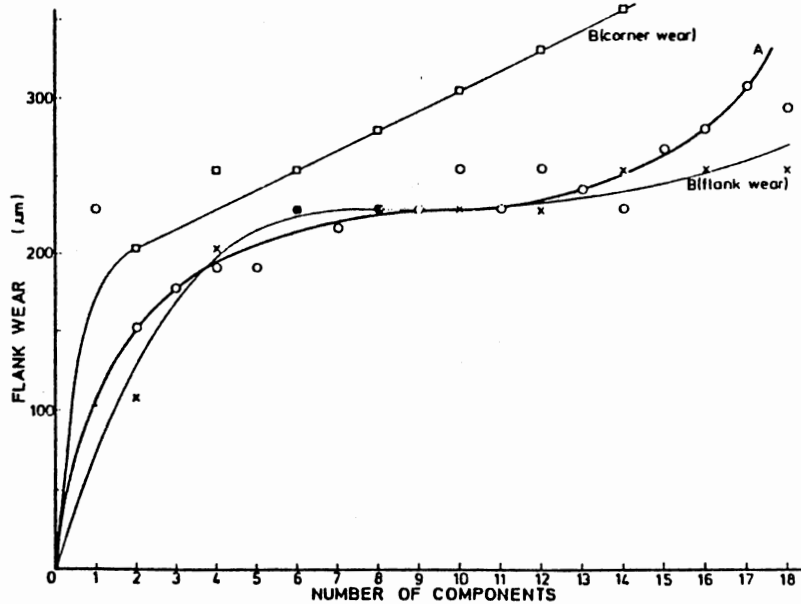


Figure 2.14 Wear Results for Drilling Cast Iron With a 7.94 mm (5/16 inch) Drill. Curve A Gives Radioactivity Measurements, and Curve B the Optical Measurements [31].

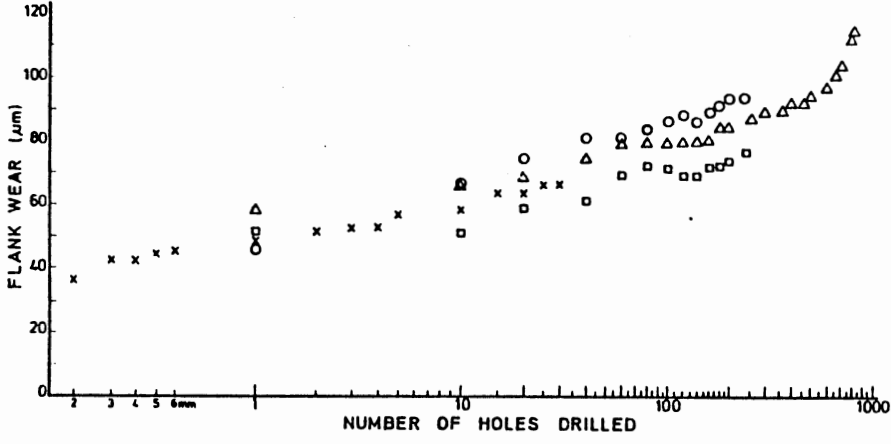


Figure 2.15 Repeatability of Flank Wear With Number of Holes Drilled [31].

are shown in Figures 2.16 through 2.19. From these figures, it can be seen that the flank wear increases rapidly at the end of tool life and that torque, thrust, and power also reflected this situation.

From these results, Subramanian and Cook concluded the existence of two distinct situations: (a) a gradual increase in flank wear accompanied by a similar increase in torque, thrust, and power and (b) a very rapid increase in flank wear near the end of tool life accompanied by large increase in torque, thrust, and power.

Subramanian and Cook also found from their study that the drill life to be influenced significantly by the workpiece hardness. Consequently, the presence of a few random workpieces of high hardness may influence the drill life much more than a large number of workpiece of low hardness. Hence, in an industrial operation, drills may fail very early or after a long time, depending on the occurrence of these few workpieces of high hardness or even hardness variability within a given workpiece. This can explain to some extent the large variation in drill life in an industrial environment.

Subramanian and Cook also found that the workpiece hardness had an influence on the thrust force and torque in a drilling operation. They found that if the variation in workpiece hardness is held within 5% of the mean hardness value then increases in the thrust force can be used as a measure of flank wear.

Braun et al [32] measured torque, thrust, and radial force (perpendicular to the axis of the a drill) as well as sound in order to monitor the drilling process. They concluded that there was no correlation between the wear propagation of the drill and the thrust and torque generated in drilling. But they observed a periodic increase and decrease of the radial force (in the plane perpendicular to drill axis). They attributed this patten to the uneven wear of the lips due to production tolerances resulting from the asymmetric drill wear at one lip until the heights of both lips are equal. The second lip, which is now sharper then begins to cut. This alternating process continues until both lips have no more clearances at the margins. At this time, the drill adheres to the workpiece and breaks necessitating the drilling process

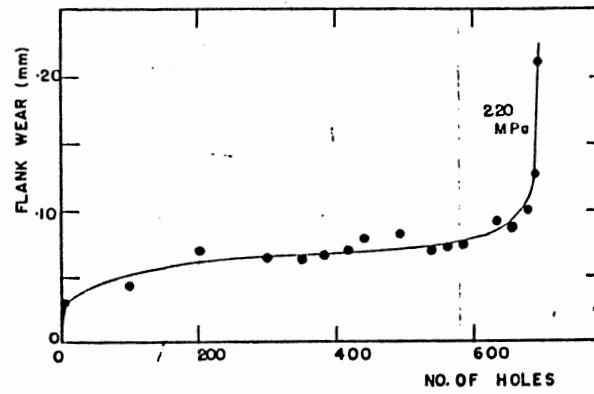


Figure 2.16 Flank Wear Versus the Number of Holes Drilled [6].

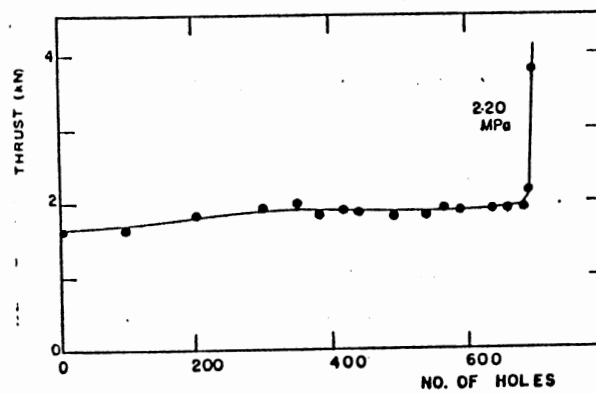


Figure 2.17 Thrust Force Versus of the Number or Holes Drilled [6].

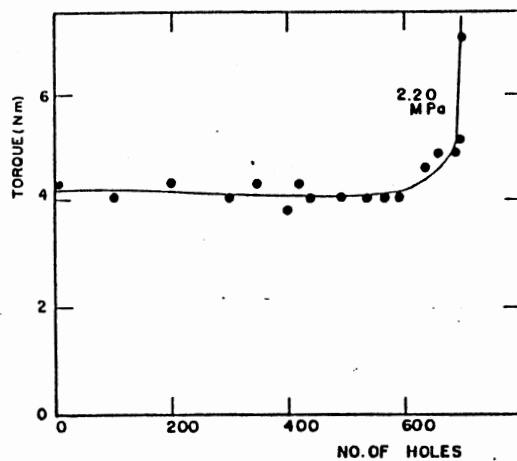


Figure 2.18 Torque Versus the Number of Holes Drilled [6].

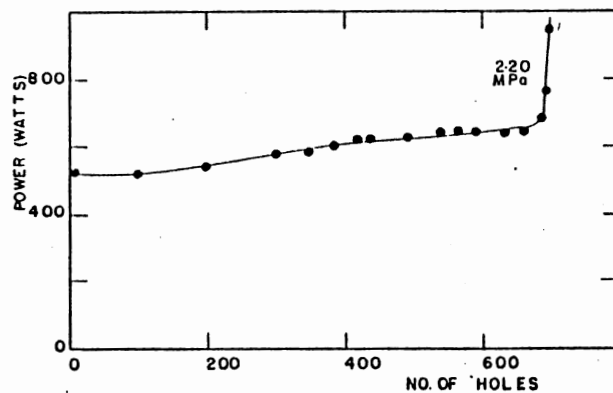


Figure 2.19 Power Versus of the Number or Holes Drilled [6].

to stop in time. Figure 20 shows the uneven wear on the lips as drilling time progresses (after Braun et al).

Typical signatures from a microphone and a force transducer are shown in Figures 2.21 and 2.22 respectively (after Braun et al). They consist of some background signals on which are superimposed sharp oscillatory waves. The authors observed sharp transients to occur mostly, but with increasing frequency as the drilling operation progressed. From a study of these signals they concluded that these are generated by a random nonstationary process.

In the present investigation strains on the table of the machine in the lateral direction (perpendicular to axis of the drill) and along the cutting direction were measured. The results showed that strains signal in the lateral direction is less reliable than the signals from torque, thrust, and strain on the table of the machine in the cutting direction. This may be attributed to the uneven wear of the cutting edge observed in this study similar to that reported by Braun. As can be seen from Figure 2.20, the uneven wear on both sides of the drill may be attributed to a variety of reasons including differences in the hardness of drill and variability of geometry during the manufacture of the drill bit.

Yee and Blomquist [23] investigated vibration analysis technique for predicting drill breakage. They determined the drill wear and predicted drill breakage by applying time domain analysis to the signal from an accelerometer mounted on the workpiece. This method depends on detecting increased vibration patterns due to contact between the drill and the walls of the hole being drilled. They carried out experiments using a 1 mm diameter drills and reported successful prediction of failure. From this study, they concluded that signal to noise ratio gets smaller the further the accelerometer is mounted from the drilling action. This technique necessitates considerable tuning for use with different machine tools and different workpieces and applies basically for small diameter, long, slender drills.

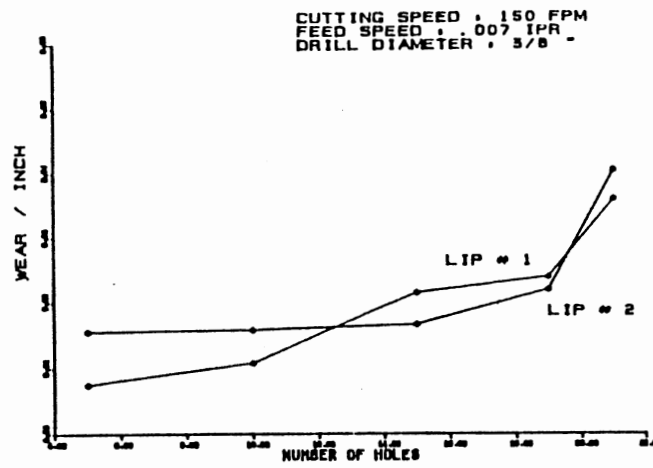


Figure 2.20 Plot of Drill Wear Versus the Number of Holes [32].



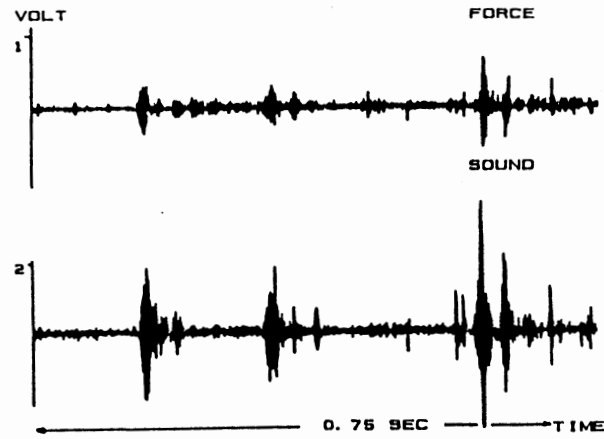


Figure 2.21 Signature Waveform Pattern for a Sharp Drill [32].

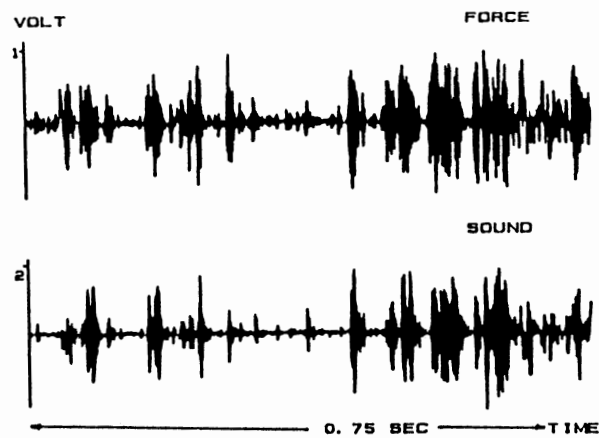


Figure 2.22 Signature Waveform Pattern for a Worn Drill [32].

In the early 80's, the use of acoustic emission (AE) signals was investigated for monitoring of tool wear and tool failure. AE is a high frequency vibration (100 KHz-1 MHz) signal generated by the release of energy in any material under strain due to motion of dislocations. In machining, AE signals are generated in the deformation zones where plastic deformation of the work material takes place to form the chip. In addition, AE signals are generated by chip breakage, tool fracture and chipping. Moriwaki [33] used AE signal from the cutting process for in-process detection of tool failure in turning. He observed a large amplitude in the AE signal when tool failure (including cracking, chipping and fracture) took place during cutting. A major hurdle in the use of these signals is in the development of an appropriate filtering technique and algorithms to separate the signals for tool wear/breakage from the background noise generated in any metalworking process. In the present study, the entanglement of chips inside the drilled holes during the cutting process, had been found to provide additional source for the AE signals which makes this signal nondependable for monitoring the drilling process.

Radhakrishnan and Wu [34] used the dynamic components of the thrust force obtained during drilling of a composite material to monitor the surface quality of the hole being drilled. From their study, they concluded that static aspects such as the mean and the peak forces are unreliable when a close monitoring of the hole quality is required. In comparison, the standard deviation of the thrust showed a better indication of the hole quality. They found very strong correlation between the change in the standard deviation of the lamination frequency component in the thrust and surface signals. Lamination frequency is the number of laminations that drill cuts per unit time.

Thangaraj and Wright [24] and Fabris and Podder [35] proposed experimental thresholds for the gradient of thrust near the end of a drill life. This was based on the rapid change in the rate of change of wear with respect to time in the three regions described above (Figure 2.8). There is a marked difference from region I to region II and from region II to region III. More specifically, regions I and III have much greater rates of

change as compared to region II. This indicates that rate of change of wear is better suited for monitoring the conditions of a cutting tool than the absolute magnitude of the wear. In view of the correlation between the thrust force and the drill wear, the rate of change of thrust force was used in the prediction of drill failure. Thangaraj and Wright [24] reported they were able to find a threshold for the gradient of the thrust to check the end of drill life. As soon as the gradient of thrust exceeded the predetermined threshold, the drill was considered worn and removed from the machine tool.

Nedess and Himburg [36] analyzed the signals of several sensors (thrust, torque, strain, and accelerometer) in drilling. Some of their findings are given in the following.

1. The signal-to-noise ratio for a 8.5 mm drill for different sensors are given as:
  - Thrust and torque: 100
  - Strain: 1.3 - 10 depending on the position
  - Acceleration: 1.1 - 360 depending on the position.
2. Tool wear is more correlated with the dynamic components of the thrust and torque than their mean values.
3. There is no correlation between the flank wear and the dynamic components of the signals.
4. Dynamic components of the thrust, torque and strain at the table unit are correlated to the margin wear of the drill.

Nedess et al that reported corner wear was correlated more with the dynamic components of the sensor signal than the mean. In the present investigation, signal-to-noise ratios in the time domain for various sensors used in drilling were found as follows:

Thrust: 45

Torque: 16

Strain on the machine table along the cutting process: 53

Strain on the machine table perpendicular to drill axis: 45.

## 2.5 Sensor Integration Approaches to Tool Wear Monitoring

An essential step in the design of and control of most mechanical systems requires modeling of the system which involves an analysis of the system dynamic. Some systems can be described directly on the basis of physical laws. There are, however, other systems such as metal cutting, due to the complex nature of the process involved, fully developed theoretical models may not be available. Recognizing this fact, some researchers in the last decade or so have concentrated on the tool wear estimation using pattern recognition or more advanced techniques called neural network which have general structures for most applications.

Kannatey-Asibu [10] explored the possibility of using pattern recognition technique for monitoring the condition of a cutting tool in a machining operation using AE as a specific example. Dornfeld and Pan [11] used linear discrimination function for the classification of the chip forming state, i. e. for the classification of the chip produced in the cutting process to be either continuous or discontinuous chip. Cutting speed, feed rate, depth of cut, and event rate of the RMS of AE signal were selected to characterize the state of the chip. Dornfeld and Pan also reported the use of linear discrimination function to distinguish between continuous and discontinuous chip conditions. They found the event rate of RMS of AE signal the most important parameter in the chip form classification. Depth of cut was reported not to be as crucial as the cutting speed and the feed rate.

Emel and Kannatey-Asibu [12] used linear discrimination functions for the classification of chip noise (including sharp tool), tool breakage, and worn tool using AE sensing. The AE signal was transformed in the frequency domain using the FFT algorithms. Three feature selection methods were used to identify the best features of the signals which correlated well with the tool wear state. In the first method, a cost function was maximized based on minimizing the scatter of patterns between classes and maximizing the patterns within classes. In the second method, features were selected by

maximizing the sum of pairwise class-mean distances. In the last method, features with minimum normalized variance were selected.

Emel and Kannatey-Asibu [12] adapted two approaches for verifying the results. In the first approach the same training set was used for testing the trained pattern recognition classifier. This approach was called resubstitution technique. In the second method, called leave-one-out, one pattern out of  $n$  patterns is separated from the data set, i. e.  $(n-1)$  pattern were used for training. The separated pattern was used for testing. After testing, the separated pattern was returned to the data set and another pattern was separated for testing. The new  $(n-1)$  patterns were used to train the pattern classifier. This procedure was repeated for all patterns. Emel and Kannatey-Asibu reported 97% to 100% for resubstitution method and 69% to 82% for the leave-one-out testing technique. In an extension of the above work Emel and Kannatey-Asibu [13] used a statistical pattern classification and reported success rates between 84% to 94%.

Rangwala and Dornfeld [14, 15] applied a method based on back-propagation (BP) type neural network to predict the tool wear condition in turning on a lathe. The work material was AISI 1060 steel bar 2 in. diameter. Cutting conditions used were the following; feed rate 0.002 -0.008 ipr; depths of cut 0.01-0.03 inch; and cutting speed 278-556 sfpm. The state of tool wear was divided into two classes, namely, sharp and worn tools. For a sharp tool, wear land was considered to be between 0 and 0.25 mm, and for the worn tool 0.5 and 0.75 mm. However, no signal was collected between 0.25-0.5 mm wear land. Cutting force and acoustic emission (AE) signals were sampled simultaneously. Cutting force was sampled at a rate of 1 KHz for a length of 512 data points and AE at the rate of 5 MHz for a length of 1024 data points. Force and AE signals were transformed in the frequency domain using the FFT algorithms. The dimension of the force vector was 256 points (with a resolution of 2 Hz) and that of AE vector was 512 data points (with a resolution of 5 KHz). These two vectors were concatenated and made to a measurement vector of length of 768 data points. It is assumed that some frequencies of the

measurement vector are more related to the tool wear than others. For selecting the most correlated signal, they have attempted to minimize the interclass distances and maximize the distance between classes, in an Euclidean space. A total of 123 samples were collected, each of length 768 data points. Using the above technique, three sets of six features were selected. For the first set, the concatenated vectors of force and AE were used and for the second set, three features from the force vector and three features from the AE vector were selected separately. For the third set, all the six features were selected from the AE vector. To these six features, two more features were added, namely, cutting speed and feed. Therefore the length of the feature vector came to 8.

Altogether 30 samples, equally distributed between sharp and worn tools out of the 123 samples were selected to train a single-layer perceptron. The rest of the samples (93) were used for checking the trained perceptron. A success rate of 88%, 87%, and 80% were reported for features for Set 1, Set 2, and Set 3 respectively. Due to better performance of the features from Set 1 and Set 2, which are a combination of features from AE and force signals, they concluded that feature sets compound of multiple sensor information provide better classification performance.

The same 30 training samples were then used to train an  $8 \times 3 \times 1$  BP type neural network. During training phase, the target of the output node was fixed for fresh tool and 0.99 for the worn tool. During the testing stage, a pattern presented at the input layer was associated with a fresh tool decision if the output node was between 0 and 0.5 or else the pattern was associated with the worn tool. A success rate of 94%, 97%, and 84% were reported for features for Set 1, Set 2, and Set 3 respectively. Again feature sets compound of multiple sensor information provided better classification performance. The performance of BP type neural network was reported to be better than single-layer perceptron. A 100% success rate was reported when the network was trained to predict the actual wear (this case was not mentioned in Rangwala's Ph.D. Dissertation, but included in a paper published in 1987 [15]).

Chryssolouris and Domroese [37] described intelligent machining systems (IMS) which are different from the automated machining workstations is that the IMS are capable of making decisions based on significant information on the state of the system. The reaction of IMS to the system condition, such as tool wear, machine break downs, and other failures must be of the order milliseconds to a second in order to guarantee the safety and reliability of the process.

Chryssolouris et al [37] explained that IMS should take the following steps for making a decision.

- Step 1: Intelligent controller should provide alternatives at any given instant when decision has to be made.
- Step 2: The required criterion such as machining time or machining cost should be established.
- Step 3: The criteria values for each of the proposed alternatives in Step 1 are estimated
- Step 4: By application of one or more decision making rules, the best alternative is selected.

Two separate rule based systems were used to determine the criterion as well as the alternatives. The values of the alternatives for different criteria were obtained from the model of the cutting process associated with each sensor, sensor information, and part information from general manufacturing data-base.

Chryssolouris et al [37] considered three different models based on the use of three sensors, namely, force, temperature, and acoustic emission (AE). Each of these models provide values for alternatives using additional information, such as part information and manufacturing data-base. A rule based system or some other technique is assumed to integrate the tool wear estimate of these three models and to provide more reliable tool wear estimation. A decision making rule determines the cutting conditions.

Chryssolouris et al [38] also compared three techniques, namely, neural network, multi-regression, and group method of data handling (GMDH) for integrating tool wear estimates by the three models mentioned above, using computer simulation. They concluded, that neural network was more effective in learning a relationship between sensor signals and tool wear estimate than the other two methods, especially when the relationship is nonlinear. Moreover, neural network showed that it is usually less sensitive to deterministic errors than other sensor integration techniques.

In an another attempt, Chryssolouris et al [39] used experimental data for the estimation of the state variables in the machining process, such as power, surface roughness etc. for different feed rates, cutting speeds, rake angles, widths of cut, and flank wear of the tool. Three techniques mentioned above, namely, neural network, multi-regression, and GMDH were used to estimate the state variables. Again, they concluded that neural network is superior to other methods. It is, however, not clear as to why Chryssolouris et al [38] used three models for tool wear estimation and then integrated the estimations using the neural network as the neural network would cover the function of the three models using direct sensor signals.

Chryssolouris et al [40] used experimental data from three sensors, mentioned above, and fed them into three models for the estimation of tool wear. They used neural network and statistical method for the synthesis of the three estimates of tool wear from the three models. They reported that sensor integration based on statistical information did not provide better estimation than information from a single sensor. Similarly, the neural network provided better estimation of tool wear than using information from only one sensor. They ran computer simulation for test data composed of linear, sinusoidal, and random signals. They reported that integration of sensors provided better estimate of tool wear than when only one sensor was used. When the sensors operated properly and the models reflected the complexity the process, sensor integration using statistical methods was reported to provide better tool wear estimation than neural network. But, if the



process model does not adequately reflect the complexity of process then neural network provided better estimate of wear. In case of failure of one of the sensors, statistical method was found less sensitive than neural network.

Tansel and McLaughlin [41] used ART2 neural network for the detection of tool breakage in the milling process. The resultant cutting force was fed into the network. The neural network first classified 780 simulation data in a series of cutting conditions, and gained experience. It continued to work on the experimental data by using previous experience and continued classifying the 36 experimental data. Tansel and McLaughlin reported that when vigilance of 0.98 was used, the network classified the unbroken tool input data into seven different categories and classified the broken tool input to four different categories. The success rate of the network on the experimental data was reported to be 97.2%

Elanayar et al [42] have used neural networks to model the tool wear in machining using the sensor data from the three components of the cutting force. When both crater wear and flank wear were present, they reported that they could train their neural system to predict both, as well as surface roughness to an acceptable degree of accuracy. Kamarthi et al [43] used a method based on Kohonen's self organizing feature map for the classification of data from force and vibration sensors and the subsequent estimation of the degree of tool wear. It was reported that they could achieve 95% success rate of the detection of tool wear level.

Neural networks are composed of many nonlinear computational elements operating in parallel. The computational elements or nodes are connected by adjusting weights. The knowledge is stored in neural network by adjusting the weights. Neural networks have shown potential in areas of pattern recognition and function approximation. These interesting features have attracted researchers in metal cutting for monitoring of tool wear. As presented in this section, a considerable work was conducted by many researchers in this area. Different type of neural networks, such as BP, ART2, Kohonen's self

organizing map etc. have been used for monitoring tool wear. Chapter III presents neural network models using the following techniques, namely, clustering, mapping, and decision surfaces technique as well as their performance in tool wear monitoring.

Artificial neural network structures are based on the present understanding of the biological nervous system [44]. Although an artificial neural network model with a crude brain-like structure, has great potential in the areas of pattern recognition and modelling of the highly nonlinear systems using general architecture, they are, however, far from reaching the performance of a brain [44] at this stage. In Chapter VI we will show that when multiple sensor signals are used to monitor different states of tool wear and sensor fusion approach is used, the three techniques, namely, clustering, mapping, and decision surfaces may not be able to define the state of tool wear adequately. This is due to the fact that (as shown in Chapter VI) characteristics of sensor signals from different states of tool wear are mixed and the above techniques may not be able to classify sensor signals to the right state of tool wear. Although high success rates were reported by some researchers for sensor fusion techniques there are some real concerns, as will be discussed in Chapter VI, regarding the validity of approach.

## 2.6 Problem Definition

A feature common to most of the research reviewed here is the selected cutting speeds are considerably higher than the recommended cutting speeds used in industry (at least more than 1.5 times the cutting speed recommended by the Machining Data Hand Book [45]). As observed in the present investigation, if recommend cutting speeds are used drill life would be in the tens of thousands of holes which would be impractical in a laboratory environment. Therefore, most researchers have selected higher cutting speeds than recommended to limit the drill life merely a to few tens or rarely hundreds of holes that is feasible in a laboratory environment. In the present investigation a different strategy was used. This strategy involves the use of recommended cutting speed during the

collection of data and increased cutting speed (twice the recommended cutting speed) to accelerate wear to simulate different stages of drill life. This strategy is explained in detail in Chapter V.

As mentioned earlier, the flank wear at the margin determines the end of a useful life of a drill in most cases. Excessive wear at the intersection of the flank face and the margin leads to plastic collapse of this region. This occurs because of the high temperatures generated ( $>600^{\circ}\text{C}$ ) due to increase in the area of contact as a result of wear. In the present investigation, flank wear at the margin is considered as a criterion for drill life.

Sensor signals in the frequency domain have not been studied in depth in the past. Only one set of data (or three sets of data [24]) was used to calculate the power spectral density (PSD). As shown in Chapters IV and V, the variance of the estimate of power of periodogram at each frequency is greater than the power at that frequency. Therefore PSD of the sensor signals used in the previous research may not be reliable. In the present investigation, the variance is reduced by averaging the estimate of power which was obtained from every hole, at each frequency over a number of holes during which the drill wear development is negligible for each sensor signal.

In this research, characteristics in the time and frequency domains for four sensor signals, namely, thrust, torque, and strains on the machine tool table in the cutting direction and perpendicular to the drill axis are studied and correlated with the corner wear of the drill.

The possibility for the application of neural network for sensor integration is investigated. Three techniques, namely, clustering, mapping, and decision surfaces have been studied for classifying sensor signals to different states of drill wear.

**CHAPTER III**  
**REVIEW OF PARAMETER ESTIMATION AND PATTERN**  
**RECOGNITION AND THEIR APPLICATION**  
**TO METAL CUTTING**

Automation of the machining process requires the ability to monitor the tool condition reliably during the cutting operation. Tool wear monitoring relies on sensors which provide information to the decision making system. The decision making system is expected to interpret the information and provide corrective actions in the absence of a human operator. Safe, economical, and scrap free operation can be achieved by a good sensory and decision making system.

Tool wear has a strong influence on the surface roughness and dimensional accuracy of the finished product. A reliable tool wear monitoring system can eliminate the down time of the machine tool associated with tool breakage and reduces the overall cost of operation by optimizing the process. Tool wear is rather a complex process and is affected by a number of factors, such as temperature, cutting speed, feed, and cutting fluids used. Because of this complexity, theoretical correlation between tool wear and operating conditions is not readily available. One of the first attempts in this direction is the Taylor tool life formula, developed by F. W. Taylor. It is an empirical relation between cutting speed and tool life and given by

$$VT^n = C \quad (3.1)$$

where  $V$  is cutting speed,  $T$  is tool life in minutes,  $C$  and  $n$  are constants depending on the tool-work material combinations used. The difficulty associated with this equation is it requires considerable experimental data at different cutting conditions to determine  $C$  and  $n$  for a combination of tool and work materials. Due to the stochastic nature of the wear process, scatter in data can be expected which makes it difficult to apply the above equation to an on-line tool wear monitoring system.

As mentioned earlier, sensors are important elements of any tool monitoring system. Excellent reviews of tool wear sensors can be found in Micheletti [8] and Tlustý et. al. [9]. Sensors can be classified as off-line and on-line sensors for monitoring the cutting process. Off-line sensors usually use optical, radioactive, or pneumatic techniques. These techniques are simple and easy to interpret but some of them may pose danger (radio active) or can be implemented only between cuts (such as optical optical techniques).

On-line sensory devices, such as force sensors, accelerometers, and acoustic emission (AE) sensors can be used easily for they do not interfere with the cutting operation. But, it is somewhat difficult to obtain a good correlation between tool wear and the sensor signals. The following three approaches were considered to obtain the correlation between the tool wear and sensor signals.

1. Theoretical modeling: Some correlation between sensor signals, for example, force and tool wear is obtained by using the mechanics of the cutting process.
2. Empirical modeling: The parameters of an empirical model are tuned using the experimental data.
3. General modeling structure: The parameters of general modeling structures, such as pattern recognition techniques or mapping techniques, for example, back propagation (BP) network are tuned using the experimental data.

Developing a reliable theoretical model (first method) that correlates tool wear and sensor signal is extremely difficult due to the complexity of the process. In the second method, an empirical model is proposed and its parameters are tuned using the experimental

data. An example of this technique is parameter estimation which will be discussed in Section 3.1. The third technique, the subject of Section 3.2, is pattern recognition and mapping techniques using neural network. No model is required to relate sensor data and tool wear. In this method, the problems may be approached in two ways. In the first approach, the problem of deciding whether or not the tool is worn is considered as one of associating pattern of sensor signals with appropriate tool condition (sharp or worn). In the second approach, sensor signals are mapped to the state of tool wear using mapping techniques. In both approaches, learning algorithms are used to adjust the parameters of a pattern classifier or mapping techniques with a general predefined structure.

### 3.1 Parameter Estimation

As mentioned earlier, the mechanism of tool wear is rather complex and might be highly nonlinear. A solution proposed by Liang et al [46] and Takata et. al [47] is based on the following assumptions. The cutting process, thought highly nonlinear, can be represented by a linear model at any given instant. The parameters of the linear model are functions of cutting conditions, such as cutting speed, feed rate, and depth of cut as well as the tool-work material combination,. During the cutting process, only tool wear is changing and all other factors remain unchanged. Therefore, the change of parameters of the linearized model must be a function of tool wear. This method, thus suggests that tool wear can be evaluated by monitoring the change of parameters of the cutting process.

The first formulation and its solution, as well as the application of parameter estimation was given by Gauss [48] in his famous determination of the orbit of the asteroid, Ceres. Gauss formulated the parameter estimation as an optimization problem and introduced the least square method based on minimization of the sum of the squares of the error. Since then, the least squares criterion has been used extensively. The least square method is rather simple and easy to understand. However, under some circumstances, it can estimate wrong mean values (bias estimate). However, this can be overcome by using

various extensions to this method. The least square method is restricted to model structures that are linear with unknown parameters.

In parameter estimation, the inputs and the outputs of the system are used to evaluate the parameters. As there is no access to real inputs (for example actual cutting speed, feed rate etc., see Chapter V for details) many researchers [46, 47] have used autoregressive (AR) models which do not require such inputs.

It will be shown in this investigation, (see Chapter V for details) that in the drilling process, the gain of the system may change while all other parameters of the system remain practically constant during the tool wear development.

### 3.2 Pattern Recognition

The motivation behind the application of pattern recognition to metal cutting arises from the fact that a human operator can sense whether a tool is sharp or worn by observing the machining operation. The sensory information used to make this decision is usually of various types: visual (observation of chip color, presence of smoke, detecting surface finish of the workpiece), audio (sound generated by rubbing action of the workpiece on the tool or vibrations occurring during the cutting process) and olfactory (smell of smoke generated due to tool wear). These sensory signals are processed by the brain and act as memory triggers which facilitates the operator to decide on the status of tool wear in a qualitative manner. Correlation of the sensory signals with tool wear depends to a large extent on the knowledge and experience of the operator. But, human pattern recognition is highly developed but poorly understood. The task of simulating it on a computer is at best formidable. Human brain is able to integrate information from its different sensor signals to obtain a better picture of the process. If the information from a sensor signal, say vision, is inadequate to make a reliable decision, audio information may be used as a supplement to integrate with the visual sensor. Or, if one of the sensors fails to provide sufficient information, the other sensor information may be used in order to make a reliable

decision. For example, it is believed that touch sense of blind people becomes stronger to overcome blindness. In short, the brain seems to be extremely capable of capturing and integrating sensor signals and at the same time ignoring noise from one or more of these sensors.

Artificial neural networks attempt to mimic the computational architecture of the human brain. The objective is to incorporate intelligent functions such as learning and pattern recognition in computers. The architecture of the human brain is highly complex and not well understood at present. Therefore, the current neural network architecture can only resemble the brain in a very coarse way. Artificial neural network, similar to a human brain, consists of many processing elements massively interconnected by links with variable weighing factors. Processing elements (or nodes) used in neural network models are nonlinear. The massive parallel connection provide neural network with high computation rates. Neural network models are specified by the network topology, node characteristics, and training rules. Training rules specify an initial set of weights and indicate how weights should be adapted during use to improve performance.

As mentioned earlier, human brain is capable of integrating sensor signals. This was the motivation behind many researcher's decision to use artificial neural network for integrating different sensor signals in machining to get a better estimation of tool wear. We will show in Chapter VI that there are concerns regarding the extent of applicability of artificial neural network for sensor integration in the presence of noise. As some neural network paradigms use clustering technique, this method is described below.

### 3.2.1 Clustering technique (nearest neighbor classifier)

Nearest neighbor is one of the most intuitive approach to the problem of pattern recognition. The motivation for using distance function as a tool wear classification is as follows. The most obvious way of establishing a measure of similarity between pattern vectors, which also consider as points in Euclidean space, is by determining their



proximity. For example, in Figure 3.1, we may intuitively arrive at the conclusion that the pattern  $x$  belongs to class  $C_i$  solely on the basis that it is closer to the patterns of this class. To show this technique mathematically, consider  $M$  cluster centers  $m_1, m_2, \dots, m_M$  ( see Figure 3.1). The Euclidean distance between an arbitrary pattern vector  $x$  and the cluster centers is given by

$$D_i = |x - m_i| = \sqrt{(x - m_i)^T(x - m_i)} \quad (3.2)$$

A nearest neighbor classifier computes the distance from a pattern  $x$  of an unknown classification to all classes and assign the unknown vector to the class to which it is the closest. In other words,  $x$  is assigned to class  $C_i$  if  $D_i < D_j$  for  $i \neq j$ . However, since the proximity of two patterns is a relative measure of similarity, it is usually necessary to establish a threshold in order to define the degrees of acceptance of similarity in the cluster-seeking process. Figure 3.2 shows three different cluster arrangements which have been obtained for the same data by varying the threshold,  $T$ .

There is one problem associated with this technique, namely, all clusters must be linearly separable. In the other words, there is a hyperplane in  $n$ -dimensional space ( $n$  is the dimension of feature space) that separates every pair of clusters, i. e. there is no member of one class on the other side of the hyperplane. This problem can be solved by reducing the threshold and dividing a whole class into subclasses using some neural network paradigms which will be discussed in Section 3.3.

### 3.2.2 ART 2 neural network

The analog adaptive resonance theory (ART2), introduced by Carpenter and Grossberg [50] in 1987, is an extension of the binary adaptive resonance theory (ART1). It has emerged through the development of adaptive theory presented by Grossberg [51].

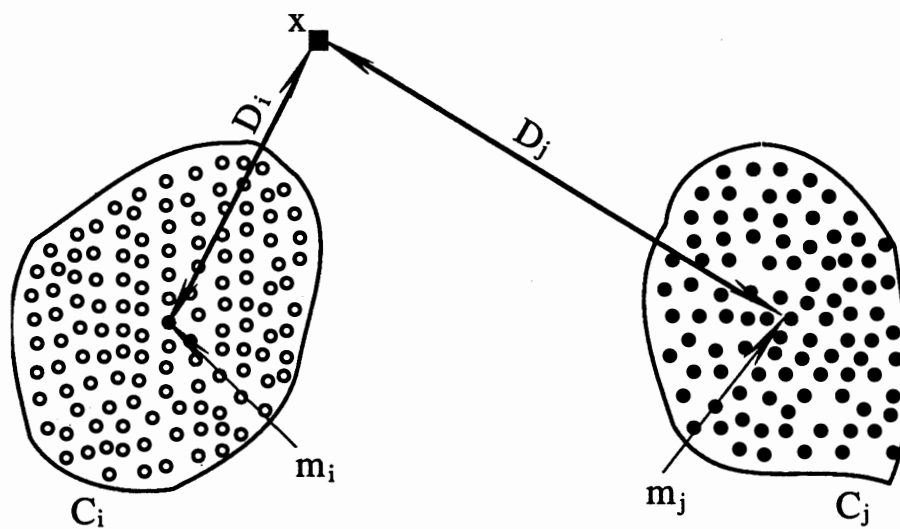


Figure 3.1 Classification of Patterns by Nearest Neighbor Concept (Clustering Technique) [49].

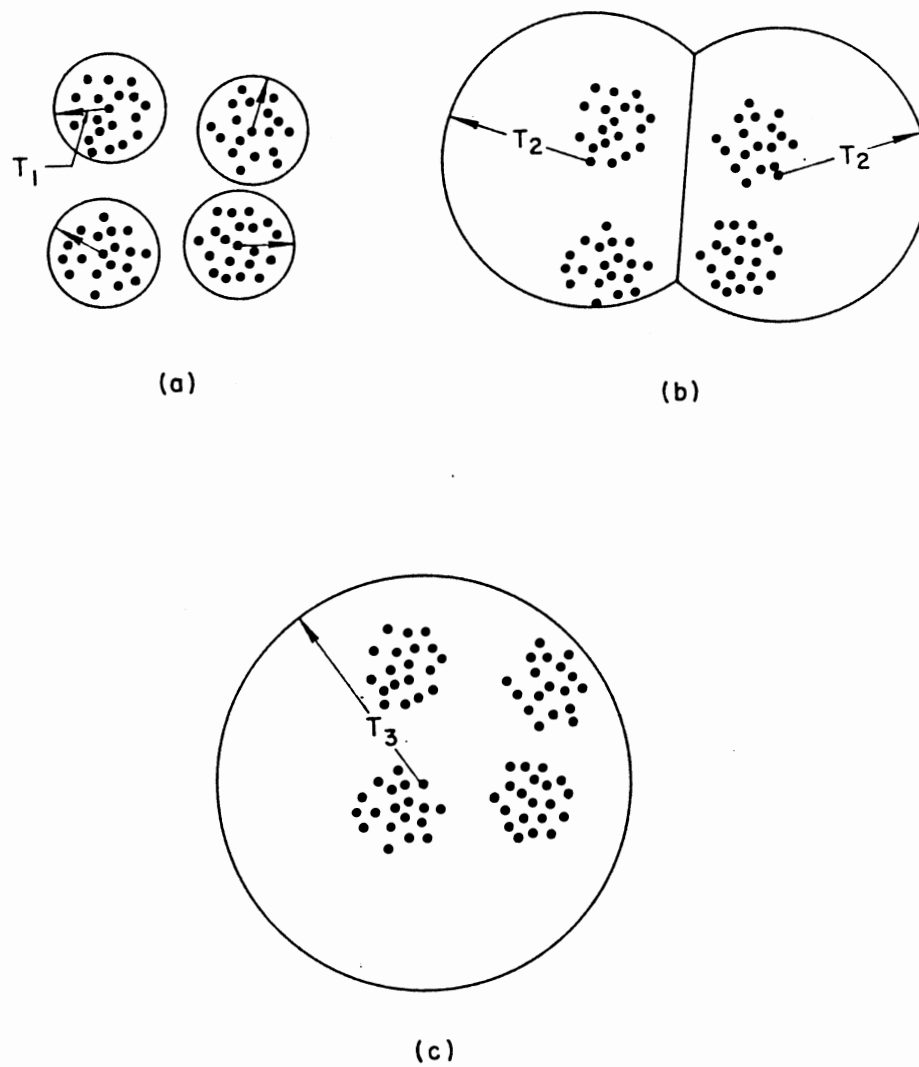


Figure 3.2 Effect of the Threshold on Cluster Arrangements [49].

ART2 is two layer nearest neighbor classifier (clustering method) that stores an analog arbitrary pattern.

$$A_k = (a_1^k, a_2^k, \dots, a_n^k) \quad k = 1, 2, \dots, m \quad (3.3)$$

ART2 learns on-line and operates in both discrete and continuous times.

Figure 3.3 shows the major components of an ART2 network with multi-inputs and multi-outputs. Matching scores are computed using feed forward and the maximum value is enhanced using lateral inhibition among the output nodes.

ART2 network forms clusters and is trained without supervision. This network implements a clustering algorithm that is very similar to the sequential leader clustering algorithm described by Hartigan [52]. The leader algorithm selects the first input as the exemplar for the first cluster. The next input is compared to the first cluster exemplar. It follows the leader and is clustered with the first if the distance to the first is less than a threshold (which is defined by the value of vigilance parameter for ART2 network). Otherwise, it is the exemplar for a new cluster. This process is repeated for all the following inputs. The number of clusters thus grows with time and depends on both threshold and the distance used to compare inputs to cluster exemplars.

A matching threshold, called vigilance which is between 0 and 1, must be set to control the size of clusters. This threshold determines how close a new input pattern must be to a stored exemplar to be considered similar. A value near one requires a close match and smaller values accept a poorer match. New inputs are presented sequentially at the bottom of the net. After presentation, the input is compared to all stored exemplars in parallel to produce matching scores. The exemplar with the highest matching score is selected using lateral inhibition. It is compared to the input by a or mathematical relationship. If the result is greater than vigilance threshold, then the input is considered to be similar to the best matching exemplar and the input merges to that category. If the result

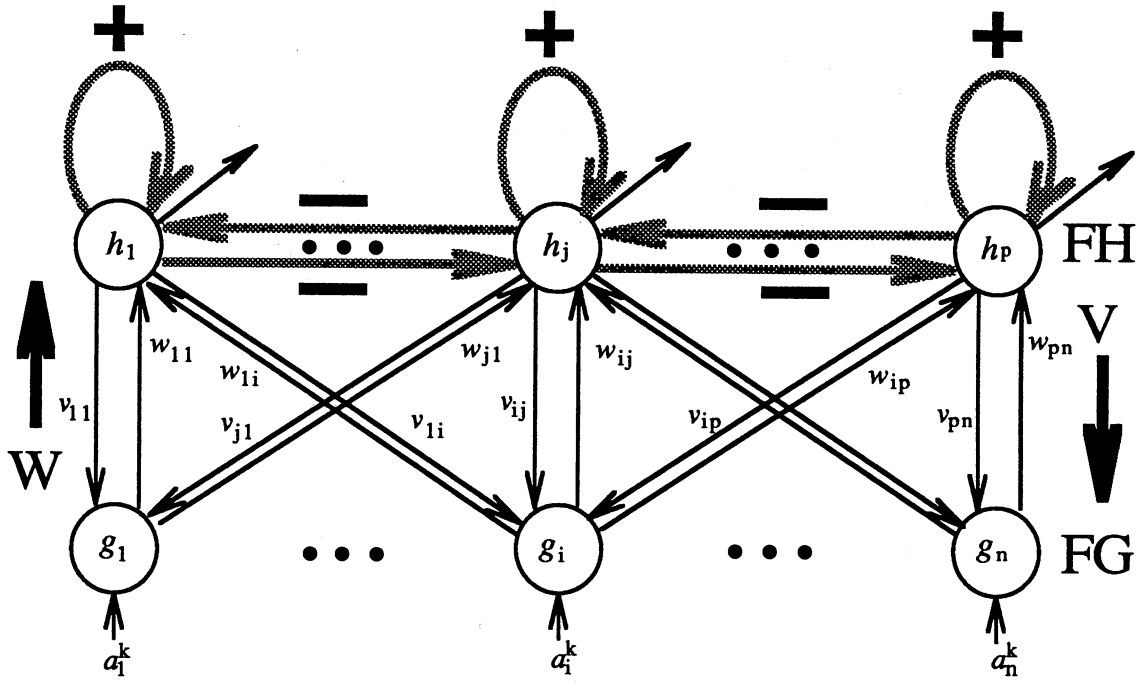


Figure 3.3 Major Components of ART2 Neural Network [53].

is less than the vigilance parameter, the input is considered to be different from all the exemplar and it is added as a new exemplar. Each additional exemplar requires one node and  $2N$  new connections to compute matching scores ( $N$  is the number of inputs).

Figure 3.4 shows the behavior of ART2 network for four patterns, namely A, B, C, and D for different values of the vigilance parameter  $\rho$ . For  $\rho = 0.95$ , the network classify all patterns correctly into different classes, while for  $\rho = 0$  the network can not classify correctly .

### 3.2.3 Kohonen's self organizing maps

Kohonen creates a vector quantizer by adjusting weights from common input nodes to  $M$  output nodes arranged in two dimensional grids as shown in Figure 3.5. Output nodes are extensively interconnected with many local connections. Continuous valued input vectors are presented sequentially in time without specifying the desired output. After enough input vectors have been presented, weights will specify clusters or vectors centers that sample the input space such that the point density function of vector centers tends to approximate the probability density function of the input vectors . In addition, the weights will be organized such that topologically close nodes are sensitive to inputs that are physically similar. Output nodes will thus be ordered in a natural manner.

Figure 3.6 shows the algorithm that forms feature maps requiring neighborhood to be defined around each node. Thus, neighborhood slowly decreases in size with time (Figure 3.6). Weights between input and output nodes are initially set to small random values. An input is presented, then the distances between the input and all nodes are computed. If the weight vectors are normalized to have constant length (the sum of the square weights from all inputs to each output are identical) then the node with the minimum Euclidean distance can be found by using the network (Figure 3.5) to form a dot product of the input and weights. The selection requires procedure for minimum Euclidean distance which is equivalent to a problem of finding the node with a maximum dot product of the

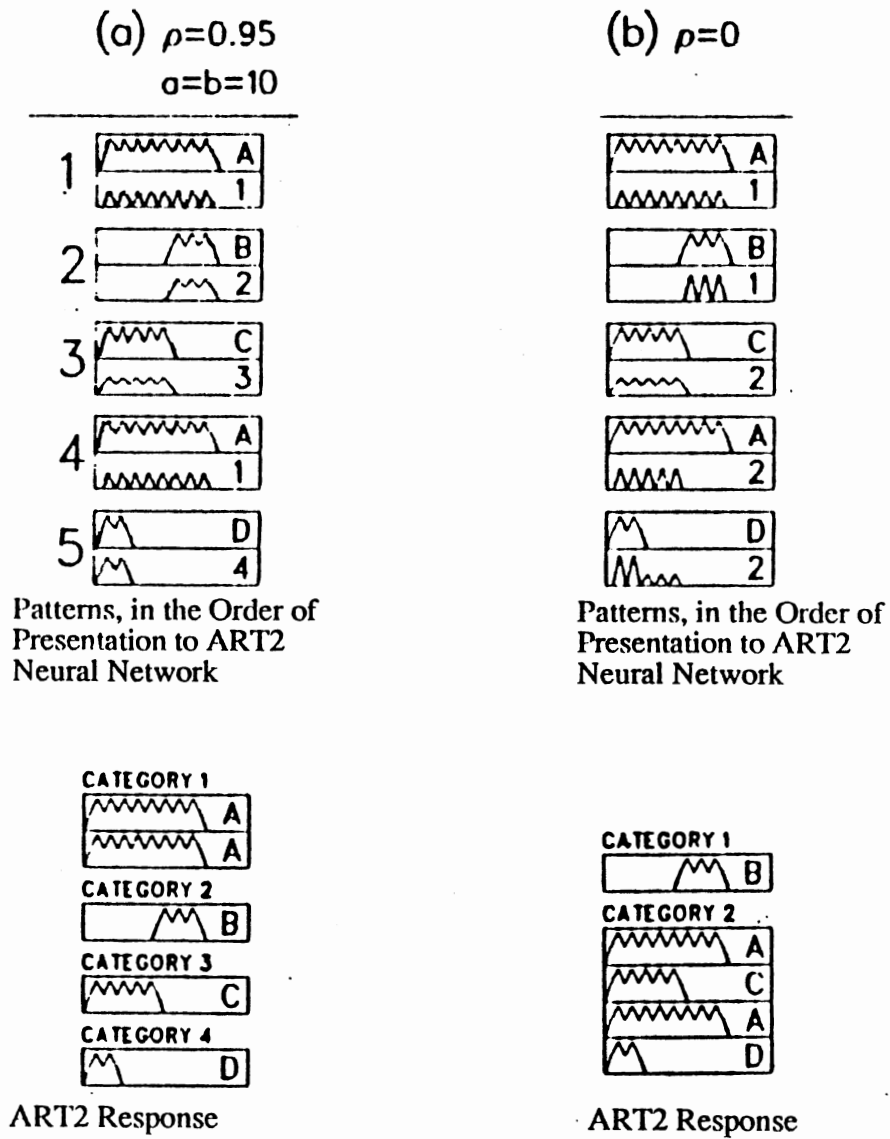


Figure 3.4 Function of ART2 neural Network for two Different Value of Vigilance Parameter a)  $\rho = 0.95$ , b)  $\rho = 0$  [50].  
 1,2, ...,5 are the order of presenting patterns to the network.  
 Two graph are depicted for each trail, the top graph shows the input pattern and the bottom graph shows the associated long term memory.

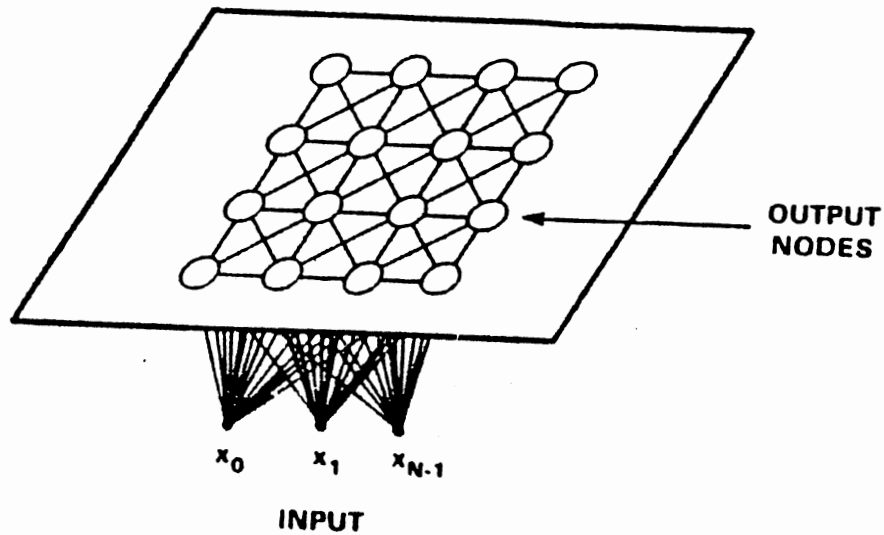


Figure 3.5 Two dimensional array of Output Nodes Used to Form Feature Maps [44]. Every input is connected to every output node via a variable connection weight.

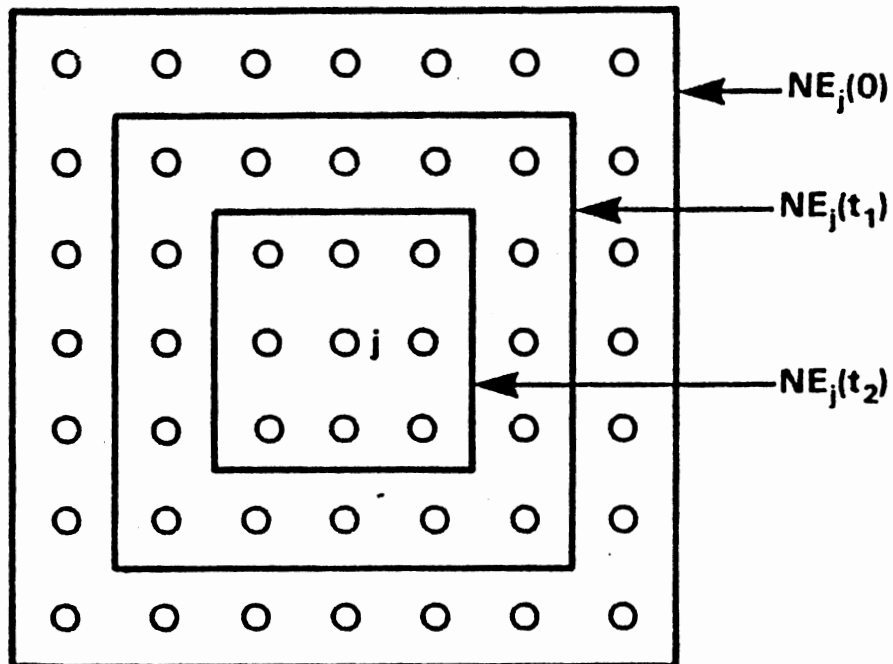


Figure 3.6 Topological Neighborhoods at Different Times as Feature Maps are Formed [44].  $NE_j(t)$  is the set of nodes considered to be in the neighborhood of node  $j$  at time  $t$ . The neighborhood starts large and slowly decreases in size over time. In this example  $0 < t_1 < t_2$ .



input and weight vector of the node. This node can be selected using extensive lateral inhibition. Once this node is selected, weights for it and to other nodes in its neighborhood are modified to make these nodes more responsive to current input. This process is repeated for further inputs. Weights eventually converge and are fixed.

Figure 3.7 presents an example of the behavior of this algorithm. The weights of 576 output nodes are plotted in these four subplots when there are two random independent inputs uniformly distributed over the region enclosed by the boxed areas. Line intersections in these plots specify weights for one output node. Weights from input  $x_0$  are specified by the position along the horizontal axis and weights from  $x_1$  are specified by the position along the vertical axis. Lines connect weight values for nodes that are topological nearest neighbors. Weights start at zero and clustered at the center of the plot. Weights then gradually expand in an orderly way until their point density approximates the uniform distribution of the input samples.

#### 3.2.4 Back propagation (BP) neural network

##### (Multi-layer perceptron)

BP neural networks are feed-forward networks with one or more layers of nodes between the input and the output layers. These additional layers contain hidden units or nodes that are not directly connected to both the input nodes and output nodes. Figure 3.8 shows a multi-layer BP network with two layers of hidden units. BP network overcomes many of the limitations of a single layer perceptron, but had not been used generally in the past because the effective training algorithms were not available. A training algorithm was developed by Rumelhart et al [54] in 1986. Although it can not be proven that these algorithms converge as with single layer perceptrons, they have been shown to be successful for many problems of interest [54].

The capability of multi-layer perceptrons stems from the nonlinearities used within the nodes. If nodes are linear elements, then a single-layer network with appropriately

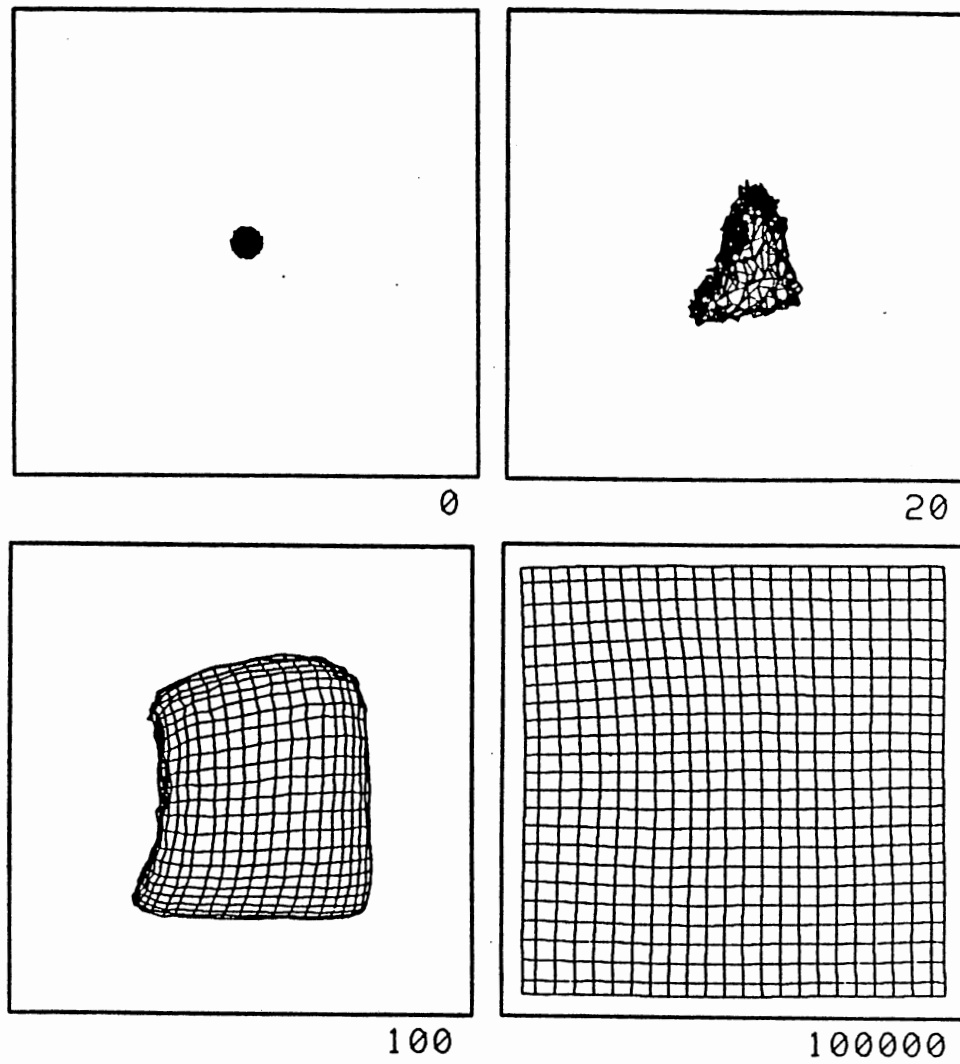


Figure 3.7 Four Frames for a Kohonen Self-Organizing map Neural Network [55].

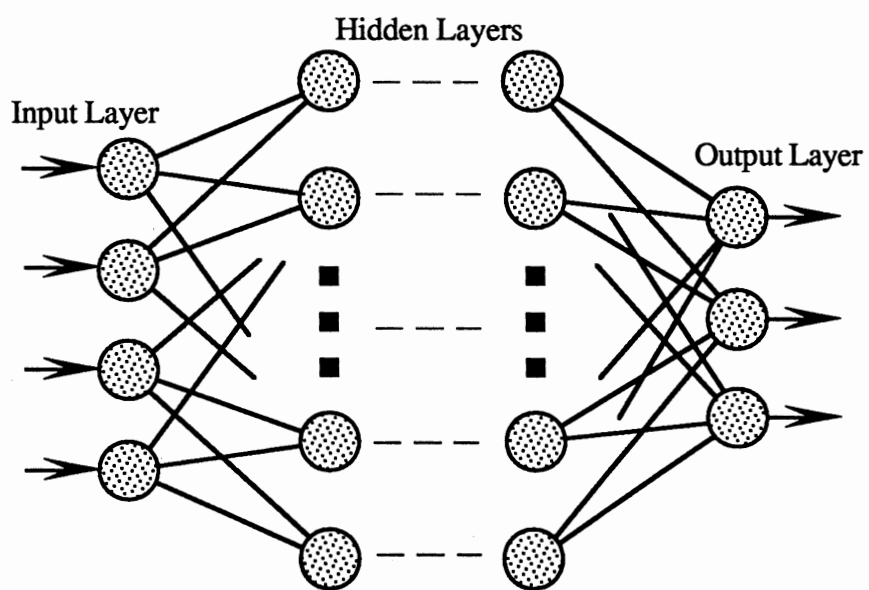


Figure 3.8 Multi-layer BP Neural Network [54].

chosen weights can exactly duplicate those calculations performed by any multi-layer network. Figure 3.9 illustrates the capabilities of a perceptron with one, two, and three layers that use hard limiting nonlinearities. The second column in this figure indicates the types of decision regions that can be formed with different networks. The next two columns present examples of decision regions which could be formed for exclusive OR problem and a problem with meshed regions. The rightmost column gives example of the most general decision regions that can be formed.

Figure 3.9 shows a three-layer perceptron which can form arbitrarily complex decision regions and can separate the meshed classes. It can form regions as complex as those formed using mixture distributions and nearest-neighbor classifiers [44] and can be proven by construction. The proof depends on partitioning the desired decision region into small hypercubes (squares when there are two inputs). Each hypercube requires  $2N$  nodes in the first layer (four nodes when there are two inputs), one for each side of the hypercube, and one node in the second layer that takes the logical AND of the outputs from the first-layer nodes. The outputs of the second layer nodes will be 'high' only for inputs within each hypercube. Hypercubes are assigned to the proper decision regions by connecting the output of each second layer node only to the output node corresponding to the decision regions that node's hypercube is in and performing a logical OR operation in each output node. A logical OR operation will be performed if these connection weights from the second hidden layer to the output layer are one, and threshold in the output nodes are 0.5. This construction procedure can be generalized to use arbitrarily shaped convex regions instead of small hypercubes and capable of generating the disconnected and non-convex regions shown in Figure 3.9.

The above analysis demonstrates that not more than three layers are required in the perceptron like feed forward nets because a three layer network can generate arbitrarily complex decision region. It also provides some insight into the problem of selecting the number of nodes to be used in three layer perceptron. The number of nodes in the second


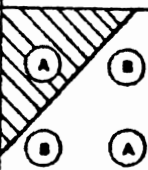
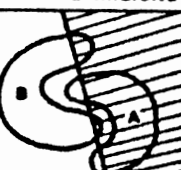


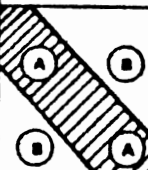



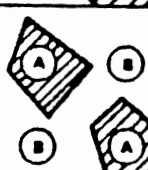
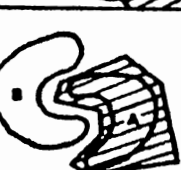

STRUCTURE	TYPES OF DECISION REGIONS	EXCLUSIVE OR PROBLEM	CLASSES WITH MESHEDED REGIONS	MOST GENERAL REGION SHAPES
 SINGLE-LAYER	HALF PLANE BOUNDED BY HYPERPLANE			
 TWO-LAYER	CONVEX OPEN OR CLOSED REGIONS			
 THREE-LAYER	ARBITRARY (Complexity Limited By Number of Nodes)			

Figure 3.9 Types of Decision Regions That can be Formed by Single- and Multi-Layer BP Neural Networks With one and two Layers of Hidden Units and two Inputs [44].

layer must be greater than one, when decision regions are disconnected or meshed and cannot be formed from one convex area. The number of second layer nodes required in the worst case is equal to the number of disconnected regions in input distributions. The number of nodes in the first layer must typically be sufficient to provide three or more edges for each convex area generated by every second layer node. There should, thus, be more than three times as many nodes in the second as in the first layer.

The above discussion centered primarily on multi-layer perceptrons with one output when hard limiting nonlinearities are used. Similar behavior is exhibited by BP network with multiple output nodes when sigmoidal nonlinearities are used and a decision rule is to select the class corresponding to the output node with the largest output. The behavior of these networks is more complex because decision regions are typically bounded by smooth curves instead of by straight line segments and analysis is thus more difficult. These networks, however, can be trained with back propagation algorithm.

#### 3.2.4.1 Function approximation using multi-layer perceptron

The first clear insight into the versatility of neural networks, for use in function approximation came with the discovery of Kolmogorov's theorem [55]. This theorem states that any continuous function of  $N$  variables can be computed using only linear summations and nonlinear but continuously increasing functions of only one variable. This result gave hope that neural networks would turn out to be able to approximate any functions that arise in the real world. The following results by Hatch-Nielson [55] and others showed that BP network capable of implementing any function of practical interest to any desired degree of accuracy.

### 3.3 Application of Pattern Recognition in Tool Wear Monitoring

An essential step in the design and control of many mechanical systems involves modeling of the system dynamics. As mentioned earlier, one method which does not

require any model is the pattern recognition and mapping technique using neural network paradigms. In this section, the methods of sensor integration using different neural network paradigms, discussed in the last section, are investigated.

Let  $T$  and  $M$  be the sensor signals from two different sensors, e. g., the thrust and torque sensors. The problem is to monitor the tool wear progress. The signals from these two sources, can be assigned to one of the following classes.

- Signals related to worn tool.
- Signals due to tool fracture.
- All other signals (including those from sharp tool).

The partitioning or classification process can be implemented using one of the methods explained in the last section or other similar methods. There are three methods of sensor signal classification:

1. Classification using clustering technique.
2. Classification using mapping technique.
3. Classification using decision surfaces.

These techniques are described in more details in the following.

### 3.3.1 Classification using clustering technique

Figure 3.10 shows the working principal of the clustering technique. As seen, the classes are not linearly separable. This is the main problem associated with this method. To solve this problem, the whole domain of each class is divided into small subclasses. Figure 3.10 shows the implementation of this technique. Table 3.1 shows the training data set. During the course of training, the state of tool wear for each set of sensor signals is known. For example,  $T_N$  and  $M_N$  belong to a worn tool (see Table 3.1). During training they may be merged to subclass number  $S_n$  (see Figure 3.10), for example, using ART2 network. Therefore, whenever subclass number  $S_n$  is set during operation, it is an indication of worn tool. Each state of tool wear, namely, worn tool, sharp tool, and tool

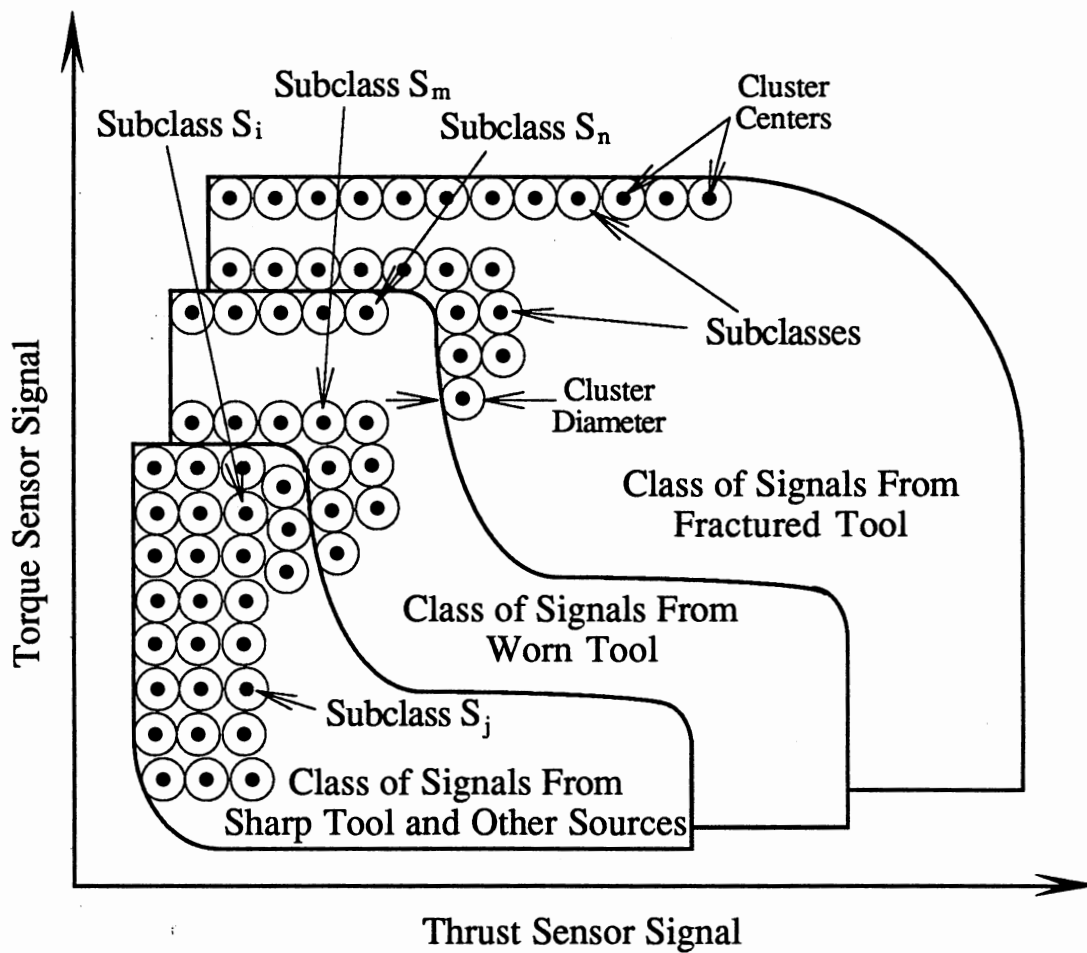


Figure 3.10 Classification of Sensor Signals Based on Clustering Technique.

TABLE 3.1  
TRAINING DATA SET

Wear Land	Tool Condition	Thrust Signal	Torque Signal	Subclass Number After Training
$w_1$	Sharp	$T_1$	$M_1$	$S_i$
$w_2$	Sharp	$T_2$	$M_2$	$S_j$
.....	.....	.....	.....	
.....	.....	.....	.....	
$w_{N-1}$	Worn	$T_{N-1}$	$M_{N-1}$	$S_m$
$w_N$	Worn	$T_N$	$M_N$	$S_n$



fracture are represented by a number of subclasses (for more clarification see  $S_i$ ,  $S_j$ ,  $S_m$ , and  $S_n$  of Table 3.1 and Figure 3.10).

The size of a subclass is a very important factor. The smaller the size of the subclasses, the finer the domain each class can be divided, and more accurate the classification. But as the size of the subclasses decreases, the structure of the neural network becomes more complicated due to increasing number of subclasses. The size of the subclasses is defined by vigilance parameter sources in ART2 network. In Kohonen network, the number of subclasses is determined before training. In this case, the sizes of the subclasses are not the same and the probability distribution of the data determines their sizes.

### 3.3.2 Classification using mapping technique

The second classification uses mapping technique. As mentioned in the last section, BP network is capable of approximating any function. Figure 3.11 shows how BP network can address the problem of tool wear classification. In this method, some value is assigned to each class of the state of tool wear. For example, a is assigned to a sharp tool, b to a worn tool and c to a fractured tool. During training of BP network a, b, and c are used as targets. When the network is operational, if the output of network is b then it indicates the tool is worn.

### 3.3.3 Classification using decision surfaces

As shown in Figure 3.9, BP can classify any complicated region using decision surfaces. It is possible to design a BP network with three outputs (Figure 3.12), each of them represents one of the classes, namely, sharp tool, worn tool, and tool fracture. After training, one of these three outputs will be set to indicate the state of tool wear associated with the input signals. Figure 3.12 shows structure of BP network that classifies sensor signals using the decision surfaces technique.

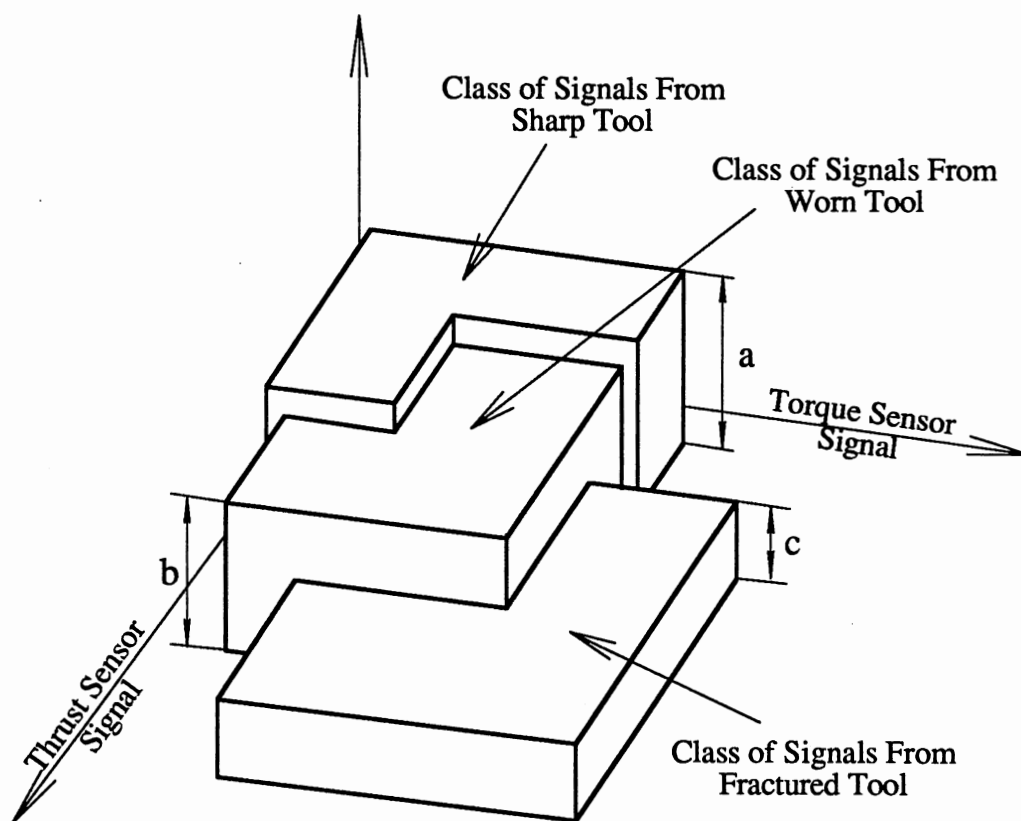


Figure 3.11 Classification of Sensor Signals Based on Mapping Technique.

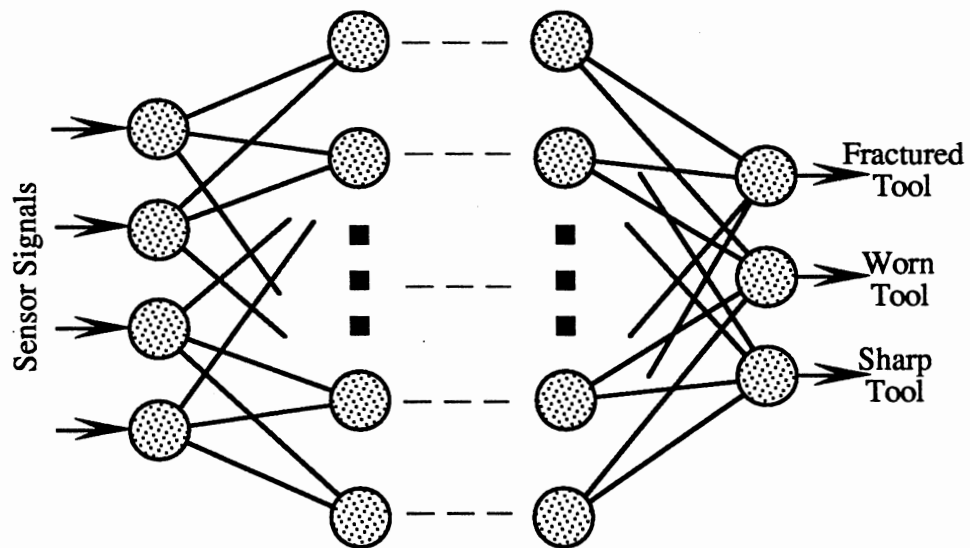


Figure 3.12 BP Network Structure for Classification of Sensor Signals Using Decision Surfaces Technique.

### 3.4 Tool Wear Estimation Using Mapping Technique

Sometimes we are interested in predicting the exact magnitude of the wear land on the tool. The magnitude of wear is useful for an artificial intelligent system (AI) to determine the optimum cutting speed and feed rate. In this case, wear may be estimated by the evaluation of sensor signals as shown by the following equation

$$w = f(T, M) \quad (3.4)$$

As mentioned in the last section, BP network is able to approximate any type of function, i. e. map inputs to outputs. Therefore, one approach is to use BP network for this purpose. Clustering technique can also be used for this case. Figure 3.13 shows how the clustering technique can model the above equation. In the clustering technique, each magnitude of wear is assigned a class. For example, in Table 3.1, thrust and torque signals,  $T_N$  and  $M_N$  associated with  $w_N$ , magnitude of wear. During training, these signals, namely, thrust and torque may be merged to class number  $S_n$  (see Figure 3.13). When the network is operational if class  $S_n$  is set. It means the magnitude of wear is  $w_N$ .

As can be seen, all three methods can address the problem of tool wear classification, and clustering and mapping techniques can estimate tool wear. The advantage of ART2 neural networks is, it uses an unsupervised learning (learning without teacher) and can learn on-line (while the network is operational). In contrast, BP network uses supervised learning and it should be trained before use. If the shape of the classes is very complicated, the size of the subclasses should be very small, which requires a considerable number of subclasses to cover each class. This leads to a large size ART2 network. But BP network needs smaller size for this case. Therefore, if enough data for training is available, BP network is better than using networks based on clustering techniques.

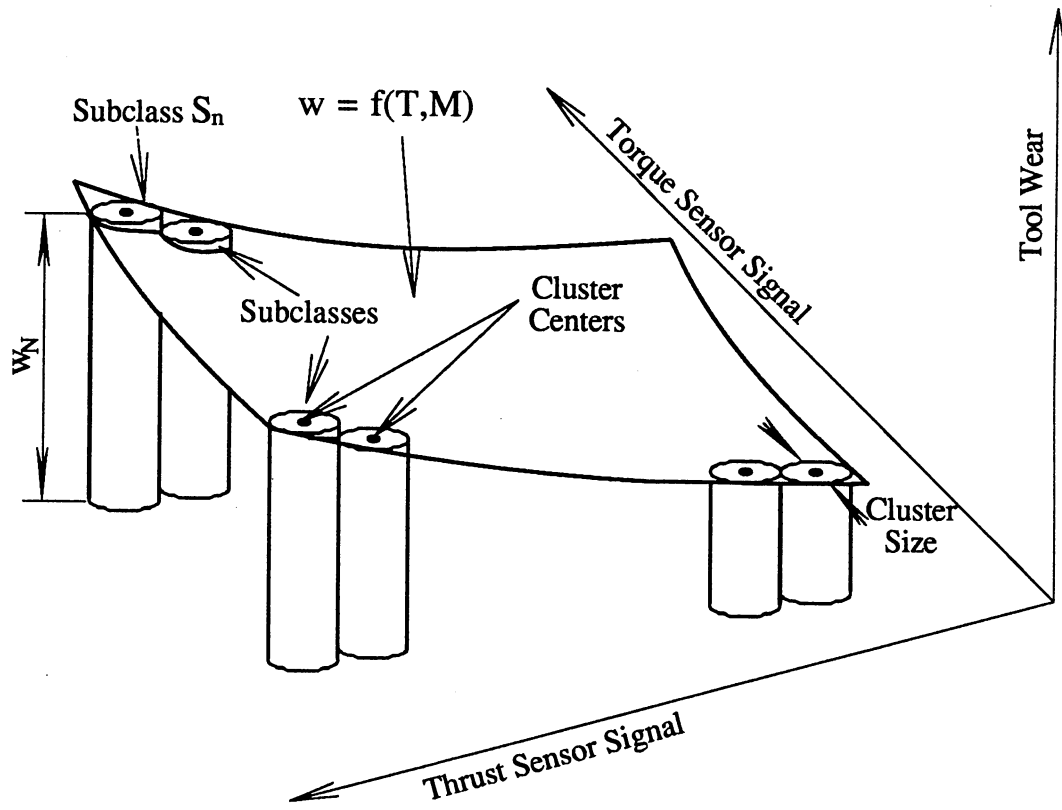


Figure 3.13 Modeling  $w = f(T, M)$ .

### 3.5 Conclusions

In this Chapter, a review of parameter estimation and pattern recognition and their application to tool wear monitoring in metal cutting are investigated. First, it was shown how parameter estimation works in the case of tool wear monitoring. This was followed by a review of the application of pattern recognition. Some researchers [43] have used a combination of both techniques. i. e. inputs to the neural network are estimated parameters of the system. In this investigation, it was shown that in a drilling process only gain of the system is changing while all the other parameters of the system remain constant with the development of tool wear (see Chapter V for details). It was also assumed that the classes can be separated by some boundaries. i. e. no member of a given class is in the domain of the other class. As long as this assumption is valid, pattern recognition technique may be applicable. In this investigation it was shown that in the drilling process, the member of different classes are mixed (see Chapter VI for details). Therefore the application of pattern recognition technique is somewhat difficult for drill wear estimation.

## CHAPTER IV

### REVIEW OF SIGNAL ANALYSIS

Time domain representation of a signal which gives the temporal variation of the signal amplitude and may be transformed into the frequency domain through power spectral density (PSD) analysis. PSD analysis decomposes the original signal into a sum of powers of sinusoidal waveforms at different frequencies. The advantage of this decomposition is that it enables one to examine how the power of the signal at different frequencies varies with changes in the source mechanism generating the signal. Thus, it provides a description of the signal characteristics which may not be evident in the original time domain.

Periodogram, which is the square of the absolute of the Fourier transform of a finite duration of a random process, is a biased estimate of PSD and its standard deviation at each frequency is of the same order as its mean at the same frequency. This fact was ignored by most of the researchers in metal cutting. This chapter gives an overview of the theories behind spectral estimation using the periodograms.

#### 4.1 Spectral Estimation

Let  $x_T(t)$  be a sample of a stationary random process  $x(t)$ , then its PSD is given by

$$S(\omega) = \int_{-\infty}^{+\infty} R(\tau)e^{-j\omega\tau}d\tau \quad (4.1)$$

where

$$R(\tau) = E\{x(t)x(t+\tau)\} = \lim_{T \rightarrow \infty} \frac{1}{T - \tau} \int_0^{T-\tau} x(t)x(t+\tau)dt \quad (4.2)$$

$R(\tau)$  is the autocorrelation function of  $x(t)$ . However, since  $x(t)$  is usually available only for a finite duration of time segment  $T$ , the above product is known for  $t < T - \tau$  (Figure 4.1). Therefore, the above equation should be changed to

$$R^T(\tau) = E\{x(t)x(t+\tau)\} = \frac{1}{T - \tau} \int_0^{T-\tau} x(t)x(t+\tau)dt \quad (4.3)$$

and PSD is

$$S^T(\omega) = \int_{-T}^{+T} R^T(\tau)e^{-j\omega\tau}d\tau \quad (4.4)$$

$S^T(\omega)$  is not a reliable estimate of  $S(\omega)$ . Although  $R^T(\tau)$  is an unbiased estimate of  $R(\tau)$ ,

$$E\{R^T(\tau)\} = R(\tau) \quad |\tau| < T \quad (4.5)$$

But,  $S^T(\omega)$  is not an unbiased estimate of  $S(\omega)$  because its inverse is zero for  $|\tau| > T$ . However, this is not the main problem. In Equation 4.3, the length of integration equals  $T - |\tau|$  and it approaches zero as  $|\tau|$  approaches  $T$ . Hence, the variance of  $R^T(\tau)$  is large for  $|\tau|$  close to  $T$ . And since all values of  $\tau$  are used in equation 4.4, the variances of  $S^T(\omega)$  is large for any  $T$ . In the following, the underlying theory using  $R_T(\tau)$ , as estimate of  $R(\tau)$ , a modified form of Equation 4.3 will be developed.



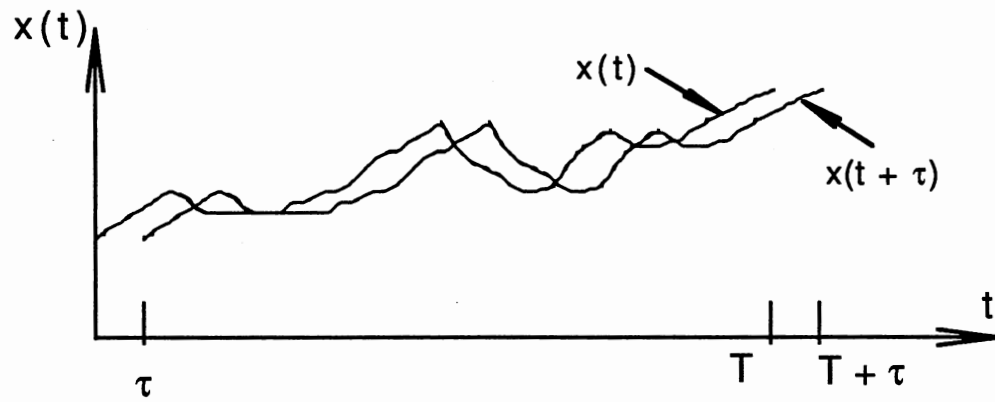


Figure 4.1  $x(t)$  and  $x(t+\tau)$  Signals [56].

$$R_T(\tau) = E\{x(t)x(t+\tau)\} = \frac{1}{T} \int_0^{T-\tau} x(t)x(t+\tau)dt \quad (4.6)$$

This is so because, unlike  $S^T(\omega)$ , the Fourier transform of  $R_T(\tau)$  is given by

$$S_T(\omega) = \int_{-T}^{+T} R_T(\tau)e^{-j\omega\tau}d\tau \quad (4.7)$$

and can be expressed directly in terms of  $x_T(t)$ . Indeed, the integral in Equation 4.6 equals the convolution of  $x(\cdot)$  and  $x(\cdot)$ , i. e.

$$R_T(\tau) = \frac{1}{T} x_T(\tau)*x_T(\tau) \quad (4.8)$$

From this and the convolution theorem it follows that

$$S_T(\omega) = \frac{1}{T} |X_T(\omega)|^2 \quad (4.9a)$$

$$X_T(\omega) = \int_0^T x(t)e^{-j\omega t}dt \quad (4.9b)$$

The process so formed is called *sample spectrum* or *periodogram*. It should be noted that the limits of integral in Equation 4.6 are not infinity. However, since  $x(t) = 0$  for  $t < 0$  and  $t > T$  this limit can be changed to infinity. Applying, now the convolution theorem to Equations 4.6, we get Equations 4.8 and 4.9. The limits of the integral in Equation 4.9b are now changed from infinity to 0 and  $T$  due to the fact mentioned above.

It is usually convenient to represent a finite duration of a signal in discrete time form,  $x(n)$ . The Fourier transform of such a representation is referred to as discrete Fourier transform (DFT) of the sequence. In this way, if  $x(n)$  is a sequence defined only over the interval from 0 to  $N-1$ , the DFT,  $X(\omega_k)$ , of  $x(n)$  is defined only over the same interval from 0 to  $N-1$  by

$$X_N(\omega_k) = \sum_{n=0}^{N-1} x(n)e^{-j\omega_k n} \quad (4.10a)$$

where  $\omega_k = 2\pi k/N$  which is the discrete time frequency and it is between  $-\pi$  and  $\pi$ . The corresponding continuous time frequency is obtained by  $\Omega_k = f_s \omega_k$  where  $f_s$  is sampling rate (frequency) of the signal in Hz. Discrete time periodogram is defined by

$$S_N(\omega_k) = \frac{1}{N} (|X_N(\omega_k)|^2) \quad \text{for } k=0 \text{ or } N/2 \quad (4.10b)$$

#### 4.2 Mean and Variance of Periodogram

The Fourier integral of a stochastic process  $x(t)$  is a stochastic process in the variable  $\omega$  given by [56]

$$X(\omega) = \int_{-\infty}^{+\infty} x(t)e^{-j\omega t} dt \quad (4.11)$$

The mean of  $X(\omega)$  is

$$E\{X(\omega)\} = \int_{-\infty}^{+\infty} E\{x(t)\}e^{-j\omega t} dt \quad (4.12)$$

Therefore, if  $x(t)$  is a zero mean process then the mean of  $X(\omega)$  is also a zero process. Hereafter, without loss of generality,  $x(t)$  is assumed to be a zero mean stationary random process. Autocorrelation  $X(\omega)$  is given by

$$E\{X(\omega_1)X^*(\omega_2)\} = \Gamma(\omega_1, -\omega_2) \quad (4.13)$$

where  $X^*(\omega_2)$  is the conjugate of  $X(\omega_2)$  and  $\Gamma(\omega_1, \omega_2)$  is a two dimensional Fourier transform defined by

$$\Gamma(\omega_1, \omega_2) = \int_{-\infty}^{+\infty} \int_{-\infty}^{+\infty} E\{x(t_1)x^*(t_2)\} e^{-j(\omega_1 t_1 + \omega_2 t_2)} dt_1 dt_2 \quad (4.14)$$

where  $x^*(t_2)$  is a conjugate of  $x(t_2)$ . For a stationary random process

$$E\{x(t_1)x^*(t_2)\} = R(t_1 - t_2) \quad (4.15)$$

If  $x(t)$  is a wide sense stationary (WSS) random process (i. e. Eq. 4.15 is valid) then  $X(\omega)$  is white noise. To show this,  $\Gamma(\omega_1, -\omega_2)$  is evaluated assuming  $t_1 = t_2 + \tau$  (see Eq. 4.13)

$$\begin{aligned} \Gamma(\omega_1, -\omega_2) &= \int_{-\infty}^{\infty} \int_{-\infty}^{\infty} R(t_1 - t_2) e^{-j(\omega_1 t_1 - \omega_2 t_2)} dt_1 dt_2 \\ &= \int_{-\infty}^{\infty} e^{-j(\omega_1 - \omega_2)t_2} \left( \int_{-\infty}^{\infty} R e^{-j\omega_1 \tau} d\tau \right) dt_2 = S(\omega_1) \int_{-\infty}^{\infty} e^{-j(\omega_1 - \omega_2)t_2} dt_2 \end{aligned}$$

$$E\{X(\omega_1)X^*(\omega_2)\} = \Gamma(\omega_1, -\omega_2) = S(\omega_1)\delta(\omega_1 - \omega_2) \quad (4.16)$$

Since  $X(\omega_1)$  and  $X^*(\omega_2)$  are uncorrelated,  $|X(\omega_1)|^2$  and  $|X(\omega_2)|^2$  are also uncorrelated. Estimation in Eq. 4.16 is unbounded when  $\omega_1 = \omega_2 = \omega$  because  $\delta(\omega - \omega)$  is infinity. It can be shown that, by setting  $\tau = t_1 - t_2$  and  $\omega_1 = \omega_2 = \omega$

$$\begin{aligned} \lim_{T \rightarrow \infty} \frac{1}{T} \Gamma_T(\omega, -\omega) &= \lim_{T \rightarrow \infty} \frac{1}{T} \int_{-T}^T \int_{-T}^T R(t_1 - t_2) e^{-j\omega(t_1 - t_2)} dt_1 dt_2 \\ &= \int_{-\infty}^{\infty} R(\tau) e^{-j\omega\tau} d\tau \end{aligned} \quad (4.17)$$

From Equations 4.1, 4.13, 4.9a and 4.17, we have

$$S(\omega) = \lim_{T \rightarrow \infty} \frac{1}{T} \Gamma_T(\omega, -\omega) = \lim_{T \rightarrow \infty} E\left\{\frac{1}{T} |X_T(\omega)|^2\right\} = \lim_{T \rightarrow \infty} E\{S_T(\omega)\} \quad (4.18)$$

It means that mean of  $S_T(\omega)$  approaches  $S(\omega)$  as  $T$  goes to infinity. Fourier transform of a process  $x(t)$  is, in general, complex

$$X(\omega) = A(\omega) + jB(\omega) \quad (4.19)$$

and may be expressed in terms of the real and imaginary parts of the following two dimensional Fourier transforms (see Equations.4.13 and 4.14)

$$\begin{aligned} E\{X(\omega_1)X^*(\omega_2)\} &= \Gamma_r(\omega_1, -\omega_2) + j\Gamma_i(\omega_1, -\omega_2) \\ E\{X(\omega_1)X(\omega_2)\} &= \Gamma_r(\omega_1, \omega_2) + j\Gamma_i(\omega_1, \omega_2) \end{aligned} \quad (4.20)$$

From Eq. 4.19 and 4.20, we can obtain

$$2E\{A(\omega_1)A(\omega_2)\} = \Gamma_r(\omega_1, -\omega_2) + \Gamma_r(\omega_1, \omega_2)$$

$$2E\{A(\omega_1)B(\omega_2)\} = \Gamma_i(\omega_1, \omega_2) - \Gamma_i(\omega_1, -\omega_2)$$

$$2E\{B(\omega_1)B(\omega_2)\} = \Gamma_r(\omega_1, -\omega_2) - \Gamma_r(\omega_1, \omega_2)$$

$$2E\{A(\omega_2)B(\omega_1)\} = \Gamma_i(\omega_1, -\omega_2) + \Gamma_i(\omega_1, \omega_2) \quad (4.21)$$

The covariance of  $|X(\omega)|^2$  can not, in most cases, be expressed in terms of  $\Gamma(\omega_1, \omega_2)$  because it involves fourth order moments. The normal case, however, is an exception. It can be shown that, the difference between the fourth order moment of  $x(t)$  and of the normal process with the same spectrum can be neglected if  $T$  is sufficiently large [56]. Therefore,  $x(t)$  is assumed to be normal with zero mean. Covariance of  $|X(\omega)|^2$ , using Equation 4.20, is

$$\begin{aligned} \text{cov}\{|X(\omega_1)|^2, |X(\omega_2)|^2\} &= E\{|X(\omega_1)|^2 |X(\omega_2)|^2\} - E\{|X(\omega_1)|^2\} E\{|X(\omega_2)|^2\} \\ &= E\{[A^2(\omega_1) + B^2(\omega_1)][A^2(\omega_2) + B^2(\omega_2)]\} \\ &\quad - E\{A^2(\omega_1) + B^2(\omega_1)\} E\{A^2(\omega_2) + B^2(\omega_2)\} \quad (4.22) \end{aligned}$$

If  $x$  and  $y$  are jointly normal process, we can write [56]

$$E\{x^2 y^2\} = E\{x^2\} E\{y^2\} + 2E^2\{xy\} \quad (4.23)$$

Using Eq. 4.23, Eq. 4.22 can be simplified to

$$\begin{aligned} \text{cov}\{|X(\omega_1)|^2, |X(\omega_2)|^2\} &= 2E^2\{A(\omega_1)A(\omega_2)\} + 2E^2\{B(\omega_1)B(\omega_2)\} \\ &\quad + 2E^2\{A(\omega_1)B(\omega_2)\} \\ &\quad + 2E^2\{A(\omega_2)B(\omega_1)\} \quad (4.24) \end{aligned}$$

Since  $A(\omega)$  and  $B(\omega)$  are zero mean jointly normal process. Substituting Equation 4.20 into Equation 4.24, we obtain

$$\text{cov}\{|X(\omega_1)|^2, |X(\omega_2)|^2\} = |\Gamma(\omega_1, -\omega_2)|^2 + |\Gamma(\omega_1, \omega_2)|^2 \quad (4.25)$$

From Eq. 4.25, we have

$$\text{var}\{|X(\omega)|^2\} \geq |\Gamma(\omega, -\omega)|^2 \quad (4.26)$$

From Eq. 4.17

$$\lim_{T \rightarrow \infty} \text{var}\left\{\frac{1}{T}|X_T(\omega)|^2\right\} \geq \lim_{T \rightarrow \infty} \left|\frac{1}{T}\Gamma_T(\omega, -\omega)\right|^2 \quad (4.27)$$

and finally from Eq. 4.18 and 4.9a, we have

$$\lim_{T \rightarrow \infty} \text{var}\{S_T(\omega)\} = \lim_{T \rightarrow \infty} \text{var}\left\{\frac{1}{T}|X_T(\omega)|^2\right\} \geq (S(\omega))^2 \quad (4.28)$$

This equation shows that variance of the periodogram is of the same order as the square of its mean.

In summary, for a stationary random process, mean of  $S_T(\omega)$  converges to  $S(\omega)$  as  $T$  goes to infinity (Eq. 4.17),  $\text{var}\{S_T(\omega)\}$  is very large, i. e. it is equal to or greater than the square of actual magnitude of PSD  $((S(\omega))^2)$  (Eq. 4.28), and finally  $S_T(\omega_1)$  and  $S_T(\omega_2)$  are uncorrelated (Equations 4.16 and 4.9a). Therefore, it appears that the PSD analysis performed by other researchers in metal cutting [10,12,14,15] by not considering these facts may not be reliable.

### 4.3 Data Windowing

As indicated in Section 4.1, a finite duration of the signal,  $x(n)$ , is used, since the input to the discrete time Fourier transform (DFT) must be of a finite duration. This is called data windowing. For example, the mathematical representation of a rectangular window, which is just a simple selection of a finite selection of the signal, is given by

$$v(n) = x(n)w(n) \quad (4.29a)$$

where  $w(n)$  for a rectangular window is given by

$$w(n) = \begin{cases} 1 & \text{for } 0 \leq n < N \\ 0 & \text{otherwise} \end{cases} \quad (4.29b)$$

The effect on frequency domain is a periodic convolution, i.e.

$$V(e^{j\omega}) = \frac{1}{2\pi} \int_{-\pi}^{\pi} X(e^{j\theta})W(e^{j(\omega-\theta)})d\theta \quad (4.30)$$

$W(e^{j\omega})$  for a 64 data points is shown in Figure 4.2a. Figures 4.2b to 4.2d show absolute of DFT for

$$v(n) = A_0 \cos(\omega_0 n + \varphi_0) + A_1 \cos(\omega_1 n + \varphi_1) \quad (4.31)$$

where  $A_0 = 1$ ,  $A_1 = 0.75$  and  $\omega_0$  and  $\omega_1$  change for different cases. For Figure 4.2b they are  $2\pi/14$  and  $4\pi/15$  respectively; for Figure 4.2c  $2\pi/14$  and  $2\pi/12$ ; and for Figure 4.2d  $2\pi/14$  and  $4\pi/25$ . In Figure 4.2b there is an overlap between the window



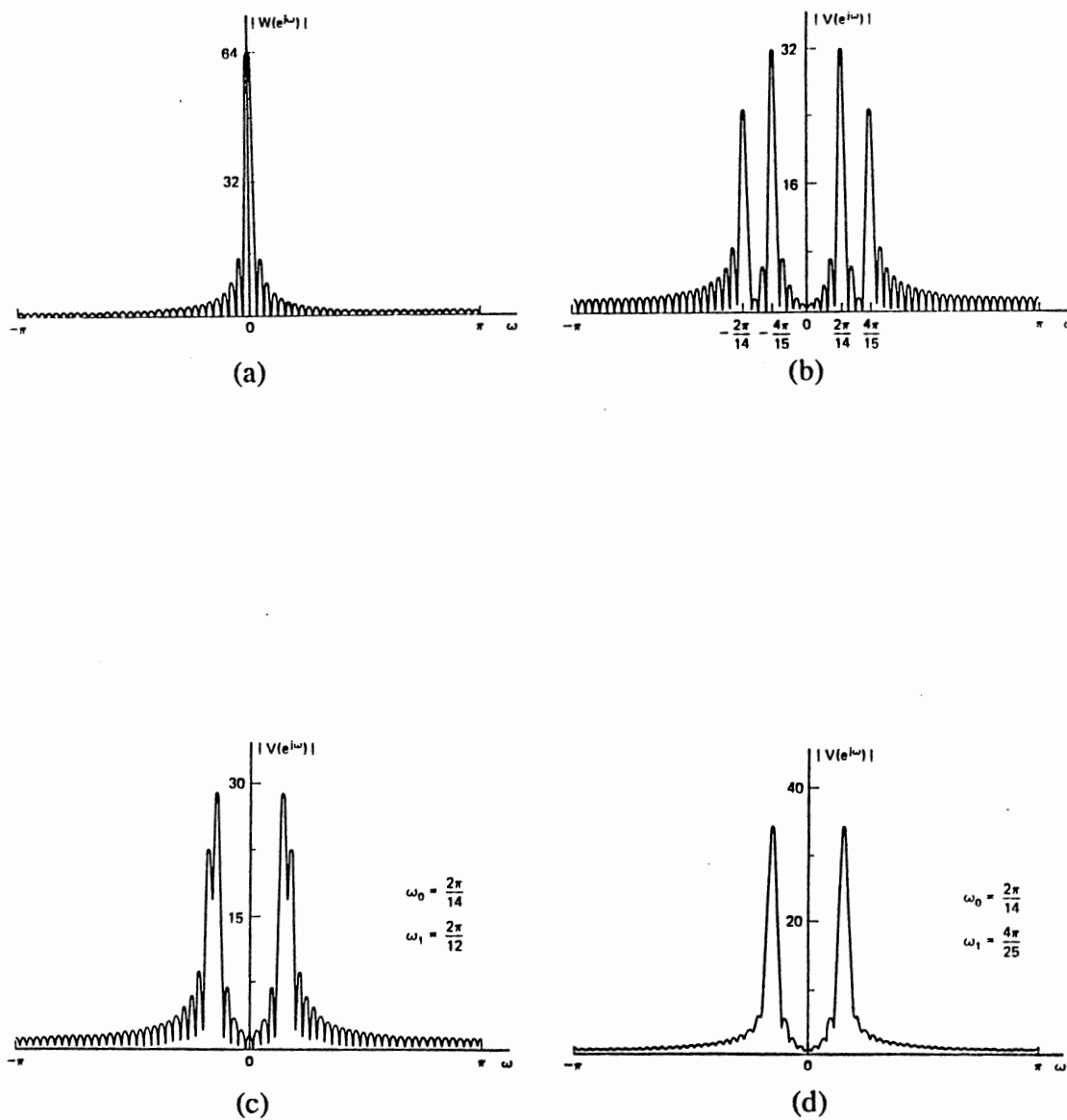


Figure 4.2 Illustration of Fourier Analysis of Windowed Cosines with Rectangular Window. (a) Fourier transform of window (b)-(d) Fourier transform of windowed cosines as the frequency spacing becomes progressively smaller. (b)  $\omega_0 = 2\pi/14$ ,  $\omega_1 = 4\pi/14$ . (c)  $\omega_0 = 2\pi/14$ ,  $\omega_1 = 2\pi/12$ . (d)  $\omega_0 = 2\pi/14$ ,  $\omega_1 = 4\pi/25$ . [57]

replicates at  $\omega_0$  and  $\omega_1$  while two distinct peaks are present, the amplitude of the spectrum at  $\omega = \omega_0$  is affected by the amplitude of the sinusoidal signal at  $\omega = \omega_1$  and vice versa. This interaction is called *leakage*. i. e. the component at one frequency leaks into the vicinity of another component due to spectral smearing introduced by the window. Figure 4.2c shows the case where the leakage is even greater and how sidelobes adding out of phase can reduce the height of the peaks. In Figure 4.2d, the overlap between the spectral windows at  $\omega_0$  and  $\omega_1$  is so significant that the two peaks visible in 4.2b and 4.2c have merged into one. In other words, with this window, the two frequencies corresponding to Figure 4.2d can not be *resolved* in the spectrum.

Reduced resolution and leakage are the two primary effects on the spectrum as a result of applying a window to the signal. The resolution is primarily influenced by the width of the mainlobe of  $W(e^{j\omega})$ , while the degree of leakage depends on relative amplitude of the mainlobe and the sidelobes of  $W(e^{j\omega})$ . The width of the mainlobe and the relative sidelobe amplitude depend primarily on the window length and the shape (amount of tapering) of the window. The rectangular window, with a Fourier transform (Figure 4.2a)

$$W_r(e^{j\omega}) = e^{j\omega(N-1)/2} \frac{\sin(\omega N/2)}{\sin(\omega/2)} \quad (4.32)$$

has the narrowest mainlobe for a given length. On the other hand, sidelobes of rectangular window is largest of the all commonly used windows.

Some commonly used windows are shown in Figure 4.3. These windows are defined by the following equations (Equation is 4.29 for a rectangular window):

Bartlett (triangular)

$$w(n) = \begin{cases} 2n/N & \text{for } 0 \leq n \leq N/2 \\ 2-2n/N & \text{for } N/2 < n \leq N \\ 0 & \text{otherwise} \end{cases} \quad (4.33a)$$

Hanning

$$w(n) = \begin{cases} 0.5(1 - \cos(2\pi n/N)) & \text{for } 0 \leq n \leq N \\ 0 & \text{otherwise} \end{cases} \quad (4.33b)$$

Hamming

$$w(n) = \begin{cases} 0.54 - 0.46\cos(2\pi n/N) & \text{for } 0 \leq n \leq N \\ 0 & \text{otherwise} \end{cases} \quad (4.33c)$$

Blackman

$$w(n) = \begin{cases} 0.42 - 0.5\cos(2\pi n/N) + 0.08\cos(4\pi n/N) & \text{for } 0 \leq n \leq N \\ 0 & \text{otherwise} \end{cases} \quad (4.33d)$$

Figures 4.4 (a) to (e) show the plots of the function  $20 \log_{10}|W(e^{j\omega})|$  for each of these windows with  $N = 50$ . The rectangular window clearly has the narrowest mainlobe and thus, for a given length, it has the best resolution among these windows. However, the first sidelobe is only about 13 db below the main peak, resulting in highest degree of leakage. As can be seen from Figure 4.4 by tapering the widow smoothly to zero as with the Hamming, Hanning, and Blackman the sidelobes are greatly reduced; however, the trade off is a much wider mainlobe and thus worse resolution.

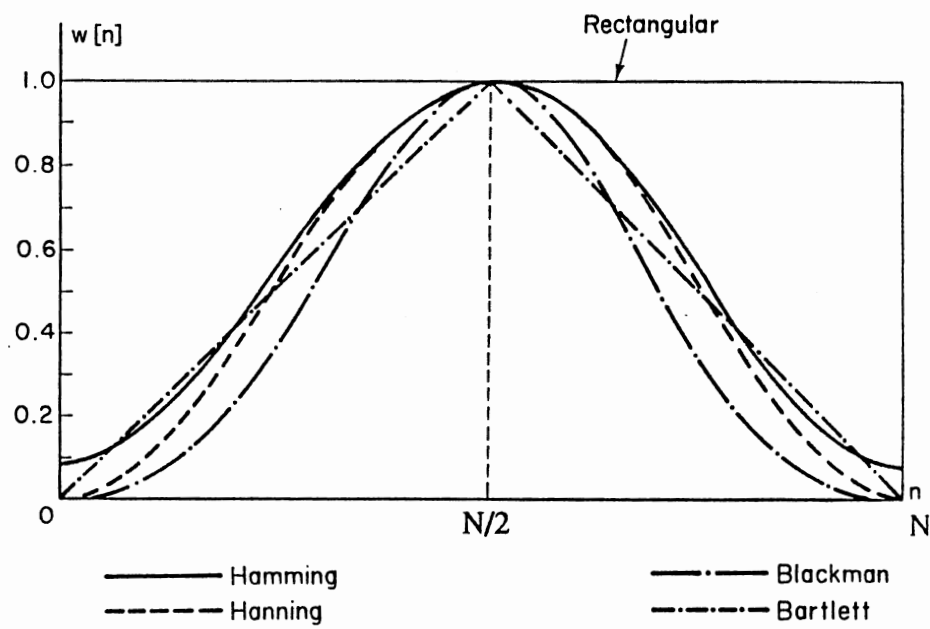


Figure 4.3 Commonly Used Windows [57].

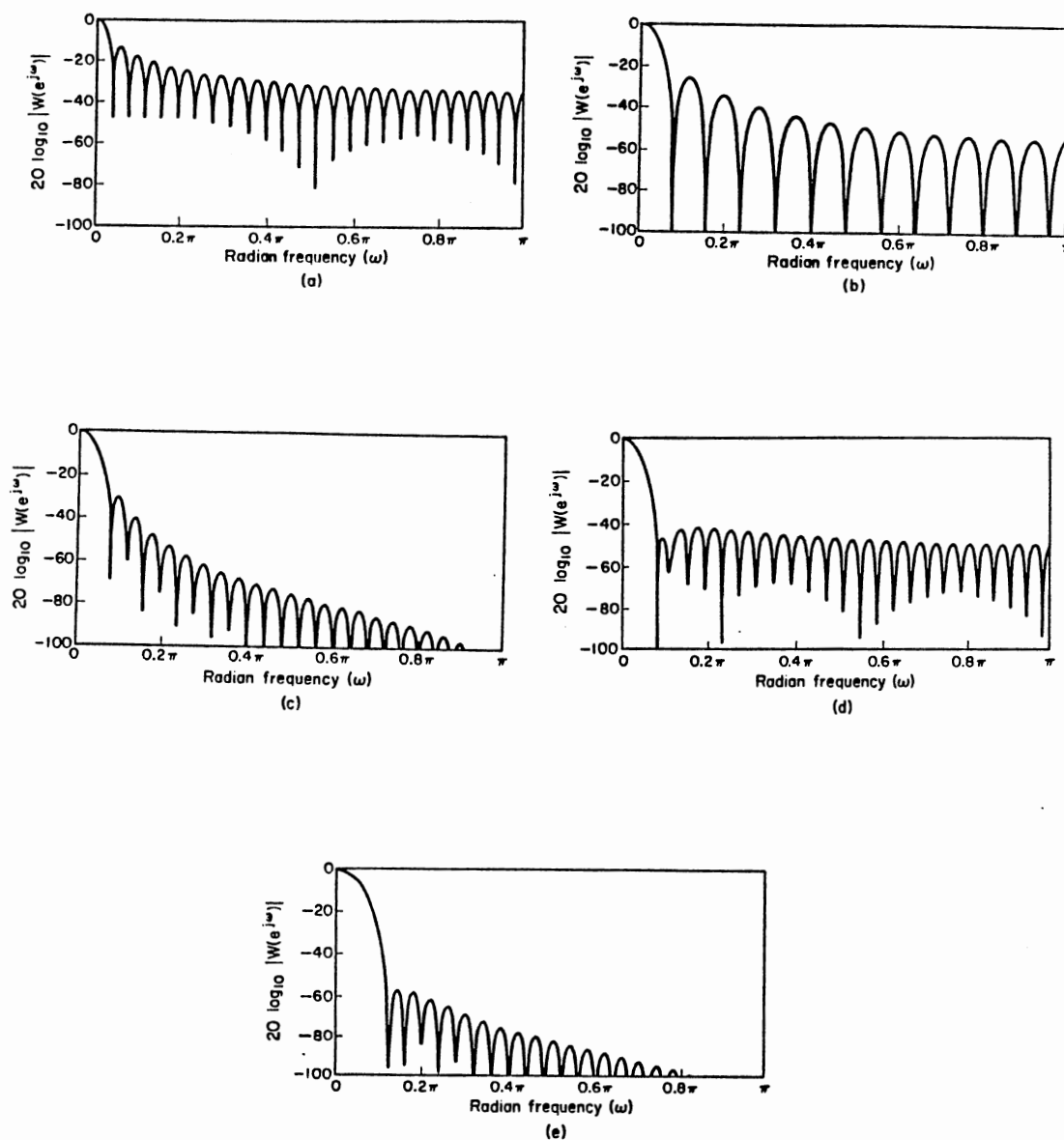


Figure 4.4 Fourier Transforms (Log Magnitude) of Windows of Figure 4.3 [57].  
 (a) Rectangular. (b) Bartlett. (c) Hanning. (d) Hamming  
 (e) Blackman.

#### 4.4 Smoothing the Periodogram

The averaging of the periodograms by spectrum estimation was studied extensively by Bartlett ; subsequently, after the fast algorithms for computing the DFT were developed, Welch [58] combined these computational algorithms with the use of a data window  $w(n)$  to develop the method of averaging modified periodograms (when window is not rectangular it is referred to as modified periodogram).

In the periodogram averaging method proposed by Bartlett, the whole data sequence  $x(q)$  of length  $Q$  is divided into segments of data sequence,  $x_m(n)$  of length  $N$  data points (see Figure 4.5),i. e.

$$x_m(n) = x(mN + n) \quad m = 0, 1, 2 \dots M \text{ and } 0 \leq n \leq N-1 \quad (4.34)$$

where  $M$  is the integer part of  $(Q/N) - 1$ . If the lengths taken consecutively as contiguous portions of one total length of series, the correlation between the two periodograms ( $S_{N_i}(\omega_k)$  and  $S_{N_j}(\omega_k)$ ) will be negligible as the length  $N$  of each portion increases, provided  $R(\tau)$  decreases fast enough as  $\tau$  increases. For example, even between adjacent portions, we have

$$E\{X_{N_1}(\omega_k)X_{N_2}^*(\omega_k)\} = \sum_{n_1=1}^N \sum_{n_2=N+1}^{2N} x(n_1)x(n_2)e^{-j(n_1 - n_2)\omega_k} \quad (4.35)$$

After some algebraic manipulations [59], we get

$$E\left\{\frac{1}{N}X_{N_1}(\omega_k)X_{N_2}^*(\omega_k)\right\} = 2 \sum_{\tau=-N+1}^{N-1} \left(1 - \frac{|\tau|}{N}\right)R(N+\tau)e^{j\tau\omega_k} \quad (4.36)$$

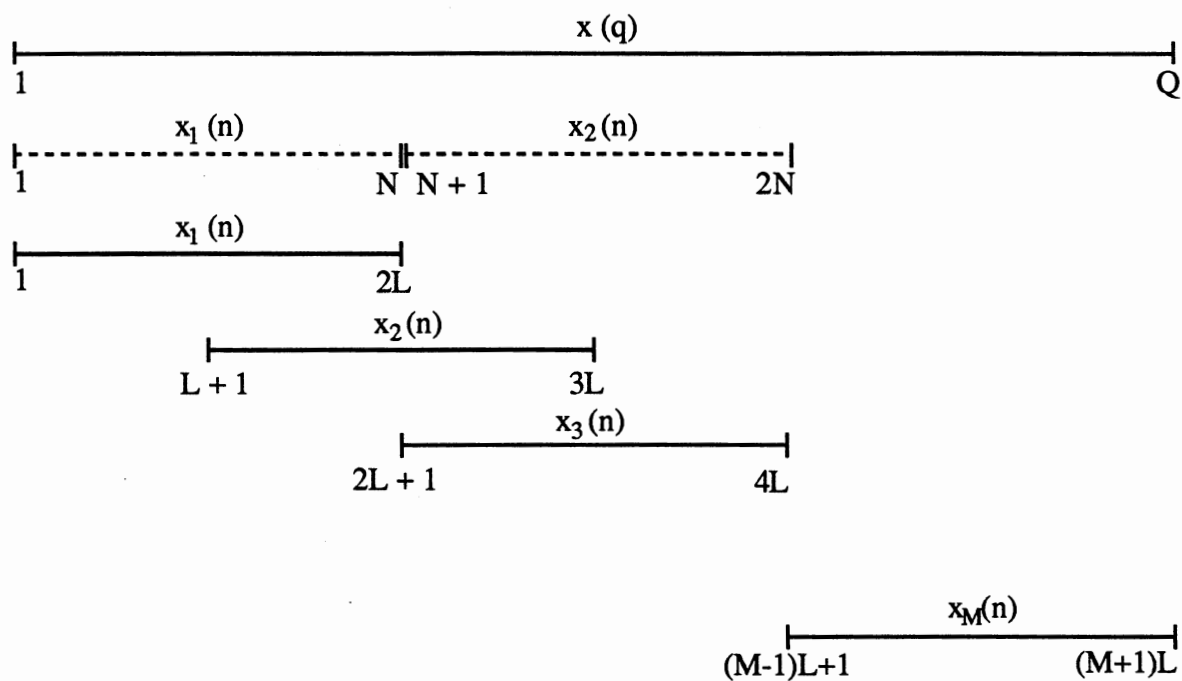


Figure 4.5 Data Segmentation for Periodogram Averaging [58].  
 ( - - ) Bartlett method, ( — ) Welch method.

where  $X_{N_1}(\omega_k)$  and  $X_{N_2}^*(\omega_k)$  are obtained from two consecutive portions, and this expression tends to zero as  $N$  increases, provided  $R(N+\tau)$  is of the order of  $(1/N)$  for fixed  $\tau$ . Therefore, periodograms of every two segments of data are uncorrelated. To examine the variance, we use the fact that in general the variance of the sum of  $M$  independent (uncorrelated), identically distributed, random variables is  $1/M$  times the variance of each individual random variable. Therefore, the variance of the average periodogram is given by

$$\text{var}\{\bar{S}_N(\omega_k)\} = \frac{1}{M}\text{var}\{S_{N_m}(\omega_k)\} \quad (4.37)$$

where

$$\bar{S}_N(\omega_k) = \frac{1}{M} \sum_{m=1}^M S_{N_m}(\omega_k) \quad (4.38a)$$

and

$$S_{N_m}(\omega_k) = \frac{1}{N} |X_{N_m}(\omega_k)|^2 \quad (4.39b)$$

$X_{N_m}(\omega_k)$  may be found from Equation 4.10a. The choice of  $N$  and  $M$  for a given length of data is a compromise between reducing the variance by the approximate factor  $1/M$  and not reducing too much the resolving power which depends on the value of  $N$ . The periodogram estimated from Equation 4.38a is biased [56, 59]. But as  $N$ , the length of segment, increases the bias decreases [56, 59]. However, as the data length  $Q$  increases, both  $N$  and  $M$  can be allowed to increase, so that as  $Q$  approaches infinity, the bias and variance can approach zero.



#### 4.4.1 Welch method

In the Bartlett method, nonoverlapping rectangular windows were used for computing periodograms. Using different window shapes, Welch [60] showed that the standard deviation of each periodogram is still of the same order as its mean. The modified periodogram of each data segment is defined by

$$S_{N_m}(\omega_k) = \frac{1}{NU} |V_{N_m}(\omega_k)|^2 \quad (4.40)$$

where

$$V_N(\omega) = \sum_{n=0}^{N-1} v(n)e^{-j\omega n} \quad (4.41)$$

$v(n)$  can be found from Equation 4.29a, and  $U$  is the normalizing factor [57, 58]

$$U = \frac{1}{N} \sum_{n=0}^{N-1} [w(n)]^2 \quad (4.42)$$

Welch proposed overlapping of data segments which gives the smallest variance of the average modified periodogram per available length of data. Each segment can be represented by

$$x_m(n) = x(mL + n)w(n) \quad m = 1, 2, \dots, M \quad (4.43)$$

where  $L < N$ . Figure 4.5 shows the data segmentation for periodogram averaging when  $L = N/2$ . The first segments starts from data point 1 to data point  $2L$ . The second

segment starts from the middle of first segment, i. e.  $L+1$  to  $3L$ . This procedure continues up to the end of the complete length of the data. The total number of segments can be found by

$$M = \text{integer part of } [(Q-L)/L] \quad (4.44)$$

which is approximately twice the number of segments without overlapping when  $L=N/2$ . Welch showed that as these segments are not statistically independent, the variance is not reduced by a full factor of  $M$ , but by a factor of  $9M/11$  when  $L=N/2$  and this is the maximum reduction. Greater overlap does not continue to reduce the variance because the segments are less and less independent as the overlapping increase. Although  $9M/11$  is smaller than  $M$ , and since the number of segments is approximately twice as many for a given length of data, Welch method is more effective than Bartlett method.

Welch method can be summarized as follows: The modified periodogram of each data segment is calculated using Equations 4.40 through 4.42. The average modified periodogram is found by applying Equation 4.38a. Then, the variance of the estimate is given by

$$\text{var}\{\bar{S}_N(\omega_k)\} = \frac{9}{11M} \text{var}\{S_{N_m}(\omega_k)\} \quad (4.45)$$

#### 4.5 Conclusions

In this Chapter power spectral density (PSD) calculations using periodogram (i. e. square of the absolute of Fourier transform of the sensor signal) averaging is described. It was shown that the mean of periodograms of sensor signals converges to a power of the signal at that frequency. Variance of the periodograms at each frequency was shown to be equal to or greater than the power at that frequency. To reduce the variance of the

estimation of PSD, periodogram averaging using Bartlett method (using non overlapped data segment) and Welch method (overlapped data segments) were recommended.

Windowing data for the calculation of PSD was investigated. Problems associated with data windowing, namely, leakage, resolution for different window types were reviewed.

## CHAPTER V

### EXPERIMENTAL WORK AND DATA PROCESSING

In Chapter II it was pointed out that the cutting speed used by most researchers in drilling is higher (sometimes more than 1.5 times the cutting speed recommended in the Machining Data Hand Book [45]) than the normal cutting speed used in industry . The reason for this is if one were to use the recommended cutting speed (which is very conservative), the drill life would be of the order of thousands of holes which is not generally feasible in a laboratory environment. To overcome this, the following strategy is developed in this investigation. Data was collected at the recommended cutting speed and feed. However for accelerating wear, higher cutting speed ( $\sim$  twice the recommended speed) is applied periodically. Details of this strategy will be explained in Section 5.2.

In this investigation, the advantage of a very slow development of wear during normal cutting (using recommended speed and feed) was used. This gave adequate data over a number of holes with negligible wear development, which facilitated the use of a technique called averaging periodograms (discussed in Chapter IV) for the calculation of PSD. Good correlation is found between the change in the area under the PSD plots of sensor signals and the corner wear area of a drill bit.

#### 5.1 Experimental Setup

Figure 5.1 is the schematic of the experimental setup used in this investigation. A 3/8 in. diameter M2 high speed steel drill bit and a 8 in. long  $\times$  1 in. square section bar of AISI 1045 steel work material were chosen for the experiments. The depth of the holes was 0.45 in., cutting speed and feed were 50 ft/min and 0.005 in/rev respectively (selected

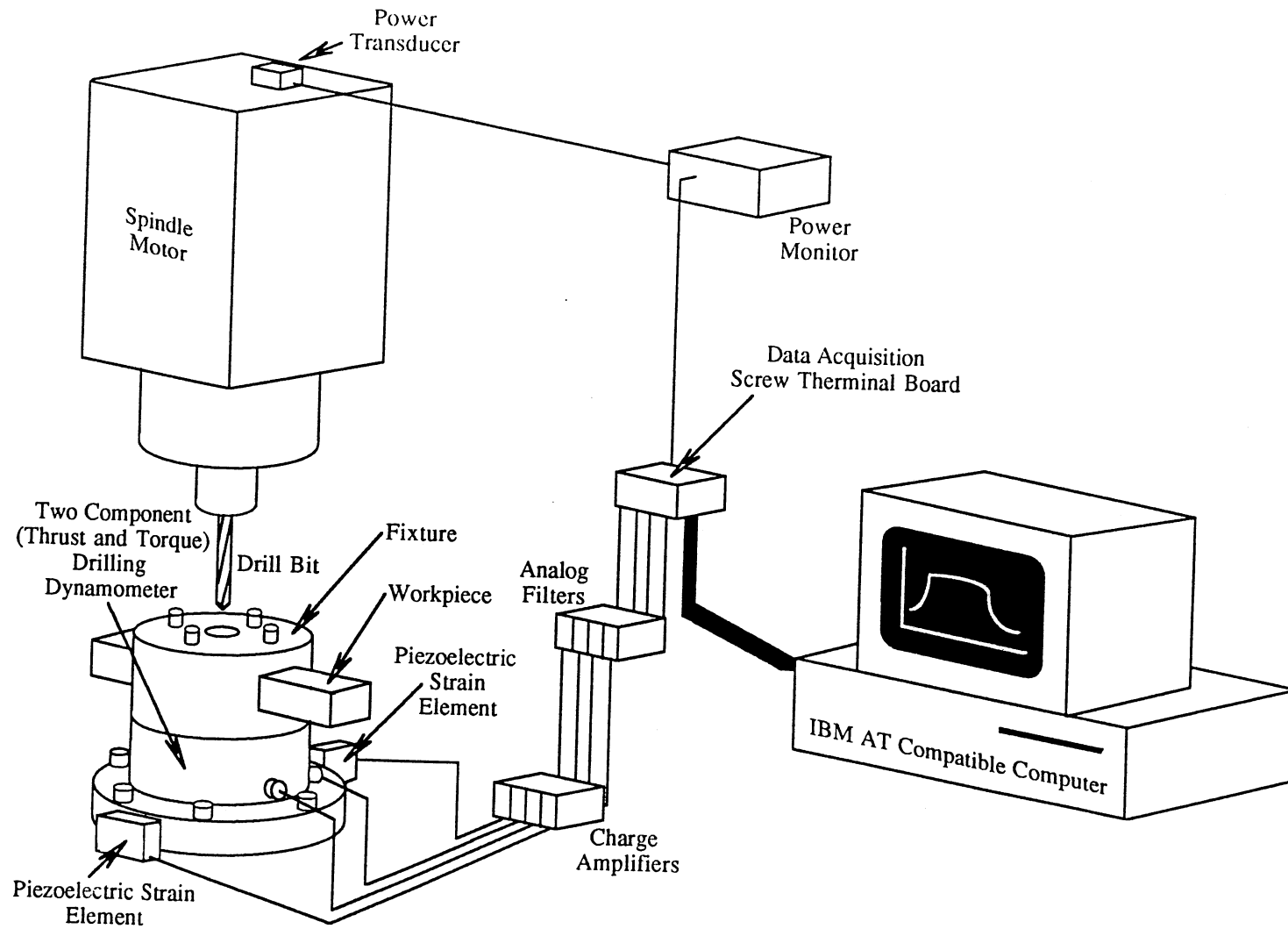
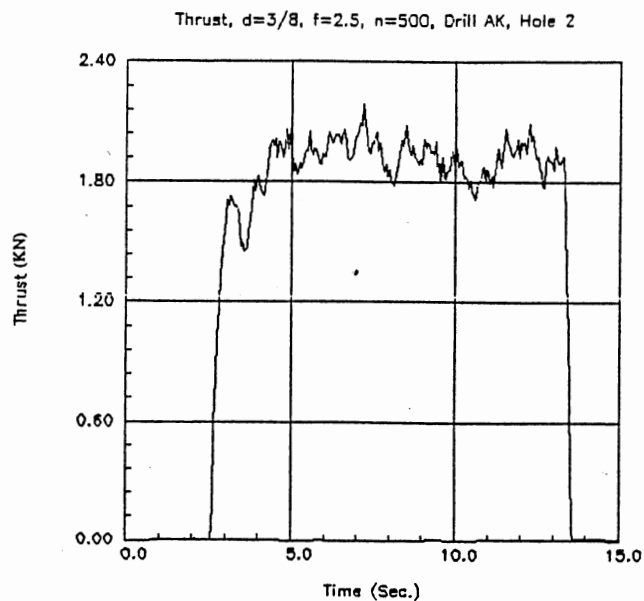


Figure 5.1 Experimental Drilling Setup

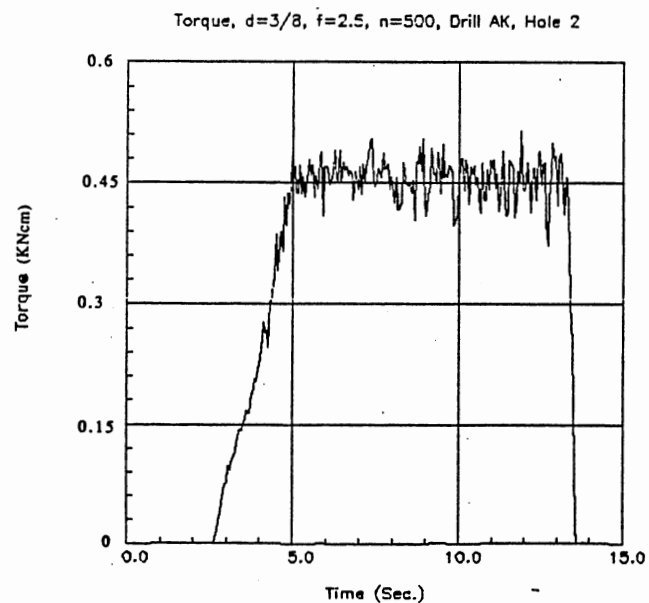
from the Machining Data Hand Book [45]). The hole depth was selected such that holes could be cut on both sides of a 1 in. square bar to conserve the use of work material. Experiments were carried out on a Bridgeport CNC milling machine. Appendix A gives the specification of the machine tool and the instrumentation used in this investigation. A fixture was made to hold the workpiece and the latter was mounted on a Kistler piezoelectric (Model 9271A) two-component dynamometer (thrust and torque). Two piezoelectric strain elements were used to measure strains in the X and Y directions and secured on the machine table. Workpiece was moved in the fixture after cutting each hole locate the put uncut part of the workpiece under the drill bit for cutting the next hole. The signals from the two component dynamometer and two piezoelectric strain elements were amplified by Kistler Charge Amplifiers and then passed through analog filters to avoid aliasing. The filters used are third order Butterworth active filters. The cut-off frequency and gain of the filters are adjusted by changing the appropriate resistors on the PC board of the filters. Signals were sampled by data acquisition board (Model Dash-16) on an IBM AT compatible computer. The signal from the power transducer after passing through the power monitor is also sampled by the data acquisition board. All sampled data were saved on the hard disk of the computer. Figures 5.2 show typical sensor signals of thrust, torque, strains in the X and Y directions at the recommended cutting speed and feed for a 3/8 in. drill bit. Sampling of the sensors signals for each hole commenced at a known depth (0.17 in.) where the conical portion of the drill is completely inside the workpiece. The minimum depth is calculated as

$$\begin{aligned} \text{Required depth} &= (\text{Drill diameter}) \cot(\text{Point angle}/2)/2 \\ &= (3/8) \cot(59^\circ)/2 = 0.12 \text{ in.} \end{aligned}$$

To compensate for the possible geometrical errors of the drill bits, sampling commenced at 0.17 in depth of each hole instead of the required depth of 0.12 in. To initiate the sampling

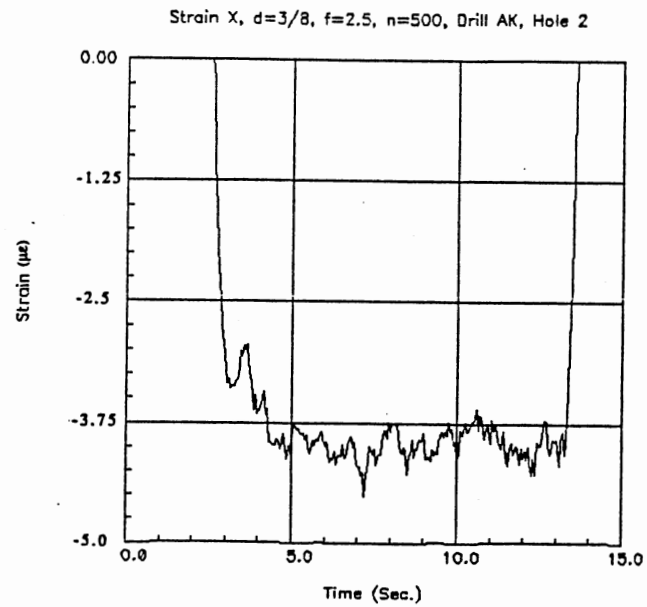


(I) Thrust

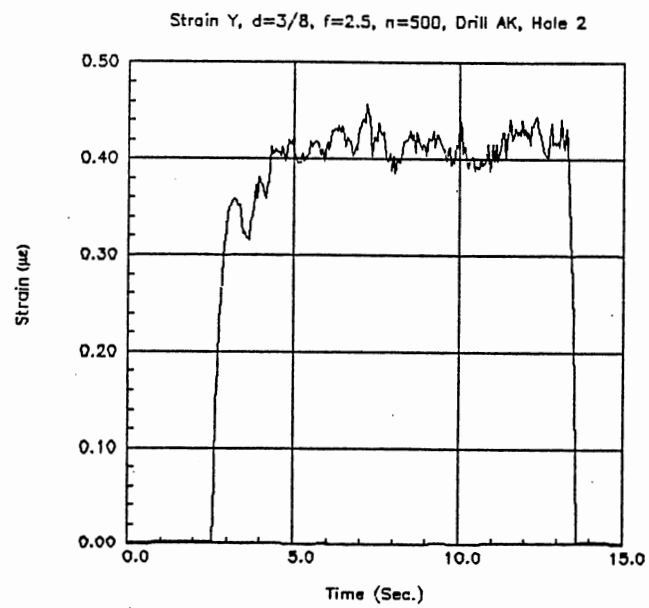


(II) Torque

Figure 5.2 Sensor Signals From the Beginning to the end of Cutting Hole No. 2 of Drill AK. (I) Thrust, (II) Torque. Cutting Speed = 50 ft/min, feed rate = 0.005 in/rev drill diameter 3/8 in. Work material AISI 1045 Steel.



(III) Strain in the X Direction



(IV) Strain in the Y Direction.

Figure 5.2 (Continued) (III) Strain in the X direction (IV) Strain in the Y direction.



sensor signal at this depth, the following method was used: As can be seen from Figure 5.2, the thrust signal has a very steep slope (approximately  $90^\circ$ ) when the drill bit enters the work material. The computer samples the thrust signal until the thrust force passes 800 N, it then waits for 4.08 sec., required for the drill bit to penetrate 0.17 in. inside the workpiece at the selected cutting speed and feed. At the end of this period the computer starts sampling all sensor signals at the same time. The signals are sampled at 5 KHz for 0.74 second. The corner frequency of analog filters is set to 2500 Hz. It will be shown in Section 5.2, estimates of power at frequencies below 300 Hz have maximum signal-to-noise ratio, therefore, they have been considered in this research. As power at frequencies above 300 Hz are not required, sampling rate is reduced to 1 KHz for 0.9 second and the corner frequency of analog filters is set to 450 Hz..

In this research, data are collected from 6500 holes and 156000 FFT calculation are performed as well as 3500 plots have been produced. Author developed, the necessary computer codes for performing calculations and plotting the graphs. In this report, the results of data from 1500 holes are presented, which involved 36000 FFT calculations.

#### 5.1.1 Block diagram of the experimental setup

Figure 5.3 is a modified block diagram of Koren [4] of the experimental setup. There are two feedback loops. The first feedback returns with the actual cutting speed (for example through a tachometer or an encoder). A comparator compares the reference cutting speed and the feedback signal, then proper control command is sent to the spindle drive of a machine tool to adjust the cutting speed by the controller. However, the torque required to maintain the cutting at the reference cutting speed reduces the cutting speed. Therefore, actual cutting speed is different from the reference cutting speed. Similarly, the second feedback system controls the feed mechanism.

As shown in Figure 5.3 drilling process is a two input-cutting speed and feed and two output-torque and thrust system. Each input has an effect on both outputs. For

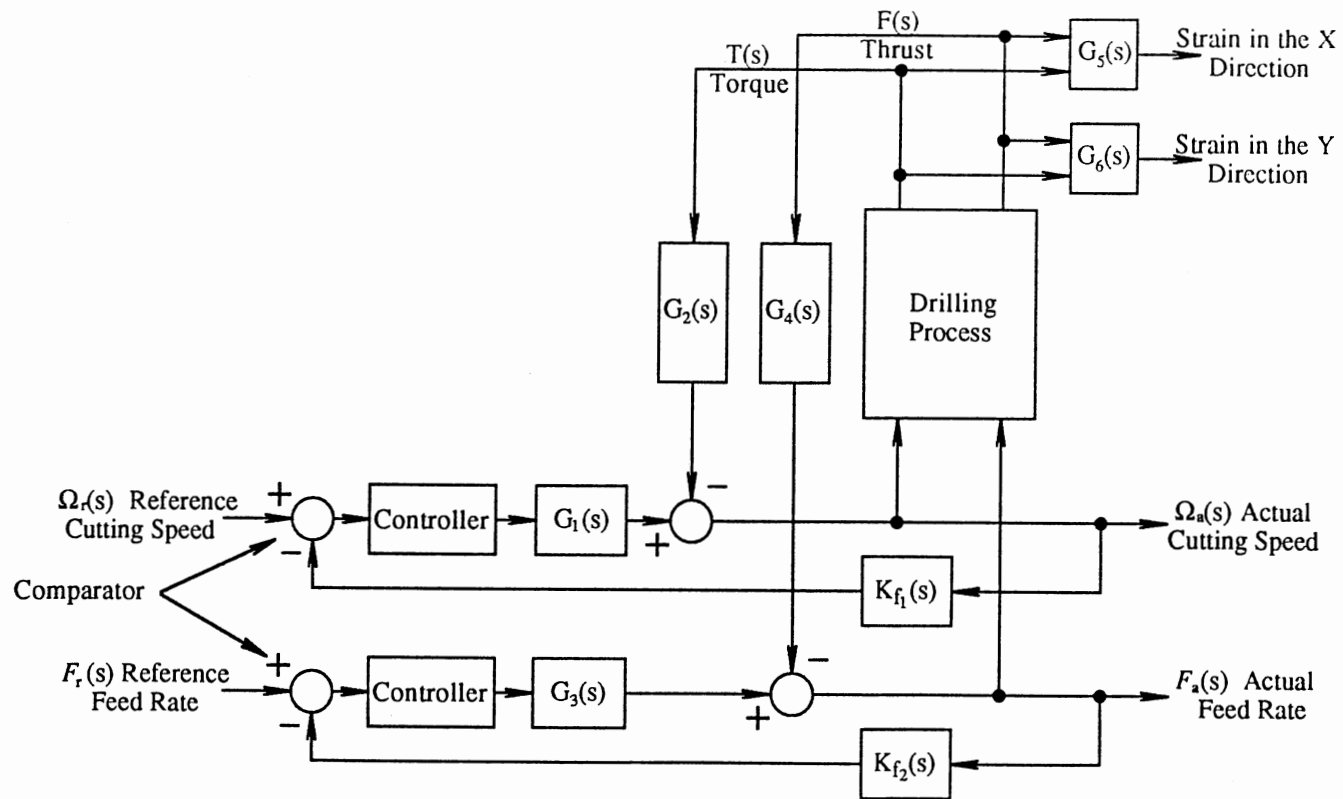


Figure 5.3 Block Diagram of the Experimental Setup

example, an increase in the feed causes an increase in both the torque and the thrust force. Strains on the machine table along the cutting direction and perpendicular to the drill axis can be correlated with torque and thrust by an appropriate transfer functions. In this investigation, torque, thrust, strain in cutting direction (X-direction), and strain perpendicular to the drill axis (Y-direction) on the machine table are measured and are correlated with drill wear.

## 5.2 Experiment Strategy

Each drill is defined by two capital letters, for example drill AD or drill BF. In the first stage of the experiments a 3/8 in. drill bit (drill AC) was used to cut 0.45 in. deep holes in AISI 4150 steel (330 BHN) using the recommended cutting speed (50 ft/min) and feed rate (0.004 in/rev) from the Machining Data Hand Book [45]. It was observed that after cutting 610 holes, the drill bit was still sharp. Therefore, it was decided to accelerate wear on the drill bit by using higher cutting speed on the same work material. The cutting speed was thus increased to twice the recommended speed (100 ft/min) and the feed rate was increased to 0.005 in/rev. The hole depth was same as in the previous case, i. e. 0.45 in. As a result, the drill life was reduced to 16-40 holes (drill AF, AG and AH) for this case. The following rough calculation was made to calculate the drill life using the Taylor tool life formula at the recommended cutting speed. The  $n$  value in the Taylor's Tool life formula for the drilling process was estimated by Kadlor et al [21] to be 0.14. Therefore, the Taylor tool life formula for the present case can be represented as

$$VT^{0.14} = C$$

If each hole takes about  $T_h$  cutting time, then the total cutting time is  $T = NT_h$ , and the above equation will be modified to

$$VN^{0.14} = C_1$$

where  $C_1 = CT_h^{-0.14}$ . From the above equation we can write

$$V_1/V_2 = (N_2/N_1)^{0.14}$$

It was found that the drill life at the cutting speed of 100 ft/min is 16 to 40 holes. Assuming the average drill life to be 30 holes at this cutting speed and using the above equation, the drill life for the drill bit at 50 ft/min is 4240 holes. This is a conservative estimate, because thermal softening reduces tool life drastically at the high cutting speed and 30 holes may not be the exact value for drill life to substitute in the Taylor tool life formula. It was, therefore, concluded that it could take thousands of holes for one drill bit to completely wear if the recommended cutting speeds and feeds were used. Based on the above discussion the following experimental strategy was developed (Figure 5.4). High cutting speed was used to accelerate drill wear. After the drill had reached a certain state of wear the recommended cutting speed and feed were used. During this stage, designated as normal cutting, progress of wear on the drill bit was found negligible. All of the sensor signals (thrust, torque, strain in the X and Y directions) were sampled at the same time during this stage. Now, it was assumed that wear does not change during this stage and therefore all signals over these holes are associated with the same state of drill wear. In order to go to the next stage of wear, cutting speed was increased again to the higher speed (i. e. 100 ft/min). This procedure was repeated several times.

Figures 5.4, 5.5a, and 5.5b show this procedure for drill BL. As can be seen from Figure 5.4, high cutting speed (100 ft/min) is used for holes 1 to 10, 111 to 120 and 221 to 230 (steep slopes). During high speed cutting no signal was sampled and the work material used was AISI 4150 (330 BHN). Normal cutting conditions were used for holes 11 to 110, 121 to 220 and 231 to 330 and the work material was AISI 1045 steel (230 BHN).

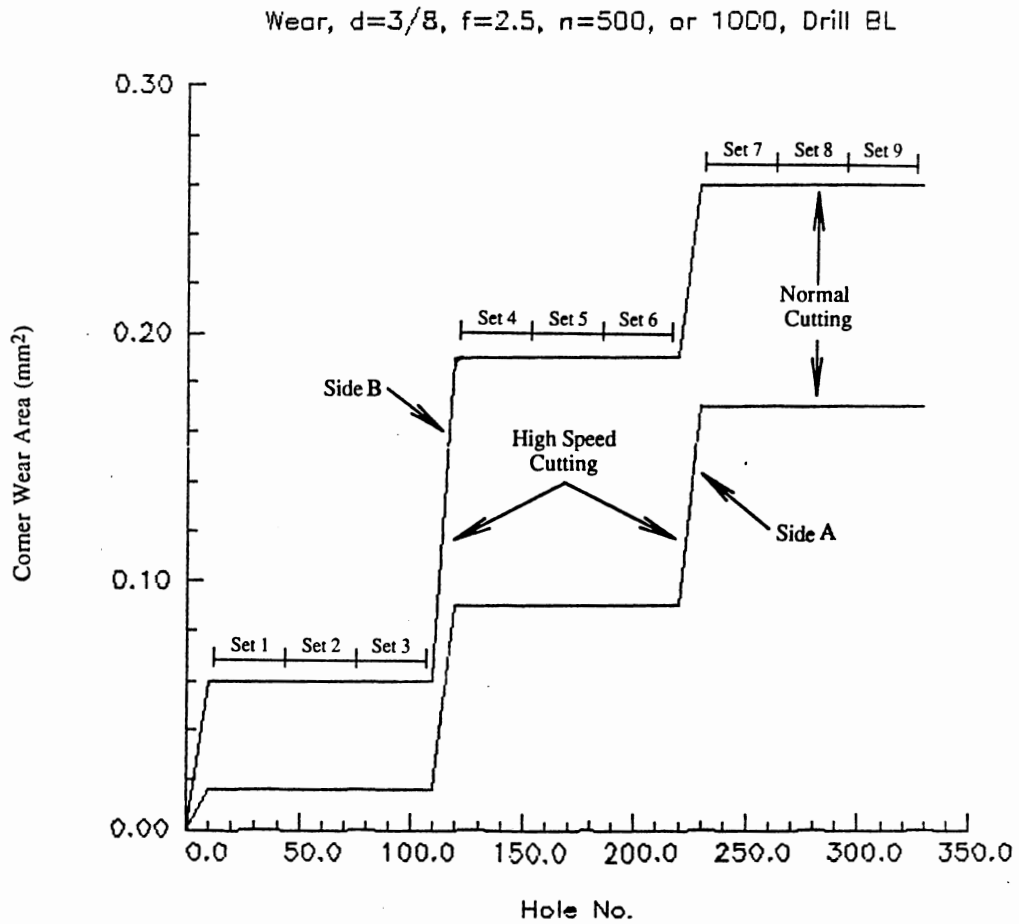


Figure 5.4 Plot of Wear vs. the Hole No. for Drill BL. Drill bit 3/8 in. For Normal Cutting: Cutting Speed: 50 ft/min (Spindle Speed: 500 rpm), Feed: 0.005 in/rev (2.5 in/min), Work Material AISI 1045 Steel (230 BHN). For High Speed Cutting: Cutting Speed: 100 ft/min (Spindle Speed: 1000 rpm), Feed rate: 0.005 in./rev (5 in./min). Work Material AISI 4150 Steel (330 BHN).

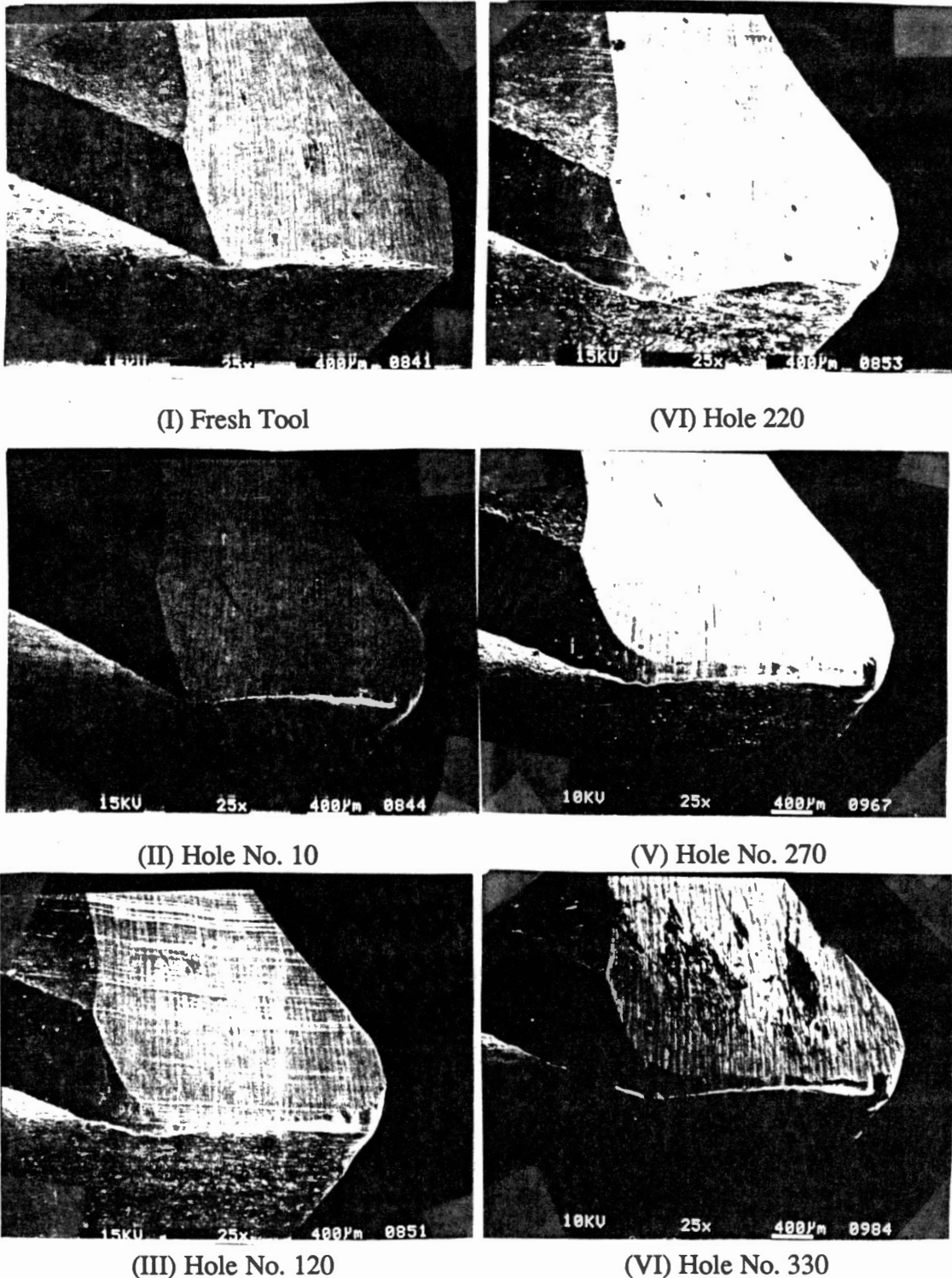


Figure 5.5a SEM Photograph at Different Stage of Wear for Side A of Drill BL. (I) Side A of Fresh Drill, (II) Side A, After Cutting 10 Holes, (III) After Cutting 120 holes, (IV) After Cutting 220 Holes, (V) After Cutting 270 Holes, (VI) After cutting 330 Holes. Drill bit 3/8 in., For normal cutting: Cutting speed: 50 ft/min (spindle speed: 500 rpm), Feed: 0.005 in./rev (2.5 in./min), Work material AISI 1045 steel (230 BHN). for high speed cutting: Cutting speed: 100 ft/min (spindle speed: 1000 rpm), Feed: 0.005 in./rev (5 in./min). Work material AISI 4150 steel (330 BHN).

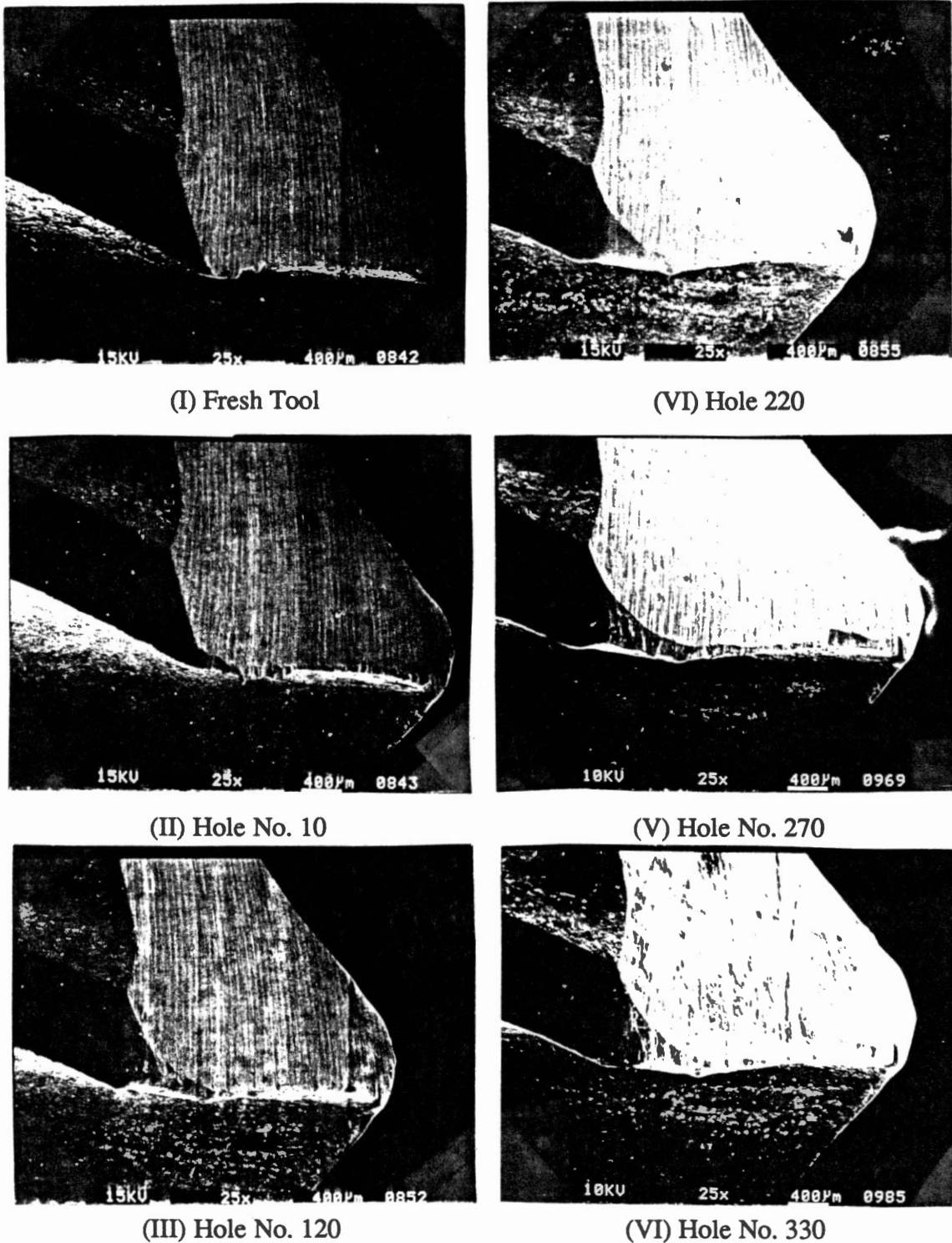


Figure 5.5b SEM Photograph at Different Stage of Wear for Side B of Drill BL. (I) Side B of Fresh Drill, (II) Side B, After Cutting 10 Holes, (III) After Cutting 120 holes. (IV) After Cutting 220 Holes, (V) After Cutting 270 Holes, (VI) After cutting 330 Holes. Drill bit 3/8 in., For normal cutting: Cutting speed: 50 ft/min (spindle speed: 500 rpm), Feed: 0.005 in./rev (2.5 in./min), Work material AISI 1045 steel (230 BHN). for high speed cutting: Cutting speed: 100 ft/min (spindle speed: 1000 rpm), Feed: 0.005 in./rev (5 in./min). Work material AISI 4150 steel (330 BHN).

On comparing the scanning electron microscope (SEM) photographs (Figures 5.5a and 5.5b) of side A and side B of drill BL at hole No. 120 (which is at the end of high speed cutting) and hole No. 220 (which is at the end of normal cutting) are compared only minor changes of wear can be observed in drilling 100 holes during normal cutting. The same conclusion can be drawn by comparing SEM photographs of the same drill at holes 270 and 330.

Figure 5.4 shows one side of the drill is worn more than the other side. This uneven wear on different sides of the drill was also noticed by Braun et al [32] also. This might be due to geometrical errors in the manufacture of the drill bit as well as uneven hardness variation of the drills. Uneven hardness of drill bit, i. e. one side of the drill bits harder than the other can result from the problems associated with heat treatments of an intricate shaped drill bit.

One observation can be made in the high cutting speed region. Although Figure 5.4 shows that 10 holes were cut in the high cutting speed period, for example holes 111 to 120, the exact number of holes was not shown in the figure. This is because, in high speed cutting, drill life can vary between 16 and 40 holes. Therefore, the following procedure was adapted during this period. After drilling a few holes, the drill bit was observed under an optical microscope for drill wear. If change of drill wear was sufficient then normal cutting was resumed. Otherwise the former procedure was repeated again. For simplicity and paying attention to the fact that no signal was sampled during high cutting speed period, this region was shown in Figure 5.4 only as 10 holes.

### 5.3 Vibration Analysis of the Experimental Setup

Before analyzing data in the frequency domain, it is necessary to examine some of the critical natural frequencies of the system. Documented data regarding natural frequency of the machine tool was not available from the machine tool builder. Rotberg et al [61] conducted vibration analysis of a drill bit using finite element method (FEM). They found



the torsional and axial natural frequency of a 100 mm long, 10 mm diameter drill bit (approximately similar to a 3/8 in. drill bit used in this investigation) to be 5 KHz and 14 KHz respectively.

Torsional vibration of the dynamometer, including the fixture and the workpiece, may be calculated as follows: From Kistler Model 9271A users manual, natural frequency and torsional rigidity of dynamometer are given as  $f_d = 3$  KHz and  $K_d = 50$  Ncm/ $\mu$ rad respectively.  $I_d$ , the moment of inertia of the dynamometer is

$$I_d = \frac{K_d}{(2\pi f_d)^2} = \frac{50 \times 10^8 \text{ kg cm}^2/\text{rad}}{(2\pi \times 3000)^2} = 14.1 \text{ kg cm}^2$$

Moment of inertia of a 8 in. long  $\times$  1 in. square bar in extreme position is

$$I_w = \frac{Ah^3\rho}{3} = \frac{(2.54)^2(8 \times 2.54)^3(0.0078)}{3} = 134.1 \text{ kg cm}^2$$

Body of the fixture, made of aluminum, has a cylindrical shape with 9 cm diameter and 5.5 cm height. The cover of the fixture which is made of steel has a cylindrical shape also of the same diameter and with a 1 cm height. Therefore, the moment of inertia of the fixture is

$$I_f = \frac{\pi D^4 h_1 \rho_1}{32} + \frac{\pi D^4 h_2 \rho_2}{32} = \frac{\pi 9^4 \times 5.5 \times 0.0027}{32} + \frac{\pi \times 9^4 \times 1 \times 0.0078}{32}$$

$$= 14.6 \text{ kg cm}^2$$

The total moment of inertia is

$$I_t = I_d + I_w + I_f = 134.9 + 14.1 + 14.6 = 163.5 \text{ kg cm}^2$$

and

$$f_n = \frac{1}{2\pi} \sqrt{\frac{K_d}{I_t}} = \frac{1}{2\pi} \sqrt{\frac{50 \times 10^8}{163.5}} = 880 \text{ Hz}$$

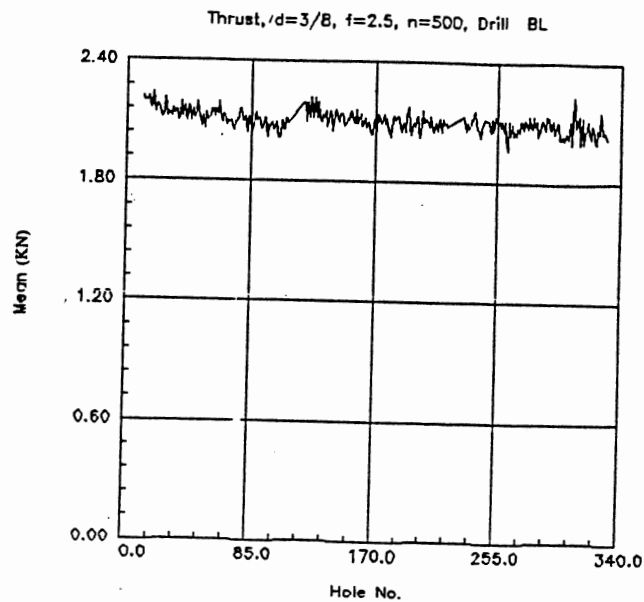
The moment of inertia of the workpiece is maximum at a location when the hole is at the end of the workpiece. However, in drilling most part of the workpiece the moment of inertia will be less than the calculated value in the extreme position. Consequently the natural frequency of the dynamometer including the fixture and the workpiece will be higher than 880 Hz.

#### 5.4 Analysis of the Sensor Signals in the Time Domain

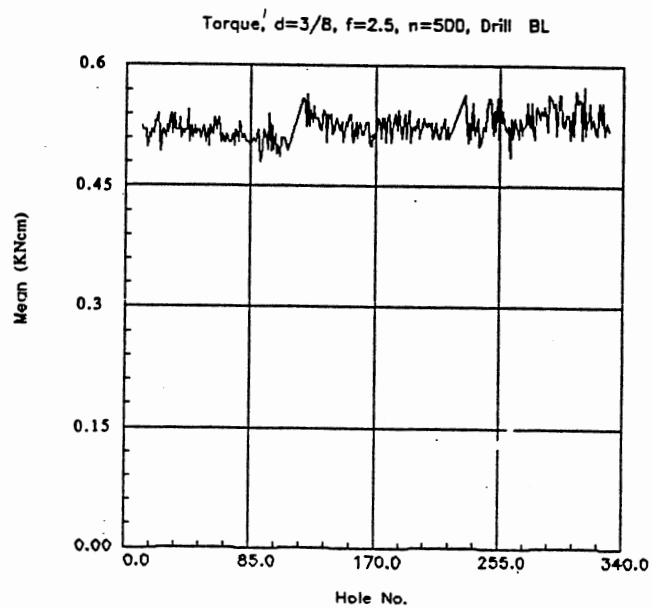
In the time domain, the mean and the variance of the sensor signals for each hole were calculated and plotted against the hole number. Figures 5.6 and 5.7 show these results. From Figure 5.4, it may be noted that the total corner wear for hole number 50 and hole number 250 are 0.076 mm<sup>2</sup> and 0.43 mm<sup>2</sup> respectively (see Section 5.6 for details of the calculation of the total corner wear area). But from Figures 5.6 and 5.7 no significant differences can be found in the mean and the variance of sensor signals for these two holes. Therefore, it can be concluded that sensor signals in the time domain do not show any correlation with drill wear.

#### 5.5 Analysis of the Sensor Signals in the Frequency Domain

If the mean of a sensor signal is not subtracted from the total signal, its power spectrum will show a high value at zero frequency. If the mean is relatively large with respect to the variance of the signal (as can be seen from Figures 5.2, 5.6 and 5.7, of this investigation), this component will dominate the spectrum estimate causing low amplitude, low frequency component to be obscured by leakage [57]. Therefore, in this investigation, mean of each data segment is estimated and the resulting estimate is subtracted from the sensor signal before computing the power spectrum estimate. It should be noted that the

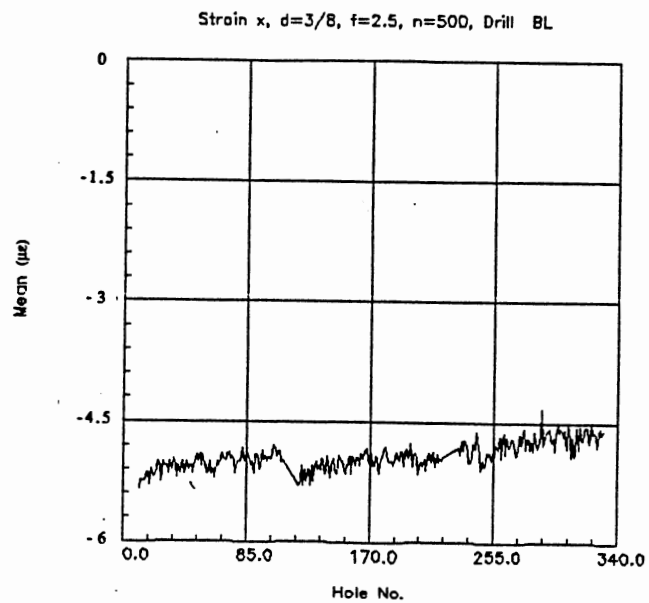


(I) Thrust

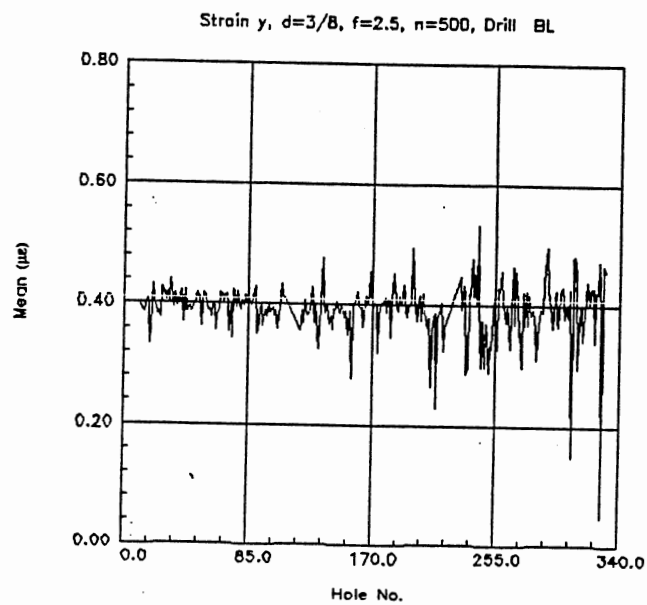


(II) Torque

Figure 5.6 Mean of Sensor Signals in the Time Domain for Drill BL. (I) Thrust, (II) Torque. For 3/8 in. Drill bit, Cutting Speed = 50 ft/min (500 rpm Spindle Speed), Feed Rate = 0.005 in/rev (2.5 in./min), Work Material AISI 1045 Steel (230 BHN).

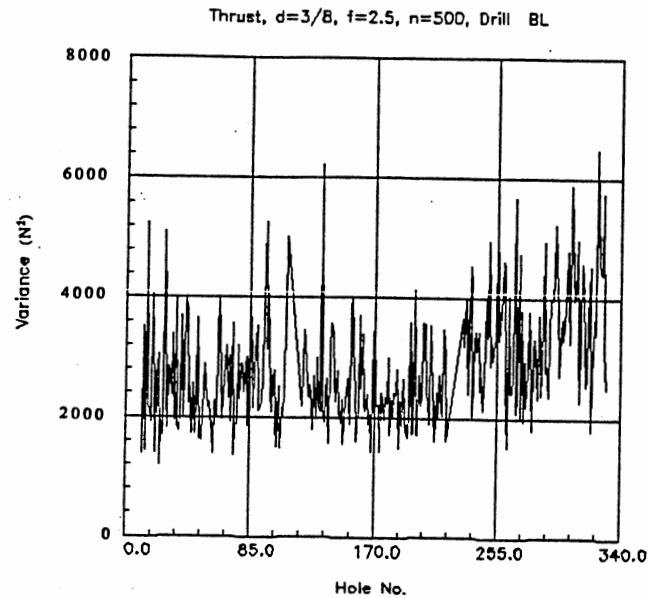


(III) Strain in the X Direction

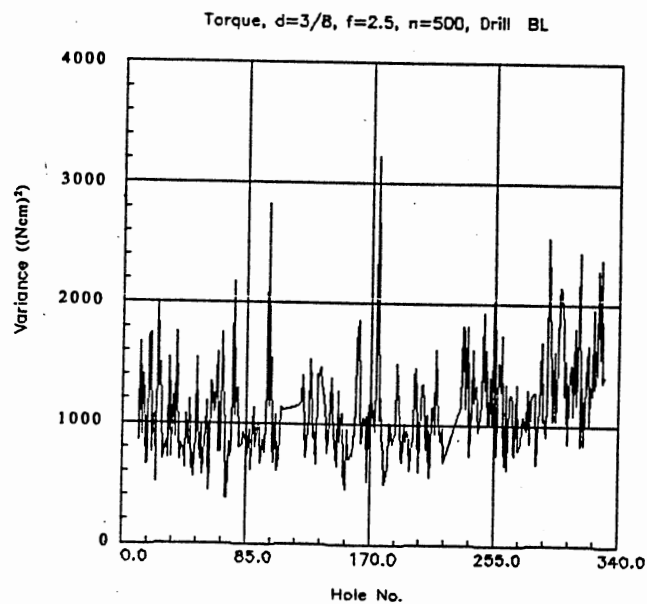


(IV) Strain in the Y Direction.

Figure 5.6 (Continued) (III) Strain in the X direction (IV) Strain in the Y direction.

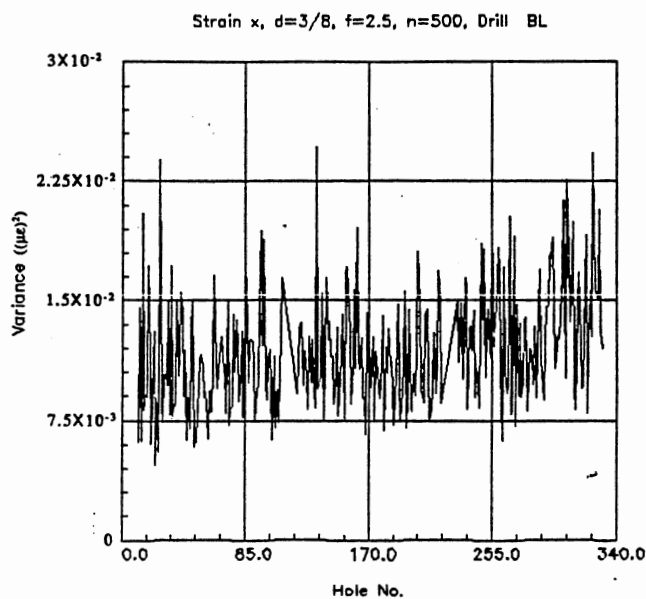


(I) Thrust

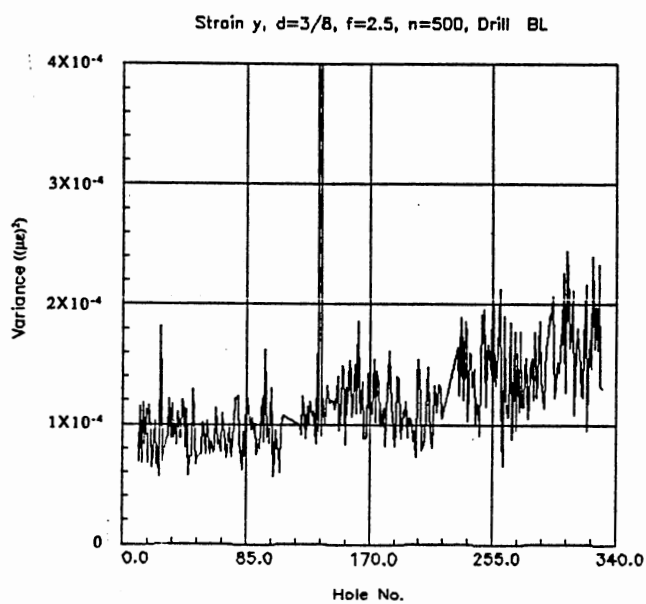


(II) Torque

Figure 5.7 Variance of Sensor Signals in the Time Domain for Drill BL. (I) Thrust, (II) Torque. For 3/8 in. drill bit, Cutting speed = 50 ft/min (500 rpm spindle speed), Feed rate = 0.005 in/rev (2.5 in./min), Work material AISI 1045 Steel (230 BHN).



(III) Strain in the X Direction



(IV) Strain in the Y Direction.

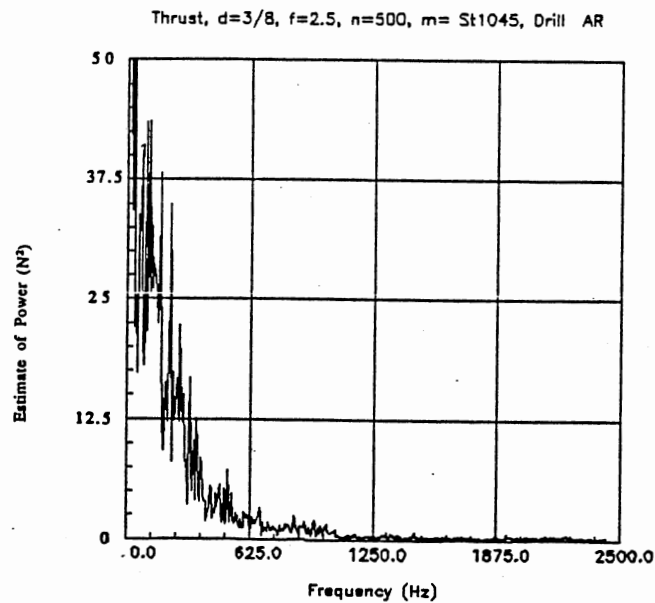
Figure 5.7 (Continued) (III) Strain in the X direction (IV) Strain in the Y direction.

mean of each data segment is only a rough estimate of the zero frequency component. Hence, some peak should be expected at zero frequency. However, the subtraction of the approximate mean from the total sensor signal leads to a better estimate at neighboring frequencies [57].

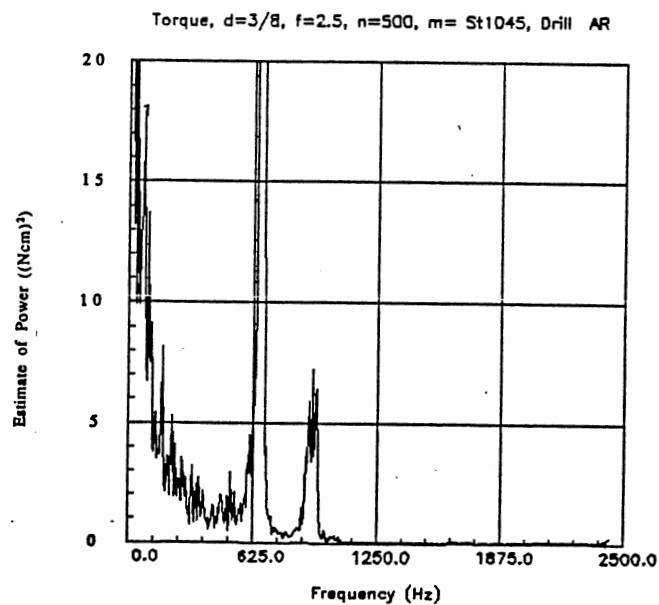
As mentioned earlier, no noticeable change was observed in drill wear over a number of holes in normal cutting (Figure 5.4). On the other hand, the sources of noises, such as nonuniformity in hardness of the work material, built-up edge, and microcracks should have some probability distribution functions that do not change at the same state of drill wear and cutting conditions. Therefore, it is assumed that the process is a stationary random process over a number of holes with negligible wear development. Consequently, the estimate of PSD can be found by averaging the periodograms of data segments from the holes with negligible wear development (as shown in Chapter IV for stationary random process).

At the beginning of the experimental work, relatively high sampling rate was used, i. e. 5 KHz for 0.74 sec. The corner frequency of the analog filters was set to 2500 Hz. The objective was to find the minimum sampling rate that gives the most information on the cutting process. For the calculation of FFT, 1024 data points were used which gives 4.88 Hz frequency resolution. Figure 5.8 shows the estimate of the PSD of the sensor signals for Hole No. 200 of drill AR. For estimating the PSD shown in Figure 5.8, Welch method (see Chapter IV) was used to average six data segments with a 50% overlap from each hole. Hanning window was applied to each data segment.

The reasons for the selection of the Hanning window for the calculation of the estimate PSD, among the windows shown in Figure 4.4, are as follows: Rectangular window has higher relative amplitude of the mainlobe and sidelobe and hence results in higher leakage. The reason for not considering the Blackman window is lower resolution due to wide mainlobe. Among the other windows discussed in Chapter IV, namely, Bartlett, Hanning, and Hamming, Hanning was considered as it has lower relative



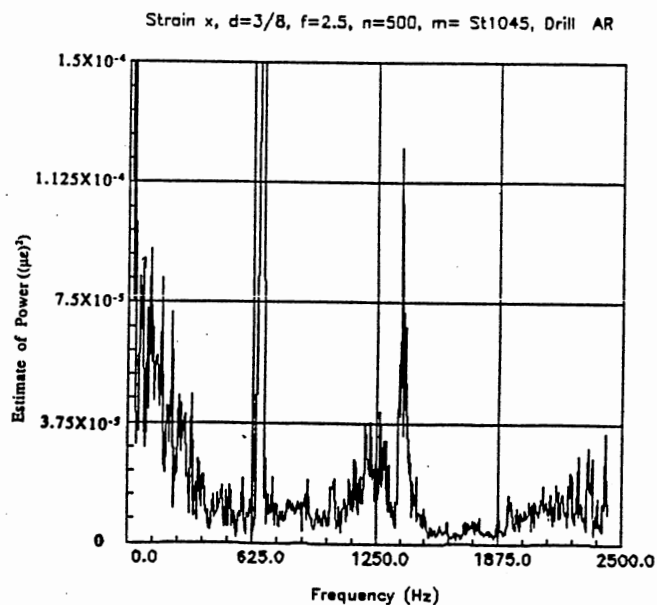
(I) Thrust



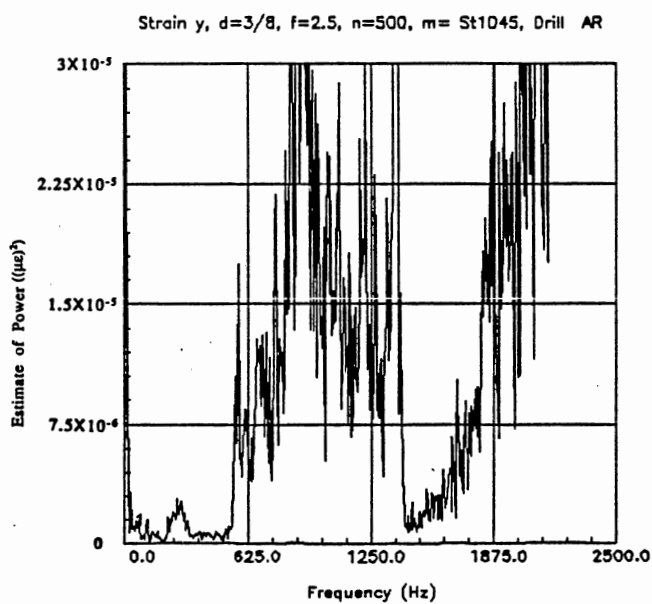
(II) Torque

Figure 5.8 Estimate of PSD of Sensor Signals of Hole No. 200 for Dill AR. (I) Thrust, (II) Torque. For 3/8 in. drill bit, Cutting speed = 50 ft/min (500 rpm spindle speed), Feed rate = 0.005 in/rev (2.5 in./min), Work material AISI 1045 Steel (230 BHN).





(III) Strain in the X Direction



(IV) Strain in the Y Direction.

Figure 5.8 (Continued) (III) Strain in the X direction (IV) Strain in the Y direction.

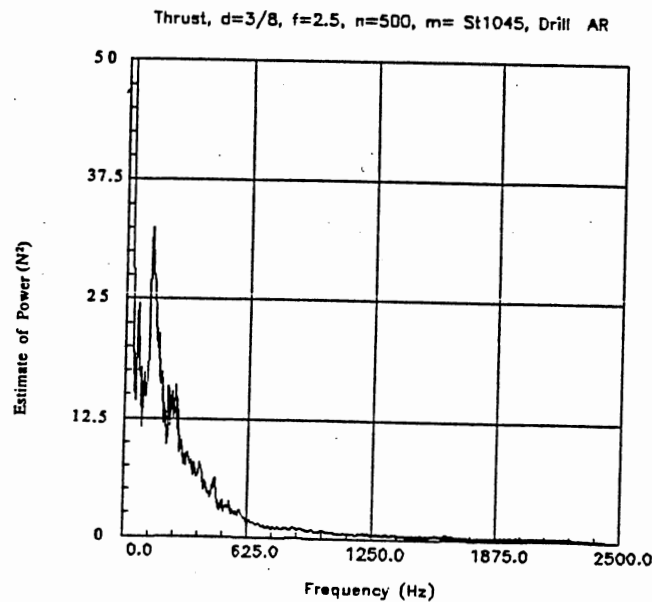
amplitude mainlobe and sidelobes and hence less leakage, even though all of them have the same mainlobe width.

Each estimate of the PSD plot in Figure 5.8 is an average of the modified periodograms of 6 data segment with a 50% overlap. As can be seen, the estimate of PSD of the sensor signals are rather noisy. Therefore, six data segments are insufficient to reduce the variance of the periodogram. To overcome this problem, the number of data segments should be increased which is impractical due to insufficient RAM space during data acquisition. As all the data has to be saved in the RAM during data acquisition due to high sampling rate; this would demand considerable RAM space. The data can not be transferred to the hard disk during data acquisition at the high sampling rate. Increasing the duration of the data collection means drilling deeper holes, this is not advisable due to the possibility of chip entanglement which affects the sensor signals. Therefore, it was decided to average the periodograms of the data segments of the sensor signals over a number of holes over which change of drill wear was negligible. The variance of the noises were reduced significantly. Figure 5.9 shows the results of the periodograms of data segments of sensor signals over 40 holes for drill AR (in this case each plot is the average modified periodograms of 240 data segments, i. e. 6 from each hole  $\times$  40 holes). At the same time signal-to-noise ratios for all sensors were calculated using the following equation:

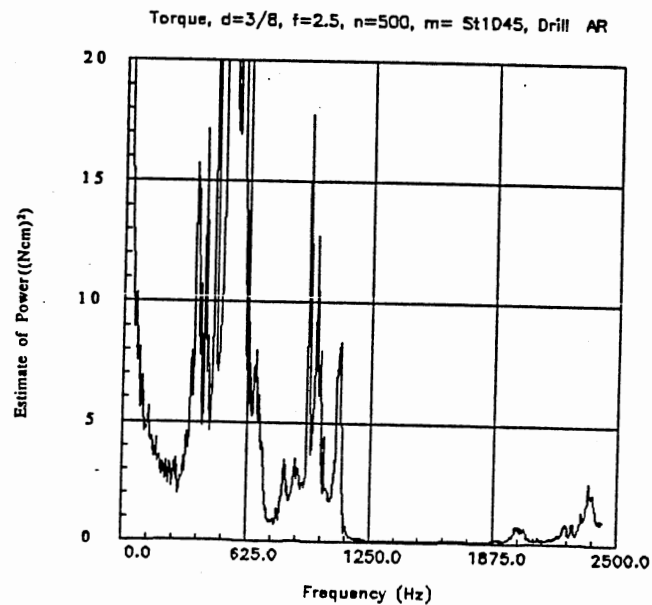
$$STN(\omega_k) = \frac{\bar{S}_T(\omega_k)}{\sqrt{\text{var}(S_T(\omega_k))}} \quad (5.1)$$

This equation has been adopted from a similar equation in the time domain [56] the results of which are shown in Figure 5.10.

As can be seen in Figures 5.9, the torque signal shows high peaks at frequencies above 300 Hz. The signal-to-noise ratio of the torque signal as in Figure 5.10 is very low

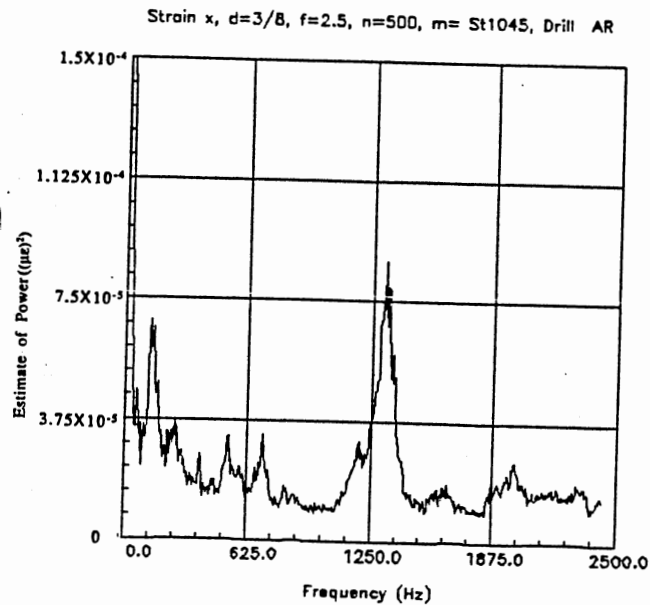


(I) Thrust

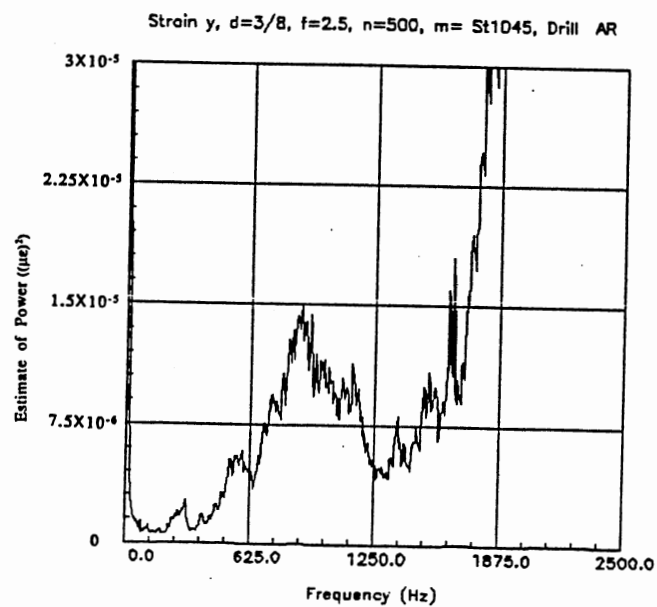


(II) Torque

Figure 5.9 Estimate of PSD of Sensor Signals Over 40 Holes (From Hole No. 200 to Hole No. 239) for Drill AR. (I) Thrust, (II) Torque. For 3/8 in. drill bit, Cutting speed = 50 ft/min (500 rpm spindle speed), Feed rate = 0.005 in/rev (2.5 in./min), Work material AISI 1045 Steel (230 BHN).

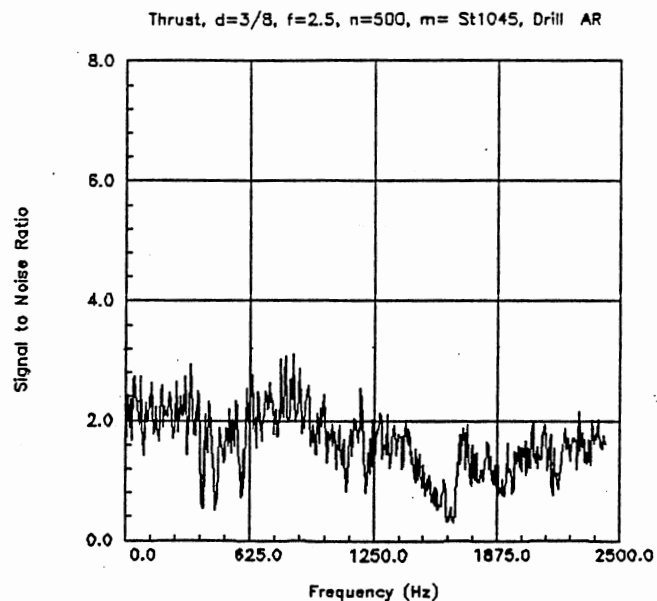


(III) Strain in the X Direction

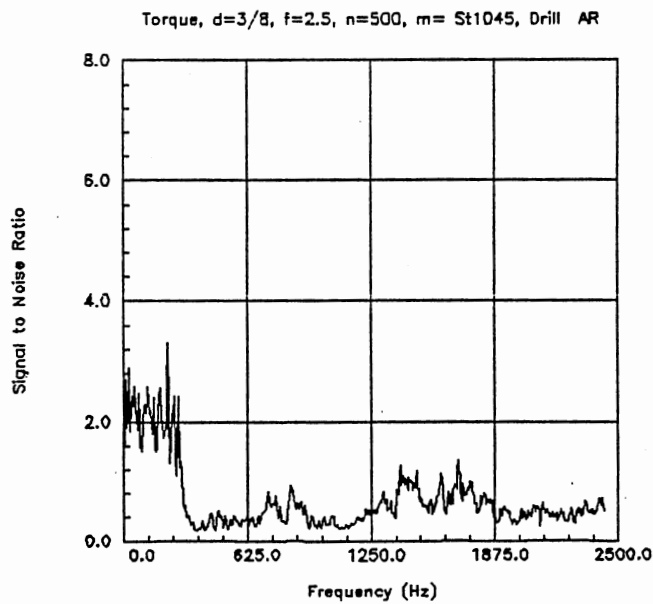


(IV) Strain in the Y Direction.

Figure 5.9 (Continued) (III) Strain in the X direction (IV) Strain in the Y direction.

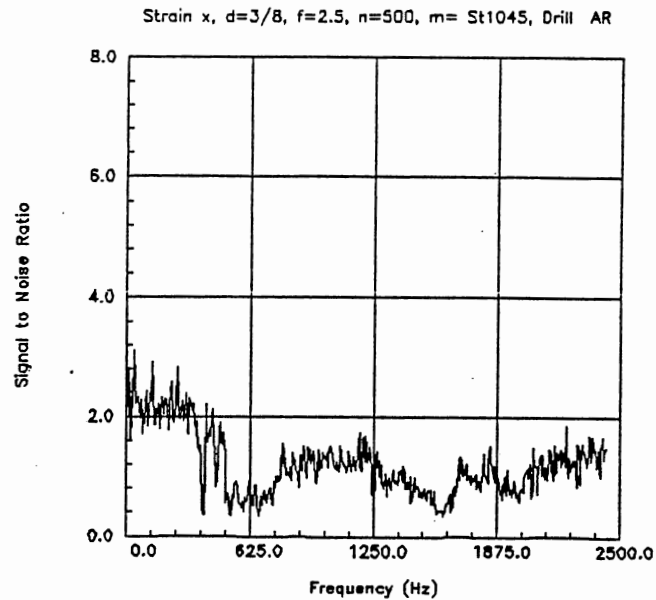


(I) Thrust

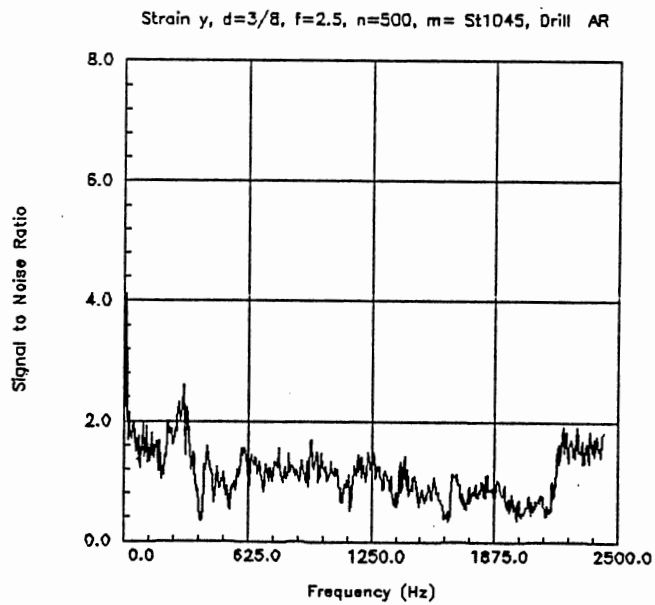


(II) Torque

Figure 5.10 Signal-to-Noise Ratio of Sensor Signals in the Frequency Domain Over 40 Holes (From Hole No. 200 to Hole No. 239) for Drill AR. (I) Thrust, (II) Torque. For 3/8 in. drill bit, Cutting speed = 50 ft/min (500 rpm spindle speed), Feed rate = 0.005 in/rev (2.5 in./min), Work material AISI 1045 Steel (230 BHN).



(III) Strain in the X Direction



(IV) Strain in the Y Direction.

Figure 5.10 (Continued) (III) Strain in the X direction (IV) Strain in the Y direction.

at frequencies larger than 300 Hz. Vibration analysis in Section 5.3 indicates that torsional vibration of the dynamometer (including the workpiece) should be higher than 880 Hz. High peaks at these lower frequencies (lower than 880 Hz) might be associated with the vibration of a system consisting of the large mass of spindle drive connected to a drill bit with low torsional rigidity. Figure 5.3 shows that strains in the X- and Y-directions are related to the torque signal by a transfer function. As can be seen in Figure 5.10, the signal-to-noise ratio of the strains in the X and Y directions is lower for frequencies above 300 Hz.

Frequencies with the least noise contamination are the most reliable frequencies. Frequencies with maximum signal-to-noise ratio are the most desirable and are selected. As can be seen from Figures 5.10, maximum signal-to-noise ratio is obtained for all sensor signals up to 300 Hz. Therefore, sampling rate was reduced to 1 KHz for 0.9 sec., and corner frequency of analog filters was set to 450 Hz. For the calculation of FFT, 256 data points were used which gave 3.91 Hz frequency resolution and Hanning window again was used for the data windowing. This enabled smaller data files on the hard disk at the same time decreased the calculation time.

It is interesting to compare the experimental results with theory. As can be seen from Figures 5.10, the signal-to-noise ratio up to 300 Hz for all sensors is ~2.2. According to Equations 4.28, 4.45 and 5.1, the ratio for averaging six periodograms should be

$$\sqrt{\frac{9M}{11}} = \sqrt{\frac{9 \times 6}{11}} \leq 2.2$$

Which is the same as the values from signal-to-noise ratio of the plots. As mentioned in Chapter IV, the variance of the periodogram of each data segment of a signal is of the same order of magnitude as the power of the signal at that frequency. Therefore,

averaging the periodograms of 6 data segments reduces the standard deviation by an order of 2.2. The problem associated with signal-to-noise ratios at different states of drill wear will be addressed in Section 6.2.

In order to check repeatability, i. e. to investigate if there is any change in the PSD of the signals at the same state of drill wear, three independent sets of holes at each state of drill wear were selected as follows (see Figure 5.4 for details of the selection of sets of holes and Section 5.6 for details of the calculation of total corner wear area)

1) Total corner wear  $0.076 \text{ mm}^2$

Set 1: hole no 11 to 40

Set 2: hole no 41 to 80

Set 3: hole no 81 to 110

2) Total corner wear  $0.28 \text{ mm}^2$

Set 4: hole no 121 to 150

Set 5: hole no 151 to 190

Set 6: hole no 191 to 220

3) Total corner wear  $0.43 \text{ mm}^2$

Set 7: hole no 231 to 260

Set 8: hole no 261 to 300

Set 9: hole no 301 to 330

In Figure 5.11a, estimates of the PSD of data Sets 1, 2, and 3 (corner wear  $0.076 \text{ mm}^2$ ) of drill BL are overlaid. It can be seen that the estimate of PSD's for Sets 1, 2 and 3 is approximately the same. This means that at the same state of wear, PSD of the sensor signals do not change. Figures 5.11b and 5.11c show the same plots over a number of holes for Sets 4, 5, and 6 (corner wear  $0.28 \text{ mm}^2$ ), and Sets 7, 8, and 9 (corner wear  $0.43 \text{ mm}^2$ ) respectively. On examining Figures 5.11a through 5.11c and Figure 5.4, it can be concluded that PSD of the sensor signals must be functions of drill wear, because drill wear is the only factor that has changed during hole Sets 2, 5 and 8 which are at different



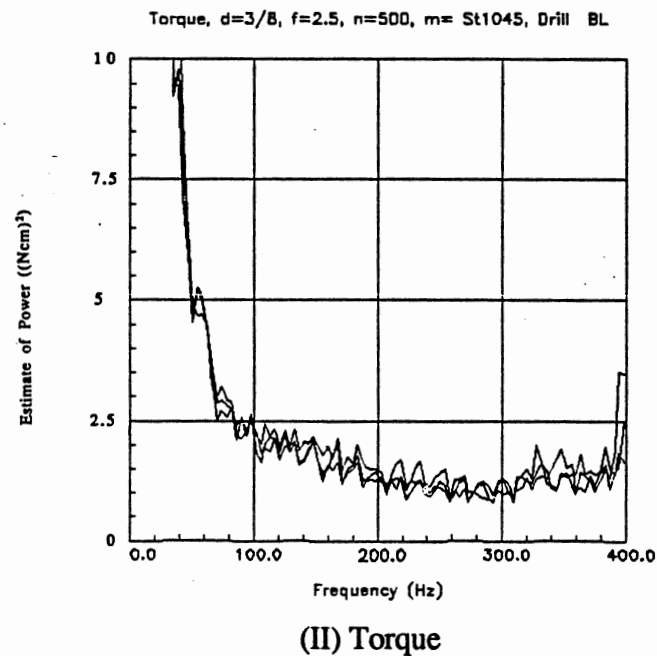
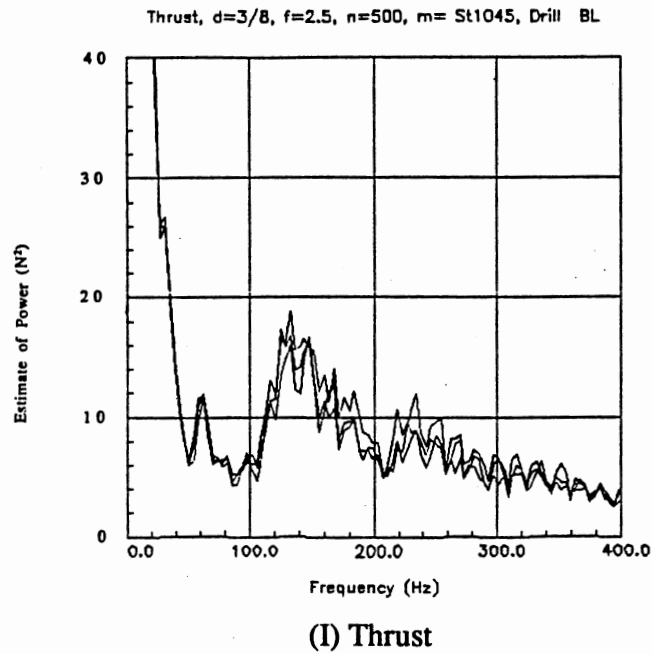
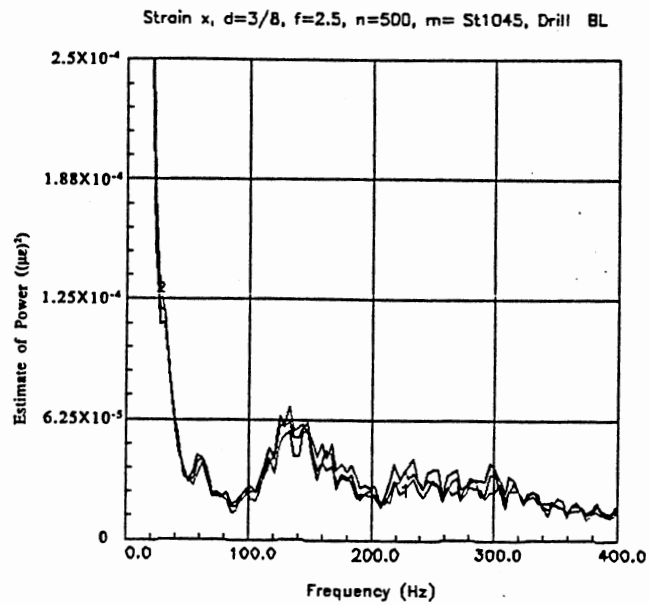
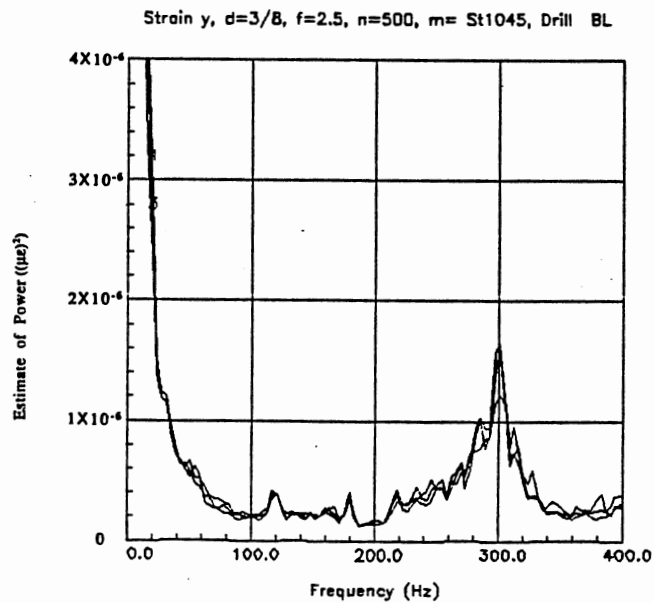


Figure 5.11a Estimate of PSD of Sensor Signals Over a Number of Holes at the Same State of Drill Wear. (1) Set 1: From Hole No. 11 to 40, (2) Set 2: From Hole No. 41 to 80, (3) Set 3: From Hole No. 81 to 110, for Drill BL. (I) Thrust, (II) Torque. For 3/8 in. drill bit, Cutting speed = 50 ft/min (500 rpm spindle speed), Feed rate = 0.005 in/rev (2.5 in./min), Work material AISI 1045 Steel (230 BHN).



(III) Strain in the X Direction



(IV) Strain in the Y Direction.

Figure 5.11a (Continued) (III) Strain in the X direction (IV) Strain in the Y direction.

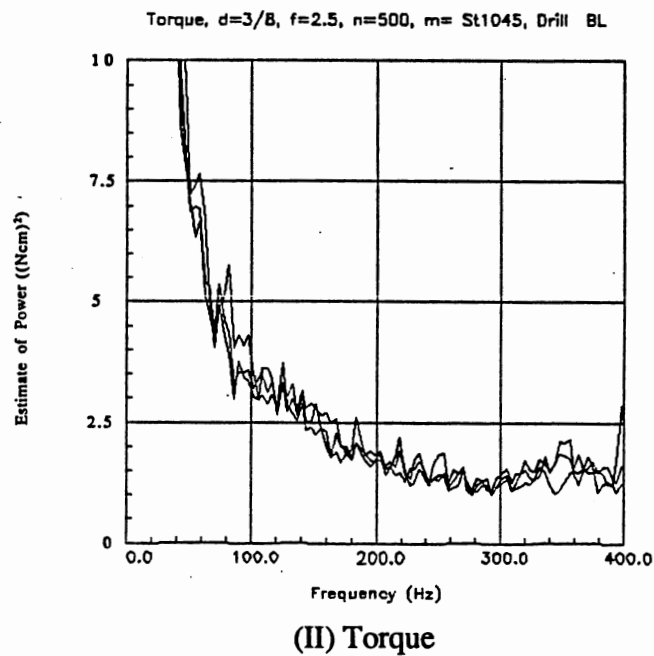
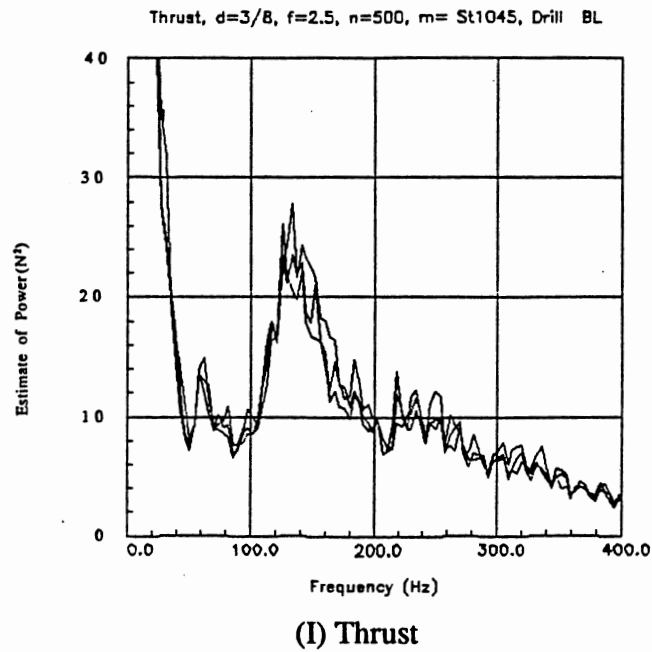
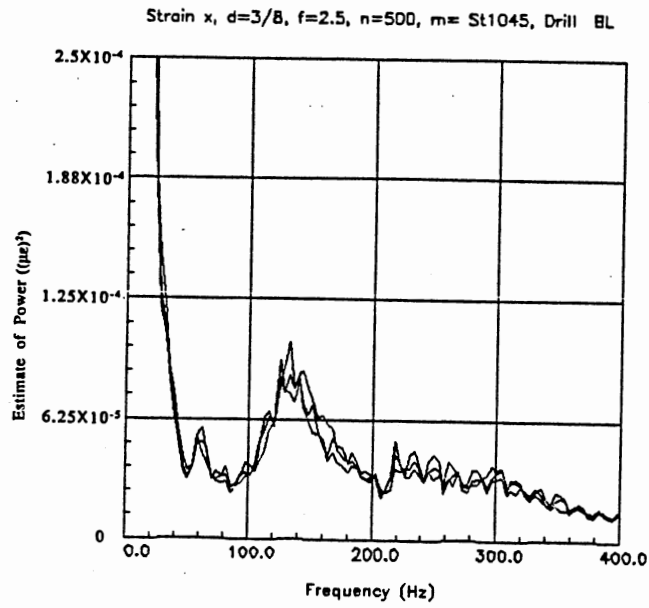
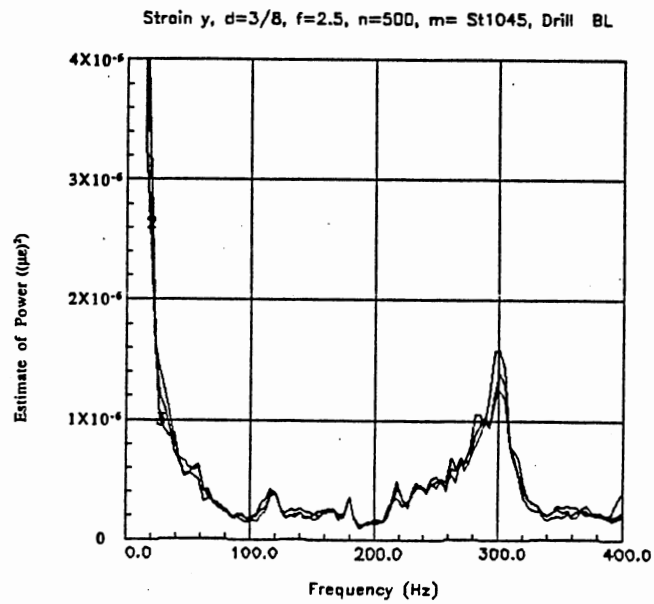


Figure 5.11b Estimate of PSD of Sensor Signals Over a Number of Holes at the Same State of Drill Wear. (1) Set 4: From Hole No. 121 to 150, (2) Set 5: From Hole No. 151 to 190, (3) Set 6: From Hole No. 191 to 220, for Drill BL (I) Thrust, (II) Torque. For 3/8 in. drill bit, Cutting speed = 50 ft/min (500 rpm spindle speed), Feed rate = 0.005 in/rev (2.5 in./min), Work material AISI 1045 Steel (230 BHN).



(III) Strain in the X Direction



(IV) Strain in the Y Direction.

Figure 5.11b (Continued) (III) Strain in the X direction (IV) Strain in the Y direction.

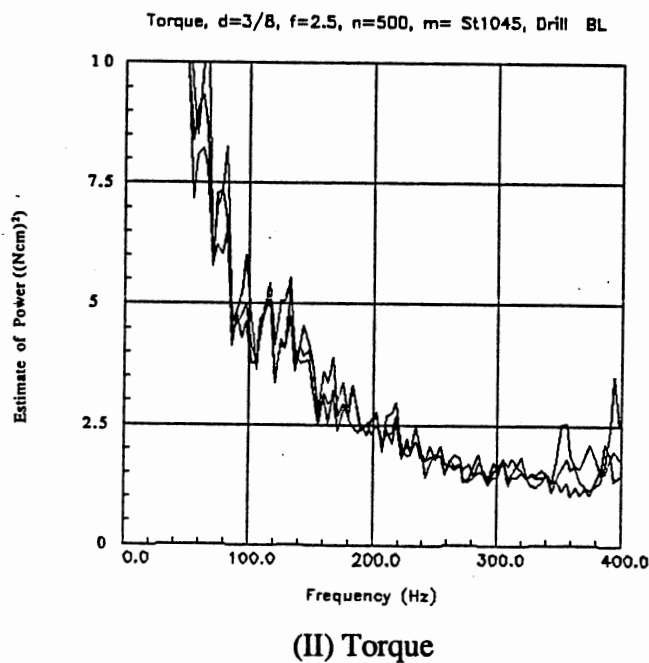
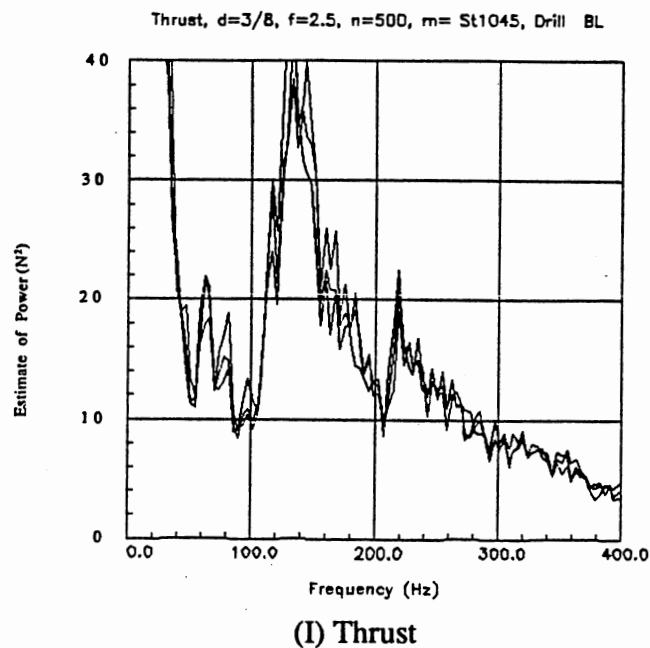
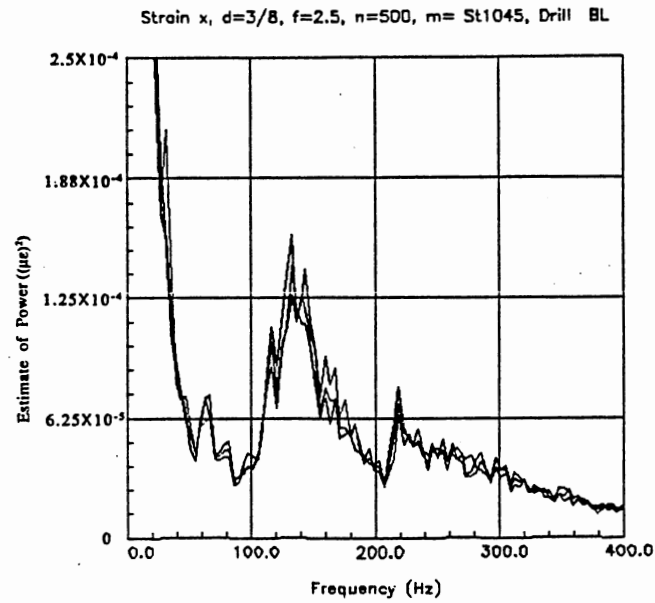
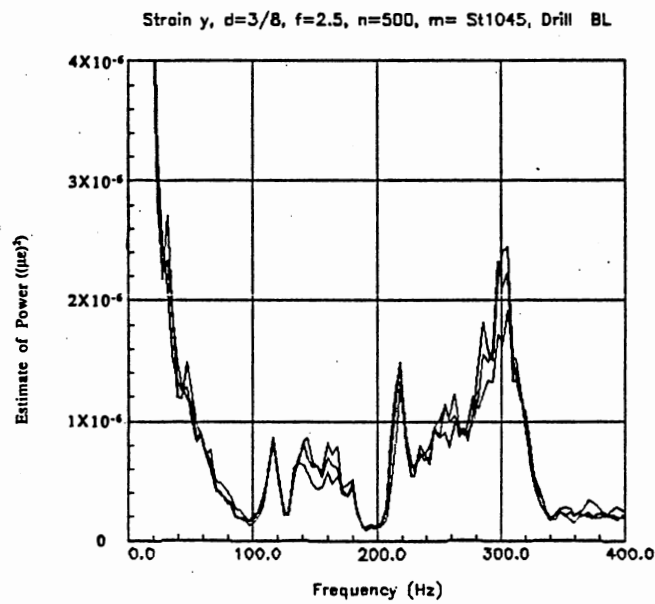


Figure 5.11c Estimate of PSD of Sensor Signals Over a Number of Holes at the Same State of Drill Wear. (1) Set 7: From Hole No. 231 to 260, (2) Set 8: From Hole No. 261 to 300, (3) Set 9: From Hole No. 301 to 330, for Drill BL (I) Thrust, (II) Torque. For 3/8 in. drill bit, Cutting speed = 50 ft/min (500 rpm spindle speed), Feed rate = 0.005 in/rev (2.5 in./min), Work material AISI 1045 Steel (230 BHN).



(III) Strain in the X Direction



(IV) Strain in the Y Direction.

Figure 5.11c (Continued) (III) Strain in the X direction (IV) Strain in the Y direction.

states of drill wear, while PSD's of data sets at the same state of drill wear are coincident (repeatability).

Figures 5.12 (I) to (IV) are PSD's of one data set from each state of drill wear, i. e. Set 2, set 5 and Set 8 plotted together, for further clarification of change in PSD with drill wear. In this figure change of area with respect to drill wear is more apparent. This figure also suggests that there might be some proportional change among PSD's of data Sets 2, 5, and 8. Therefore, the PSD's of all three data sets are normalized, i. e. the area under each PSD plot is made equal to one. For this propose, the area under the PSD plot between two different frequencies, namely,  $f_1$  and  $f_n$  is calculated using the trapezoid method (see Figure 5.13) as follows

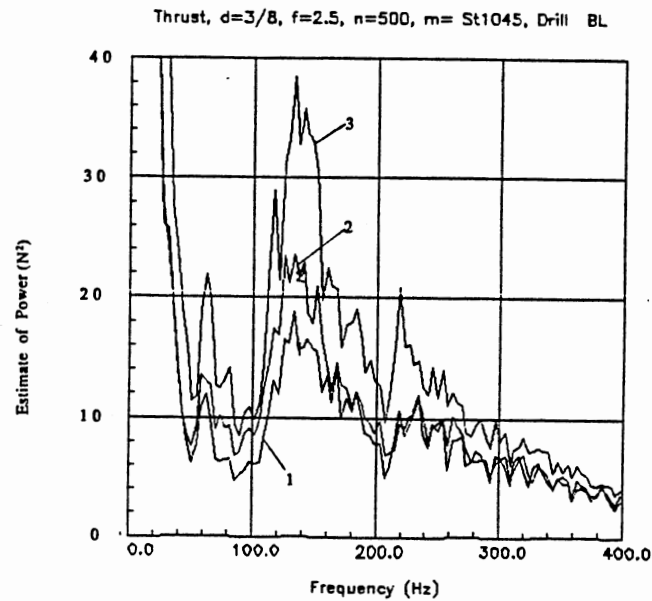
$$A = \frac{\Delta f}{2} (\text{Power}(f_1) + 2\text{Power}(f_2) + 2\text{Power}(f_3) + \dots + 2\text{Power}(f_{n-1}) + \text{Power}(f_n)) \quad (5.2)$$

Where  $\Delta f = f_{i+1} - f_i$ , is frequency resolution. The normalized power at each frequency is obtained by

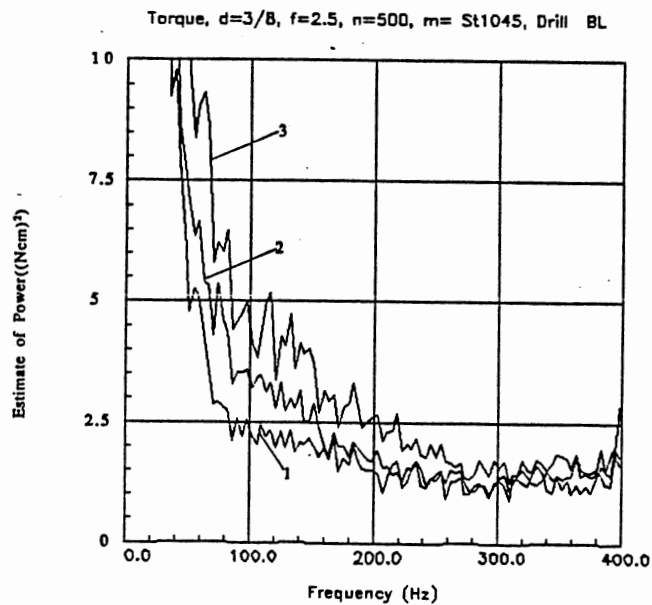
$$\text{Normalized Power at } f_i = \text{Power}(f_i)/A \quad (5.3)$$

This procedure reduces the area under the PSD plots between  $f_1$  and  $f_n$  to one. Figure 5.14 shows the normalized PSD plots for three sets, 2, 5, and 8, between 20 and 380 Hz. As can be seen, all of the normalized PSD plots are coincident with each other. This means that the only change is the gain or the input to the system with respect to change of drill wear while all other parameters of the system remaining constant

As mentioned earlier, the mean of each data segment was subtracted from the sensor signal. Figure 5.9 shows that very high peaks are present at the low frequencies close to zero on the PSD plots of all sensor signals. Due to leakage, power at the lower



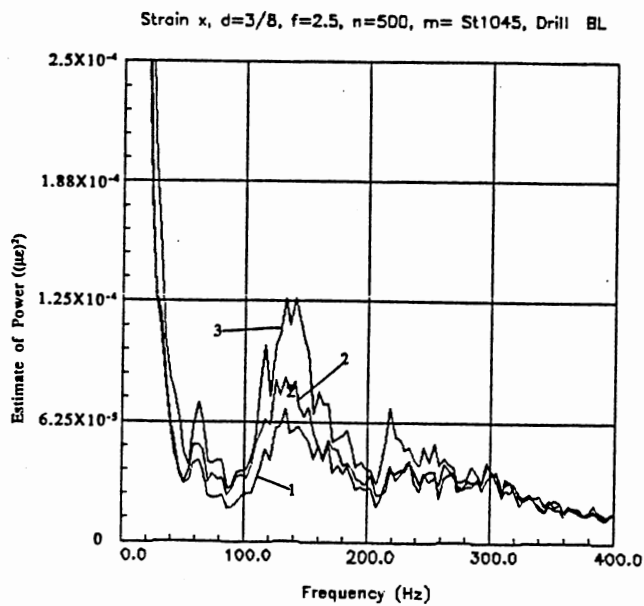
(I) Thrust



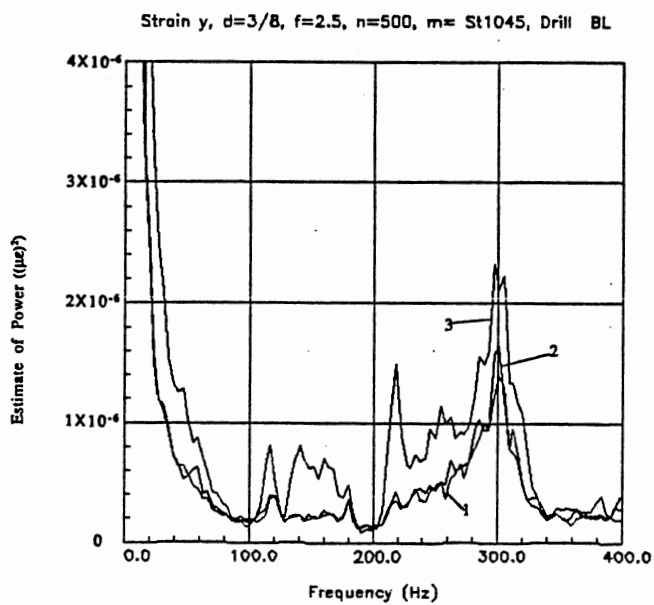
(II) Torque

Figure 5.12 Estimate of PSD of Sensor Signals Over a Number of Holes at Different States of Drill Wear. (1) Set 2: From Hole No. 41 to 80, (2) Set 5: From Hole No. 151 to 190, (3) Set 8: From Hole No. 261 to 300, for Drill BL (I) Thrust, (II) Torque. For  $3/8$  in. drill bit, Cutting speed = 50 ft/min (500 rpm spindle speed), Feed rate = 0.005 in/rev (2.5 in./min), Work material AISI 1045 Steel (230 BHN).





(III) Strain in the X Direction



(IV) Strain in the Y Direction.

Figure 5.12 (Continued) (III) Strain in the X direction (IV) Strain in the Y direction.

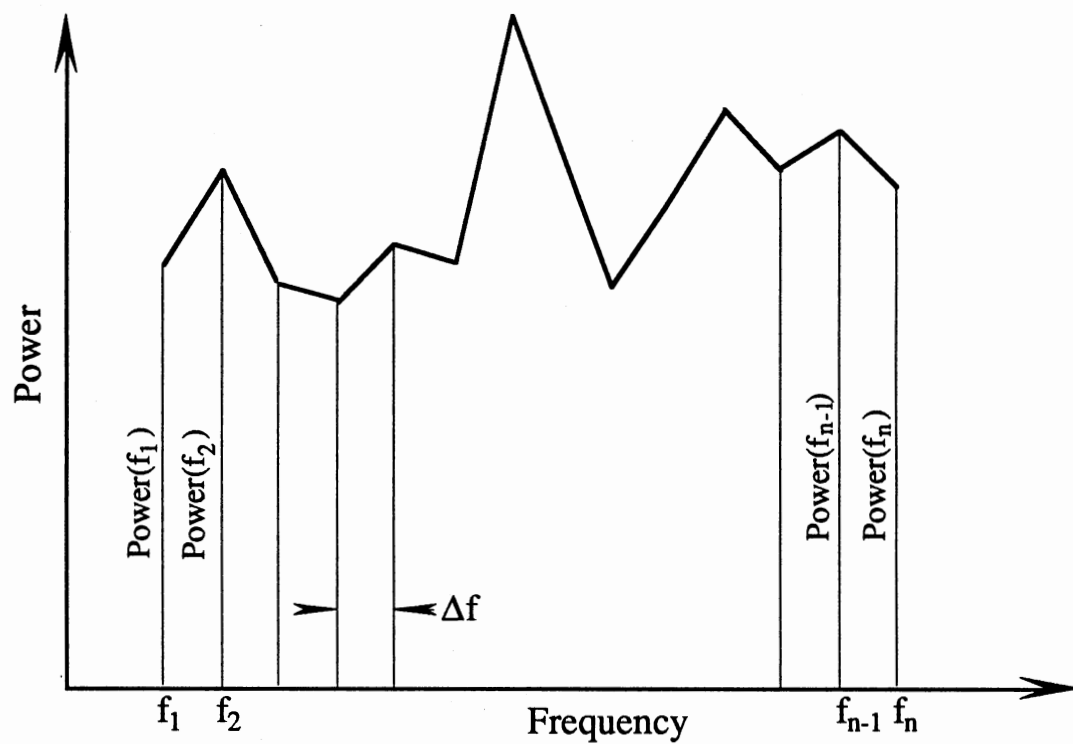
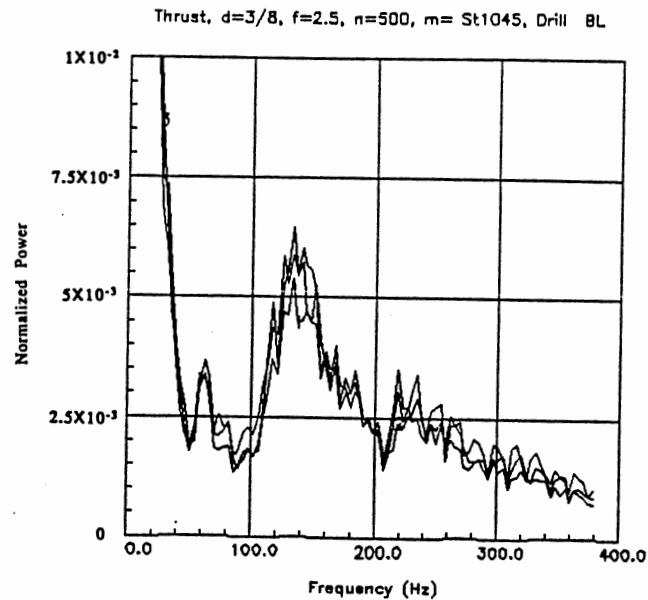
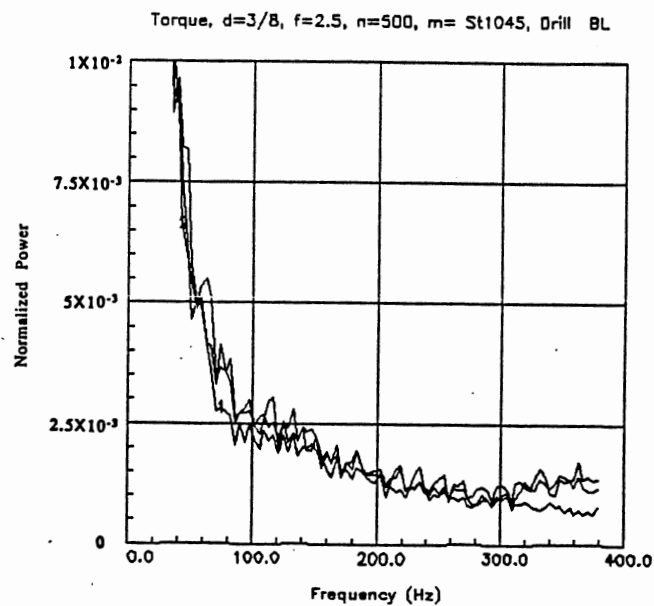


Figure 5.13 Calculation of the Area Under the PSD Using Trapezoidal Method.

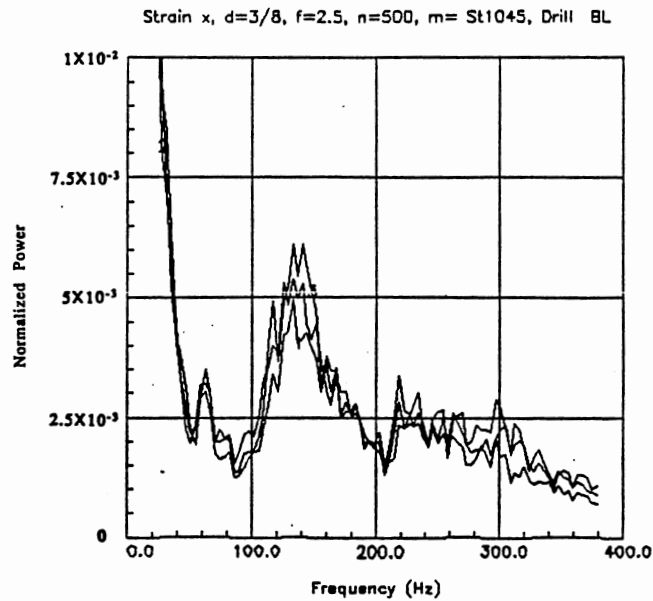


(I) Thrust

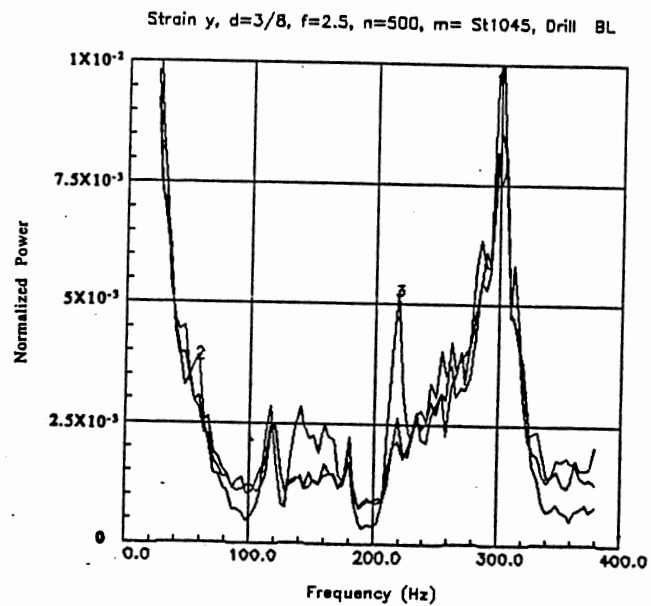


(II) Torque

Figure 5.14 Normalized PSD (Frequency Range 20 to 380 Hz) of Sensor Signals Over a Number of Holes at Different State of Drill Wear. (1) Set 2: From Hole No. 41 to 80, (2) Set 5: From Hole No. 151 to 190, (3) Set 8: From Hole No. 261 to 300, for Drill BL (I) Thrust, (II) Torque. For 3/8 in. drill bit, Cutting speed = 50 ft/min (500 rpm spindle speed), Feed rate = 0.005 in/rev (2.5 in./min), Work material AISI 1045 Steel (230 BHN).



(III) Strain in the X Direction



(IV) Strain in the Y Direction.

Figure 5.14 (Continued) (III) Strain in the X direction (IV) Strain in the Y direction.

frequencies are, therefore, not reliable. Due to low signal-to-noise ratio of the estimate of the PSD of the sensor signals above 300 Hz, the area under the PSD at these regions are also not reliable. For normalizing the PSD plots, frequencies below 20 Hz and above 380 Hz were not considered. As seen in Figure 5.14, the three sets of normalized PSD of torque signal above 300 Hz (300-380 Hz) are not coincident. This is due to low signal-to-noise ratio of the PSD of torque signal over these frequencies.

### 5.6 Correlation of Wear With the Area Under the PSD Plots

As shown in the previous sections, the PSD of sensor signals increases with increasing drill wear. From the normalized PSD plots (Figure 5.14) we can also see that all of the normalized PSD plots at different states of drill wear are coincident. It is well known that integration decreases the error. Therefore, instead of considering the variation of the PSD at any one frequency, we consider the change of area under the PSD plot as a criterion for drill wear. We can write

$$\Delta A_{\text{PSD}} = f(w) \quad (5.4)$$

Figures 5.4, 5.5a, and 5.5b show that wear extends from the corner to the center of the drill bit along the cutting edge. Figure 5.15 (I) and (II) show schematics of a sharp and a worn drill bit. From the Taylor tool life formula for cutting, we have

$$V^m T = C_1 \quad (5.6)$$

Let  $A_{T_1}$  be wear area at which tool failure is initiated when cutting speed is  $V_1$ . Tool life associated with this cutting condition is  $T_1$ . If cutting speed is increased to  $V_2$  ( $V_2 > V_1$ ) according to Equation 5.6, tool life will decrease to  $T_2$  ( $T_2 < T_1$ ). Soderberg et al [17] found that drill failure is initiated at smaller wear area at higher cutting speed, i. e.

$A_{T_2} < A_{T_1}$ . If a linear correlation is assumed between  $T$  and  $A_T$  then Equation 5.6 can be modified to

$$V^m A_T = C_2 \quad (5.7)$$

As tool failure is initiated by high temperatures due to the heat generated, constant  $C_2$  may be related to some level of generated energy (heat) at which cutting tool collapses. Therefore, it may be assumed that the generated energy, similarly to the change in the area under the PSD plots (which is energy of sensor signals) are function of  $V^m A_T$ . For a drill bit, Equation 5.6 can be written as

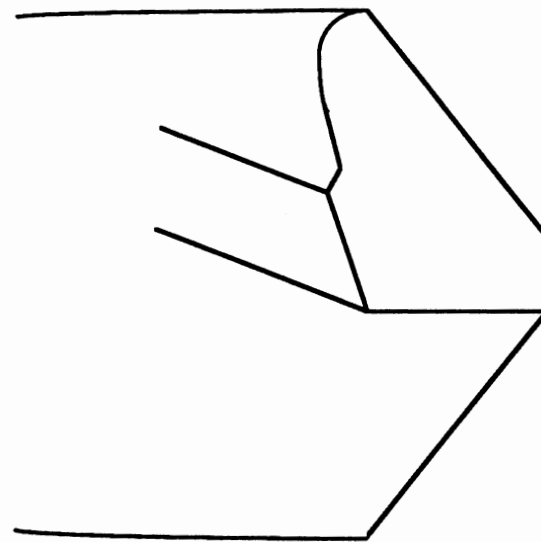
$$\Delta A_{\text{PSD}} = f\left(\int_{\text{Wear Area}} v^m dA\right) = f\left(\sum_{\text{Wear Area}} v_i^m \Delta A_i\right) \quad (5.8)$$

where  $v = 2\pi\rho n$  then

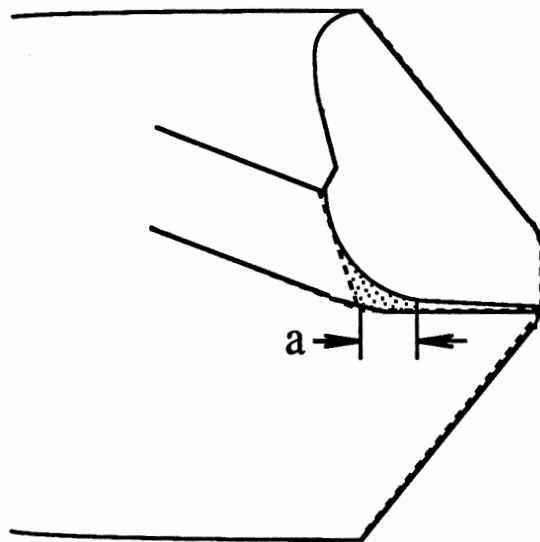
$$\Delta A_{\text{PSD}} = f((2\pi n)^m \sum_{\text{Wear Area}} \rho_i^m \Delta A_i) \quad (5.9)$$

Where  $\rho_i$  is the distance between the location of  $\Delta A_i$  on the cutting edge and the axis of the drill bit. Figures 5.5a and 5.5b show that the worn area near the corner is larger than any other part of the drill wear and  $\rho$  gets its maximum value,  $r$  (radius of the drill) at the corner. If  $m$  is large (in Taylor tool life formula  $m$  is 10 for high speed steel for the turning process) the following approximation can be made:

$$\sum_i \rho_i^m \Delta A_i \cong r^m A_{\text{cw}} \quad (5.10)$$



(I) Sharp Drill



(II) Worn Drill

Figure 5.15 Schematic of a Sharp and a Worn Drill bit. (I) Sharp drill, (II) Worn Drill, the Sharp Drill is Overlaid and Shown by Dashed Line.

Where  $A_{cw}$  is the projection of the total wear area of both corners of the drill bit on a plane perpendicular to the axis of a drill bit. Substituting Equation 5.10 in Equation 5.9, we have

$$\Delta A_{PSD} = f((2\pi nr)^m A_{cw}) = g(A_{cw}) \quad (5.11)$$

$A_{cw}$  is calculated from the SEM micrographs of the drill bits at any given state of drill wear.

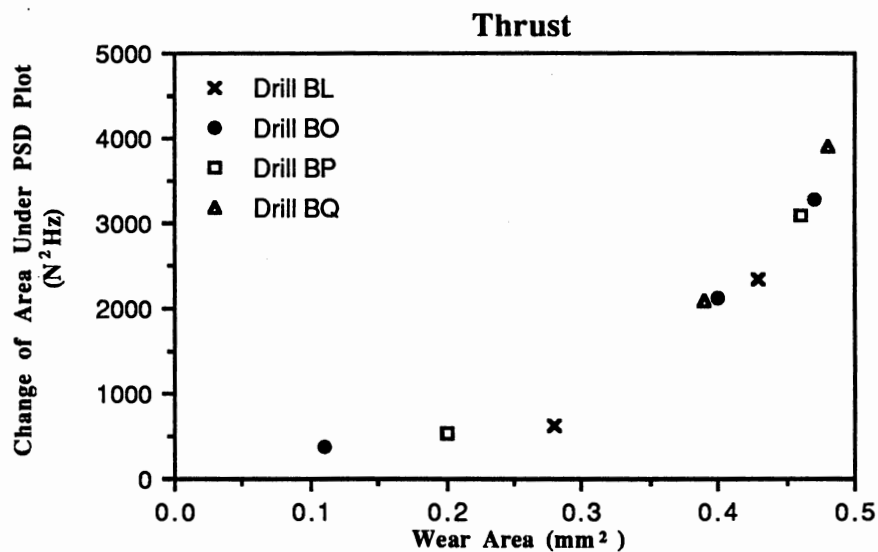
Figure 5.15 shows a schematic of the corner wear area (shaded area). In this figure the sharp tool is overlaid on tool of the worn tool and indicated by dashed line. Distance  $a$  is measured from the corner of a sharp tool along the cutting edge. This area is calculated by adding up the areas of triangles and trapezoids that make up this area. Let  $A_p$  be the calculated area of both corners of the drill bit from the SEM micrograph. Then, the projection of this area on the plane perpendicular to the drill axis is given by

$$A_{cw} = A_p s^2 \tan(p/2) \quad (5.12)$$

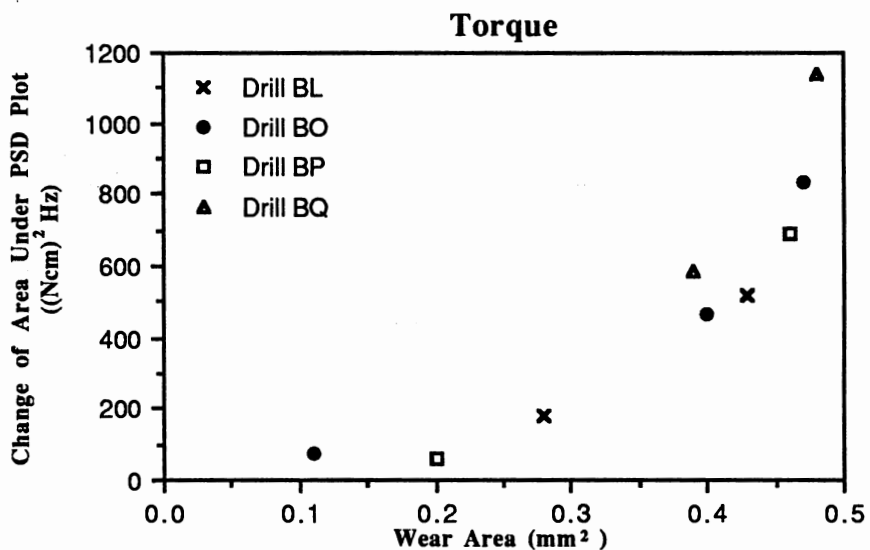
Where  $s$  is the scale of SEM micrographs designated on the picture and  $p$  is the point angle of the drill bit. The effect of clearance angle is neglected due to its small influence. Clearance angle is generally between  $8^\circ$ - $12^\circ$  and  $\cos(12^\circ) = 0.978$ , therefore its effect can be neglected.

In this investigation the wear areas of both corners are measured along 0.4 mm of the cutting edge for 3/8 in. drill. Figures 5.16 (I) to (IV) show plots of the wear area vs. the change of area under the PSD for drills BL, BO, BP and BQ. In this figure, the area under the PSD of sensor signal is measured between 50 and 300 Hz. The frequencies above 300 Hz and below 50 Hz are not considered due to the consideration discussed in the previous section.





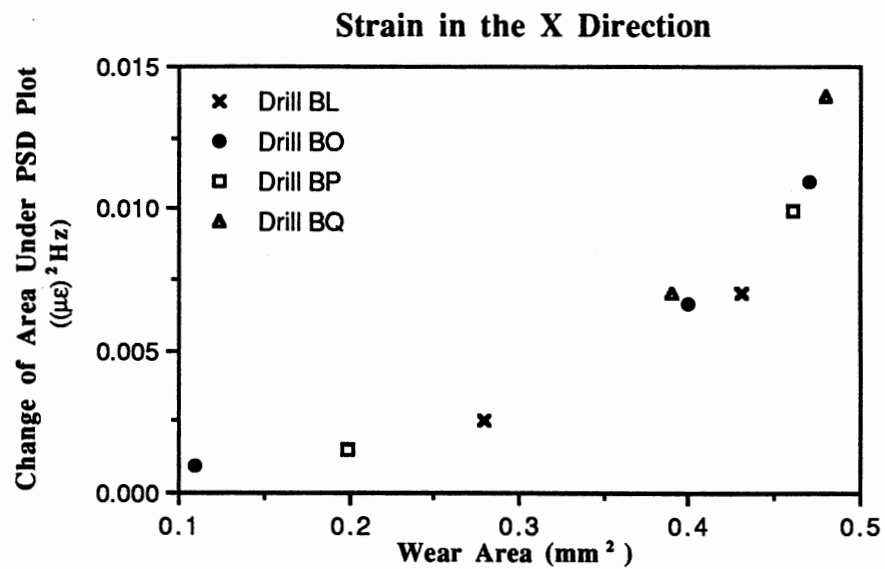
(I) Thrust



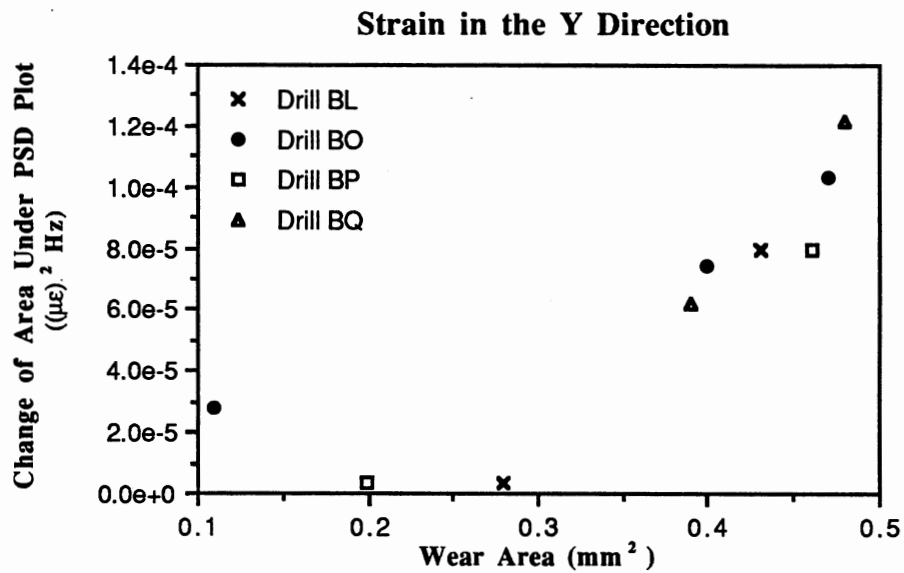
(II) Torque

Figure 5.16 Plot of Wear Area vs. Change of Area Under the PSD for Drills BL, BO, BP and BQ.

Drill bit 3/8 in. , Normal cutting: Cutting speed: 50 ft/min (spindle speed: 500 rpm), Feed: 0.005 in/rev (2.5 in/min), Work material 1045 steel (230 BHN).



(III) Strain in the X Direction



(IV) Strain in the Y Direction

Figure 5.16 (Continued) (III) Strain in the X Direction, (IV) Strain in the Y Direction.

## 5.7 Conclusions

In this Chapter time and frequency domains of four sensor signals, namely, thrust, torque, strains in the X- and Y-directions were investigated. It was observed that if the recommended cutting speed and feed are used, wear rate would be negligible over a number of holes. Therefore, signals from all of these holes may be considered to be from the same state of drill wear. For accelerating drill wear higher cutting speed than recommended speed was used.

In the time domain mean and variance of the sensor signals of each hole were calculated and plotted against the number of holes. No significant change in the mean and variance of sensor signals was noted in the time domain with respect to the change of drill wear.

In the frequency domain, Welch method (see Chapter IV for details) was used for the calculation of power spectral density (PSD). Average of the six periodograms (of six data segments from each hole for all sensor signals) was found to be noisy. It indicates that six periodograms are not sufficient for this propose. However, an average of the periodograms over a number of holes with negligible wear development would be satisfactory. Noise associated with the PSD of sensor signals was found to decrease significantly. In this investigation it was observed that the PSD plots of all sensor signals were coincident at any state of drill wear (repeatability, see Figures 5.11a to 5.11c). Signal-to-noise analysis indicated that power at frequencies between 50 and 300 Hz have the highest value of signal-to-noise ratio, and hence, are the most reliable frequencies. Comparison of the PSD plots showed that power at each frequency increases with increase in drill wear. Normalized PSD plots of all of the four sensor signals at different states of drill wear were coincident. This indicates that power at all frequencies increases proportionally with increase in drill wear. Therefore, the change of area under the PSD plots was considered instead of power at one frequency, for integration decreases the error.

The change in the area under the PSD plots of all (four) sensor signals were plotted against the total corner wear. It was observed that change of area under the PSD plots of three sensor signals, namely, thrust, torque, and strain in the X-direction showed good correlation with drill wear. Correlation between change of area under the PSD plots of strain in the Y-direction and drill wear was not as good as those of the other three sensors.

CHAPTER VI  
INVESTIGATION OF THE SENSOR INTEGRATION  
TECHNIQUE USING THE RESULTS  
OF THIS STUDY

Tool wear monitoring is an essential component of an automated cutting process. As a result, considerable research in various research laboratories around the world is centered around this purpose. The machining process, in spite of its apparent simplicity, is quite a complex process and there are many aspects of it that are still not well understood. Sufficiently accurate model that enables one to identify the nature and location of tool wear by monitoring sensor signals has not been available. A number of techniques for sensing tool wear and for identifying tool fracture have been proposed, but a few, if any have found application in industry. Consequently, totally untended machining remains a far distant goal. While tool fracture is a sudden event, which needs to be forecasted sufficiently in advance, so as to prevent any major catastrophe to the part or the tool itself, tool wear is a slowly evolving phenomenon.

Due to the complexity of the machining process and the lack of sufficiently accurate model of the process many researchers have sought methods of sensor integration, such as artificial neural networks, that do not need any theoretical or empirical model of the process. Artificial neural network, described in Chapter III, is a technique which mimics the computational architecture of a human brain. As mentioned earlier artificial neural network applied to metal cutting uses one of the following methods for pattern classification.

1. Classification using clustering technique.

2. Classification using mapping technique.
3. Classification using decision surfaces.

In chapter III it was pointed out that for tool wear estimation, mapping and clustering techniques were used.

In the last decade or so some researchers have concerned themselves with the control of the machining process using sensor fusion via neural network. Kannatey-Asibu [10] explored the possibility of using pattern recognition technique for monitoring the condition of the tool in a cutting operation using acoustic emission (AE) as a specific example. Dornfeld and Pan [11] used simple hyperplane decision surface for the determination of the chip forming state. Emel and Kannatey-Asibu [12, 13] and Balakrishnan et al [62] used the same technique for monitoring tool wear and fracture. After the introduction of a training algorithm by Rumelhart et al [54] for the multi-layer back propagation (BP) neural network which is able to approximate almost any function, mapping technique received considerable attention. Rangwala and Dornfeld [14, 15] used BP neural network for the tool wear monitoring. They reported a success rate of 95%. Mapping technique (see Figure 3.13 for clarification of the technique) for continuous function approximation was used by Chryssolouris and Domroese [63] for the evaluation of flank wear in orthogonal cutting, using RMS of AE signal, force, and temperature as inputs to the network. Clustering technique has also been applied to metal cutting problems [41, 43]. ART2 neural network (clustering technique) was used for tool wear monitoring by Tansel [41]. A combination of parameter estimation and Kohonen self organizing map was applied to tool wear monitoring by Kamarthi et al [43].

Artificial neural network structures are based on our present understanding of the biological nervous system [44]. Although an artificial neural network model, with crude brain-like structure, has great potential in the areas of pattern recognition and modelling of highly nonlinear systems using general architecture, at this stage, they are, however, far from reaching the performance of a brain [44]. In this chapter, the necessity and

possibility of sensor integration for drill wear monitoring are investigated. Time domain sensor signals will not be considered, because they did not show good correlation with drill wear. Therefore, frequency domain of sensor signals will be investigated in detail.

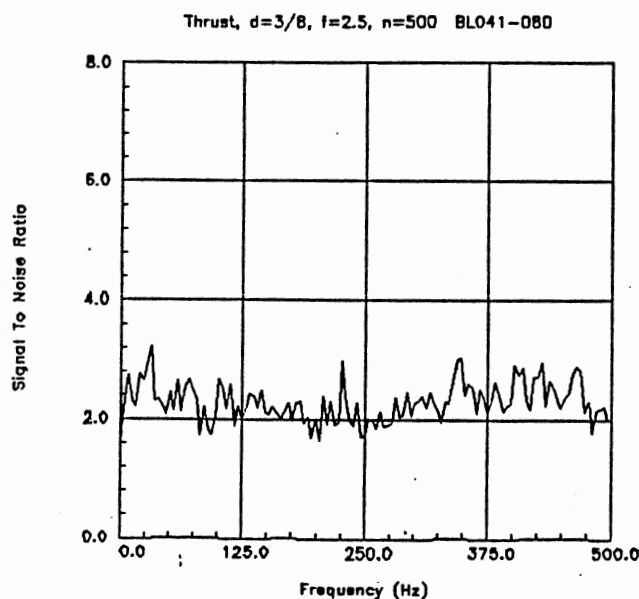
### 6.1 Necessity for the Application of Sensor Integration

Examination of Figure 5.16 shows that change of area under PSD plots of thrust, torque and strain in the X direction have good correlation with drill wear. While strain in the Y direction showed some correlation with drill wear it is not found to be as good as those of the other sensors. In the design of any system one of the objectives is to design the simplest and the most effective system. This fact implies that it is not necessary to implement any sensor integration system when one sensor is adequate. Implementing a tool monitoring system with three sensor signals each of which has equally good correlation with drill wear as in the present investigation is making it more complicated. Therefore, signal from any one of these sensors, namely thrust, torque and strain in the X direction would be adequate for monitoring drill wear.

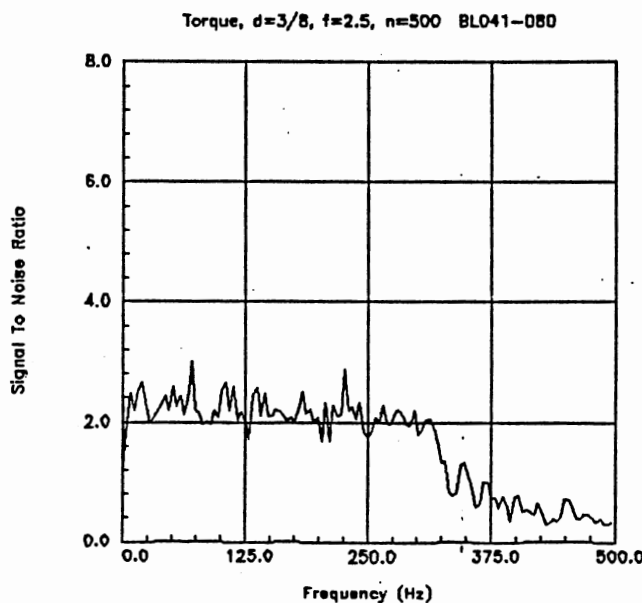
### 6.2 Possibility of Using Mapping Technique for Drill

#### Wear Evaluation

As mentioned in Chapters IV and V, standard deviation of the estimate of power at each frequency of one periodogram of sensor signal is equal to or greater than the magnitude of mean of the power at that frequency of sensor signal. In Chapter V it was shown that the signal-to-noise ratio is 2.2 when periodograms of six data sets with a 50% overlap are averaged. Figures 6.1a through 6.1c show signal-to-noise ratio at different states of drill wear (total corner wear areas for drill BL 0.076 mm<sup>2</sup>, 0.28 mm<sup>2</sup>, and 0.43 mm<sup>2</sup> respectively) when periodogram of six data sets with a 50% overlap are averaged. As can be seen, the ratio of 2.2 is valid for all states of drill wear. In Chapter V it was shown that the power of sensor signal at all frequencies increases with increase in tool wear.



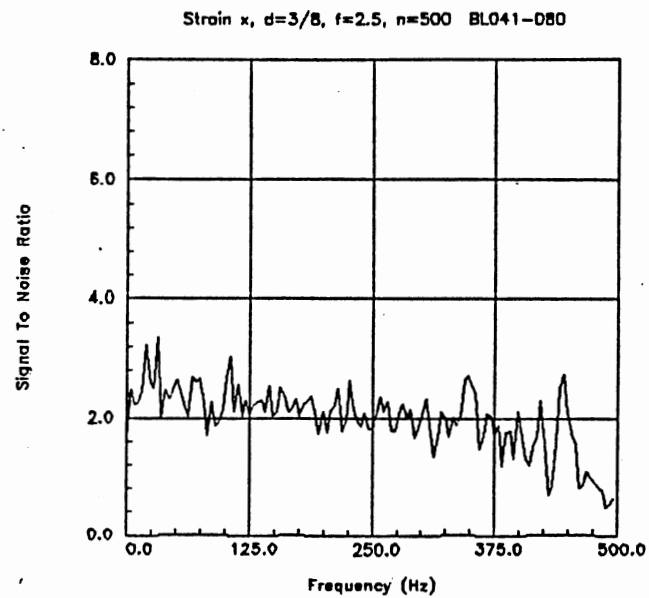
(I) Thrust



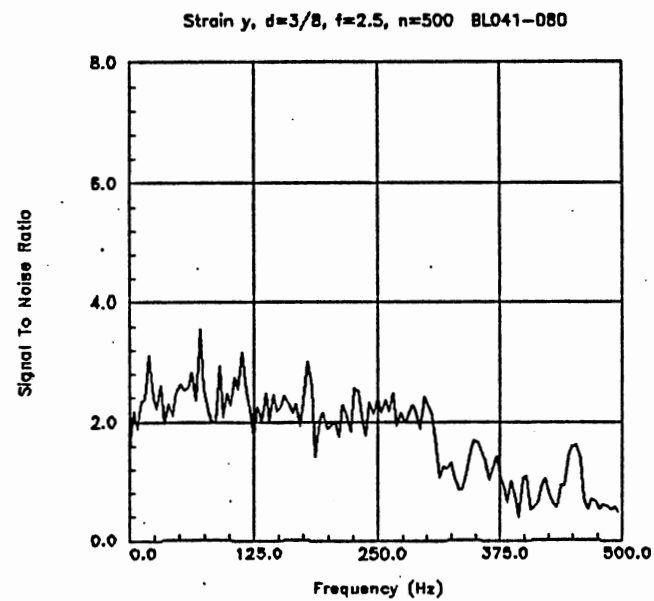
(II) Torque

Figure 6.1a Signal-to-Noise Ratio of the Sensor Signals in the Frequency Domain Over 40 Holes (From Hole No. 41 to Hole No. 80), Corner Wear:  $0.076 \text{ mm}^2$ , for Drill BL. (I) Thrust, (II) Torque. For  $3/8$  in. drill bit, Cutting speed 50 ft/min (500 rpm spindle speed), Feed rate 0.005 in/rev (2.5 in./min), Work material AISI 1045 Steel (230 BHN).





(III) Strain in the X Direction



(IV) Strain in the Y Direction.

Figure 6.1a (Continued) (III) Strain in the X Direction (IV) Strain in the Y direction.

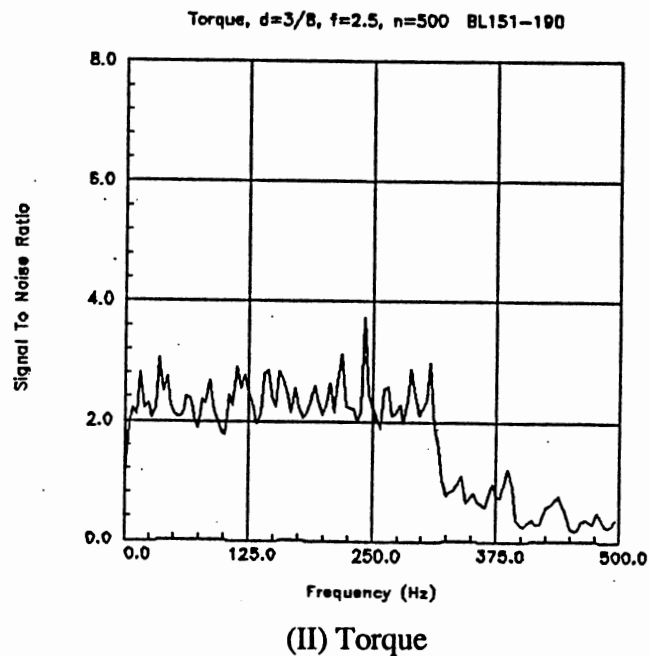
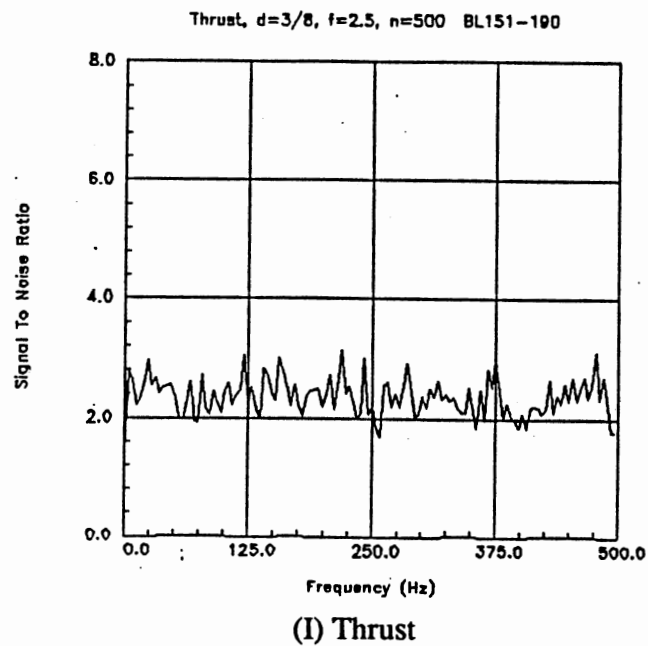
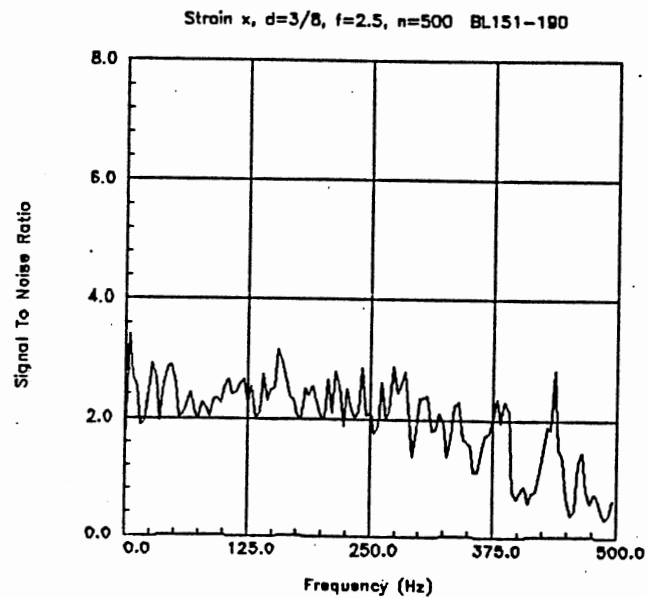
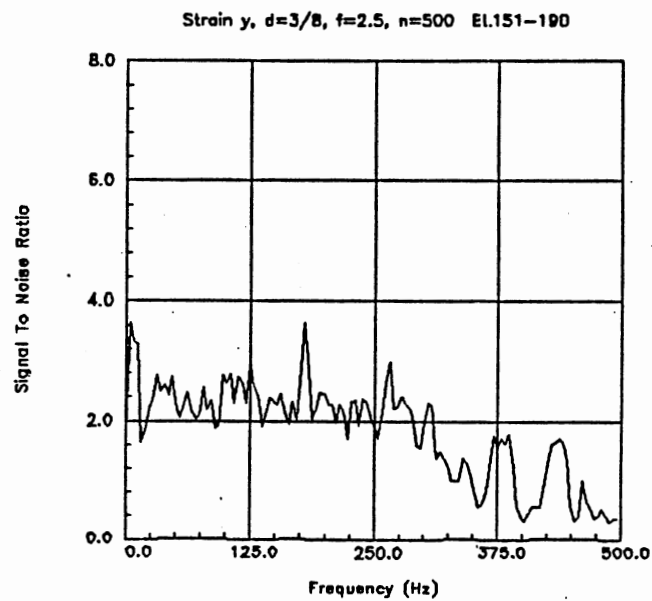


Figure 6.1b Signal-to-Noise Ratio of the Sensor Signals in the Frequency Domain Over 40 Holes (From Hole No. 151 to Hole No. 190), Corner Wear: 0.28 mm<sup>2</sup>, for Drill BL. (I) Thrust, (II) Torque. For 3/8 in. drill bit, Cutting speed 50 ft/min (500 rpm spindle speed), Feed rate 0.005 in/rev (2.5 in./min), Work material AISI 1045 Steel (230 BHN).

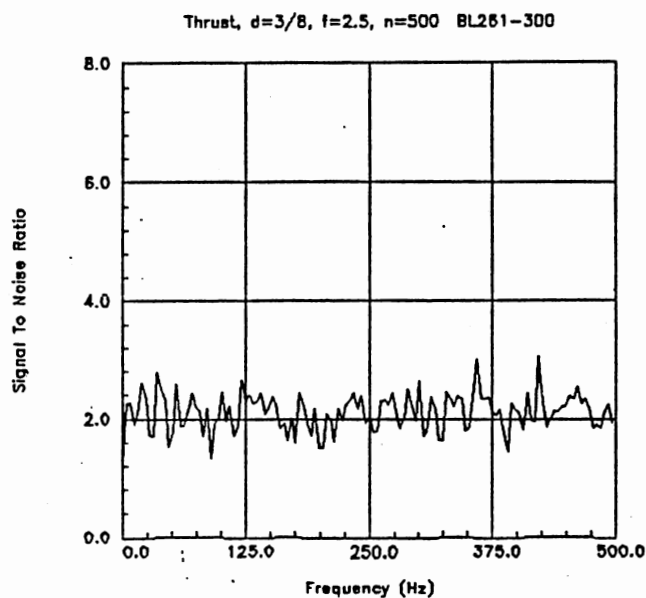


(III) Strain in the X Direction

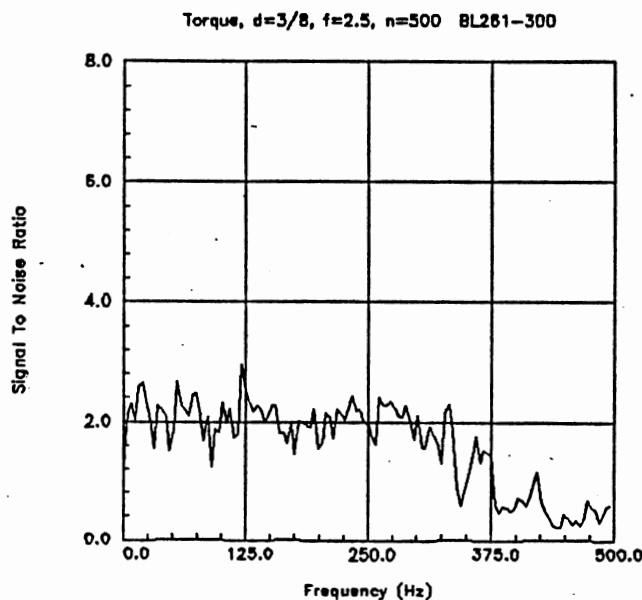


(IV) Strain in the Y Direction.

Figure 6.1b (Continued) (III) Strain in the X Direction (IV) Strain in the Y direction.

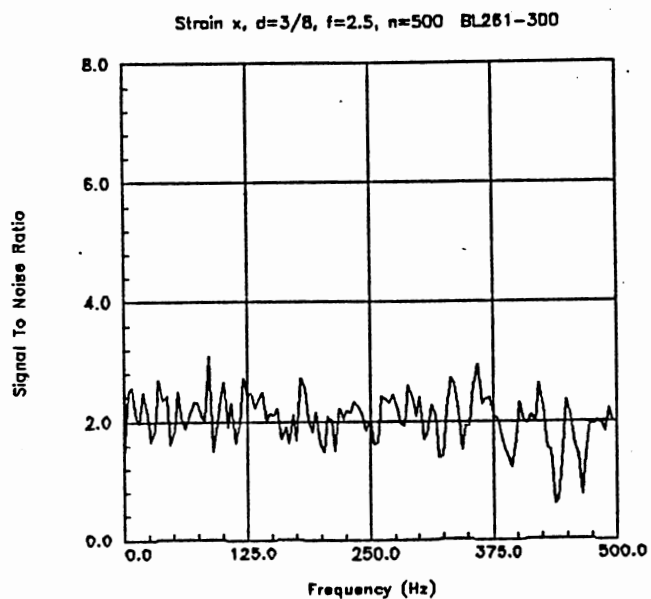


(I) Thrust

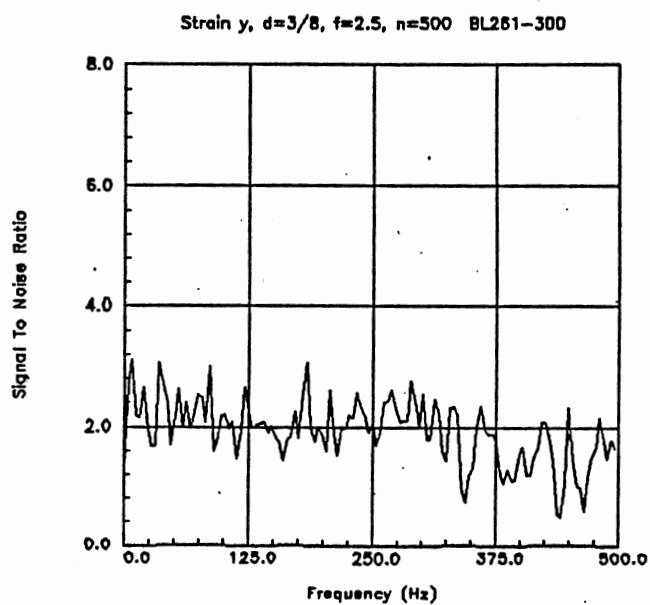


(II) Torque

Figure 6.1c Signal-to-Noise Ratio of the Sensor Signals in the Frequency Domain Over 40 Holes (From Hole No. 261 to Hole No. 300), Corner Wear:  $0.43 \text{ mm}^2$ , for Drill BL. (I) Thrust, (II) Torque. For  $3/8$  in. drill bit, Cutting speed 50 ft/min (500 rpm spindle speed), Feed rate 0.005 in/rev (2.5 in./min), Work material AISI 1045 Steel (230 BHN).



(III) Strain in the X Direction



(IV) Strain in the Y Direction.

Figure 6.1c (Continued) (III) Strain in the X Direction (IV) Strain in the Y direction.

Therefore, increase in tool wear results in increase in standard deviation of the estimate of power at each frequency of the sensor signals.

Figures 6.2 (I) to (X) show the cross correlations of the estimate of power at various frequencies of the sensor signals either for the same sensor and or for two sensors. It can be seen from this figures that in the frequency domain, the estimate of power at any two frequencies either for one sensor or for two different sensors are uncorrelated. But some correlation may be observed between two different sensors at the same frequency. Therefore, all inputs from the frequency domain to neural network are contaminated with uncorrelated noises. The standard deviation of these noises is equal to or greater then the magnitude of power at each frequency.

Figures 6.3 (I) to (X) show the cross correlation of the sensor signals in the time domain between any two holes either from one or two sensors. As shown, the noises in the time domain from thrust and torque sensor signals are also uncorrelated. Some correlation can be observed between strains in the X- and Y-directions and other sensor signals.

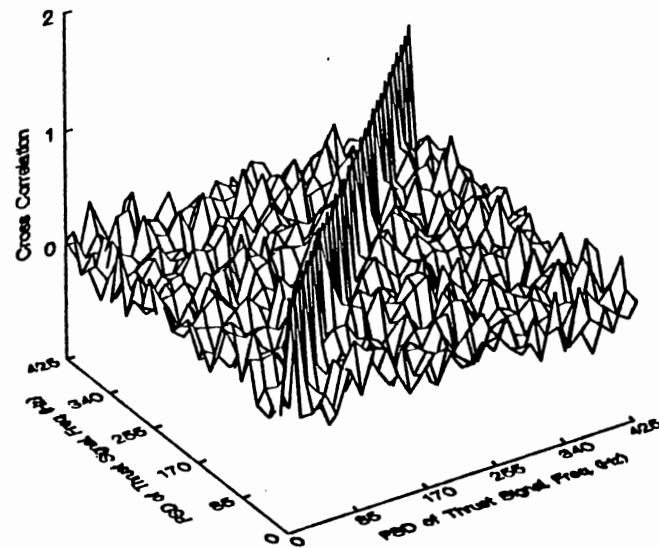
Let  $T$ ,  $M$ , and  $S_y$  be sensor signals from thrust, torque and strains in the X and Y directions respectively in the frequency domain . From Figure 5.16 it follows

$$A_{cw} = f_1(T) \quad (6.1a)$$

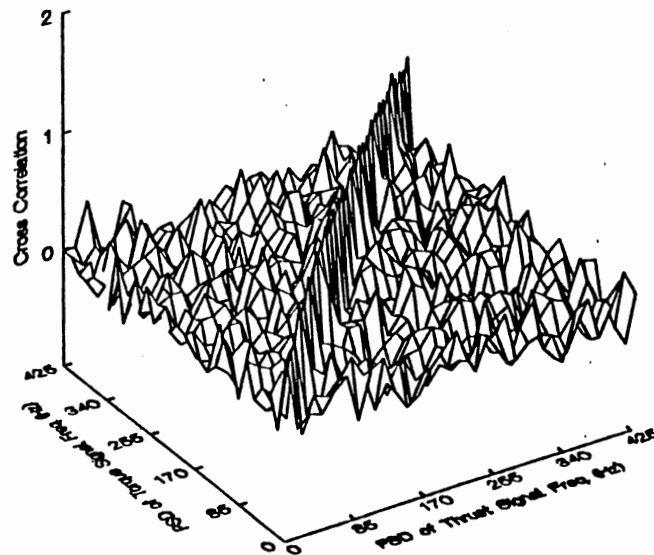
$$A_{cw} = f_2(M) \quad (6.1b)$$

$$A_{cw} = f_3(S_x) \quad (6.1c)$$

$S_y$  did not show good correlation with the drill wear. Thrust and torque sensors integration can be shown by



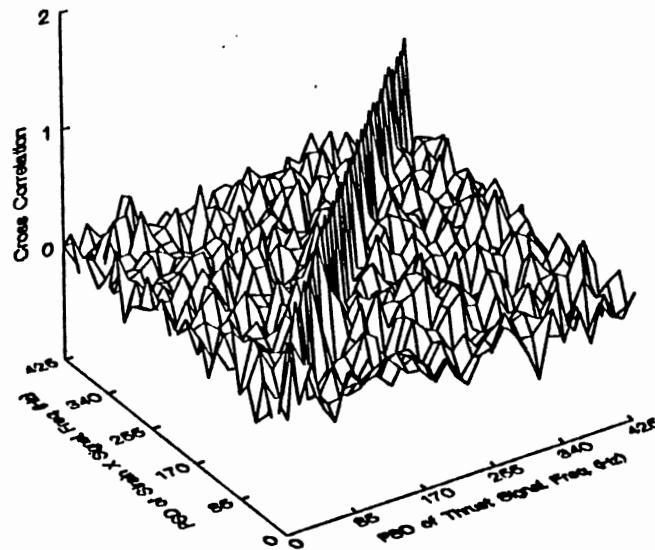
(I) Thrust and Thrust



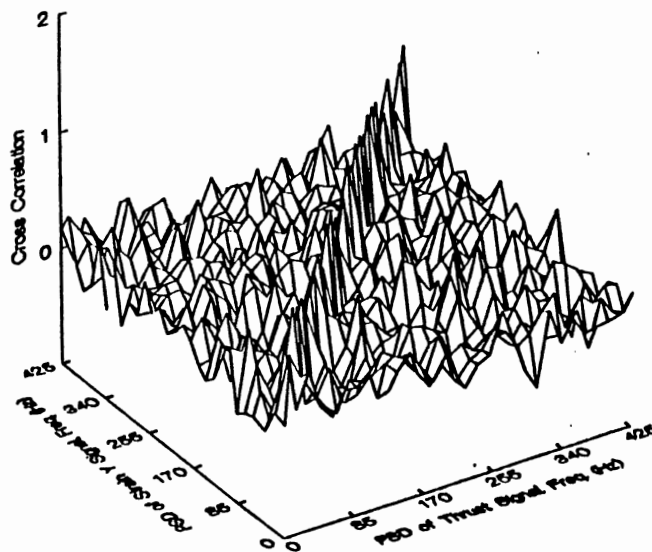
(II) Thrust and Torque

Figure 6.2 Cross Correlation of the Estimate of Power of Sensor Signals Between 0 and 425 Hz, for Holes From 240 to 279, For Drill BO. (I) Thrust and Thrust, (II) Thrust and Torque.

For 3/8 in. drill bit, Cutting speed 50 ft/min (500 rpm spindle speed), Feed rate 0.005 in/rev (2.5 in./min), Work material AISI 1045 Steel (230 BHN).



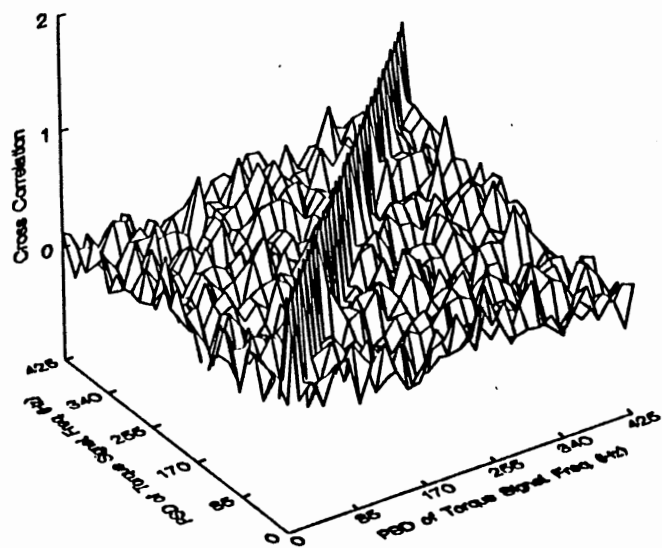
(III) Thrust and Strain in the X Direction



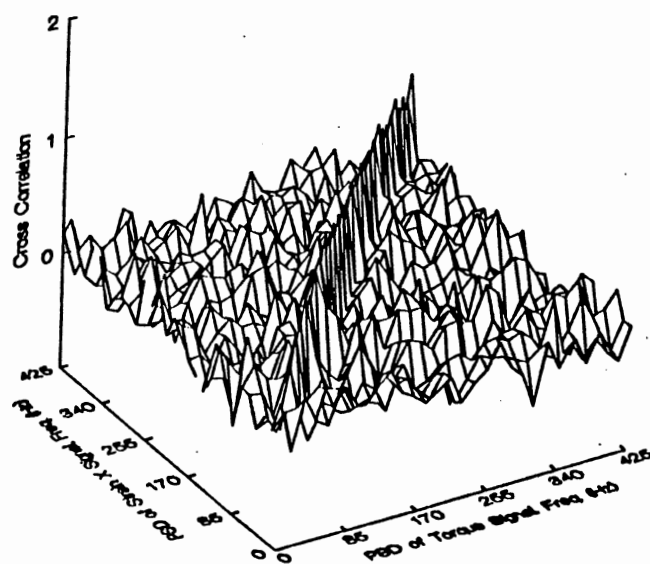
(IV) Thrust and Strain in the Y Direction.

Figure 6.2 (Continued) (III) Thrust and Strain in the X direction (IV) Thrust and Strain in the Y direction.



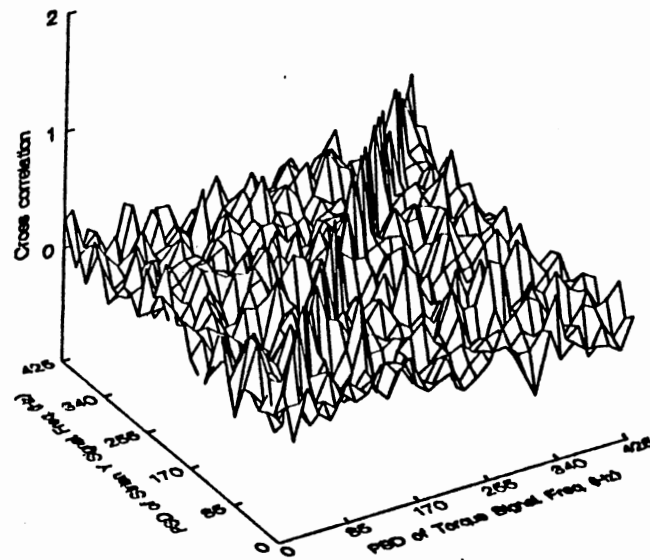


(V) Torque and Torque

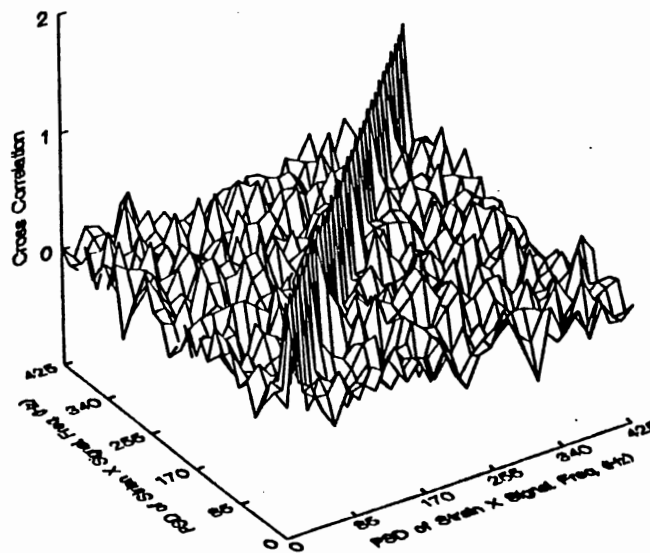


(VI) Torque and Strain in the X Direction.

Figure 6.2 (Continued) (V) Torque and Torque (VI) Torque and Strain in the X direction.

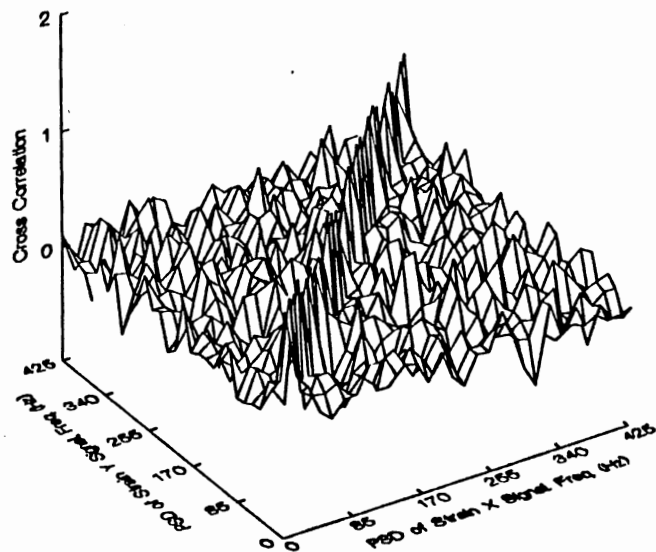


(VII) Torque and Strain in the Y Direction

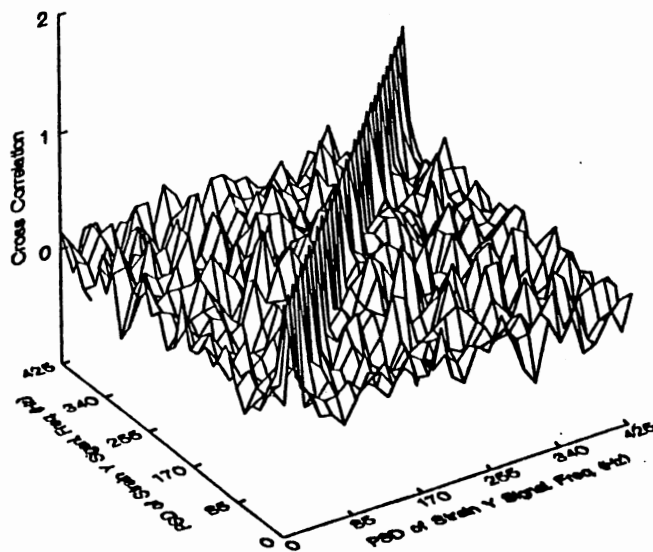


(VIII) Strain in the X Direction and Strain in the X Direction.

Figure 6.2 (Continued) (VII) Torque and Strain in the Y Direction  
 (VIII) Strain in the X Direction and Strain in the X Direction.

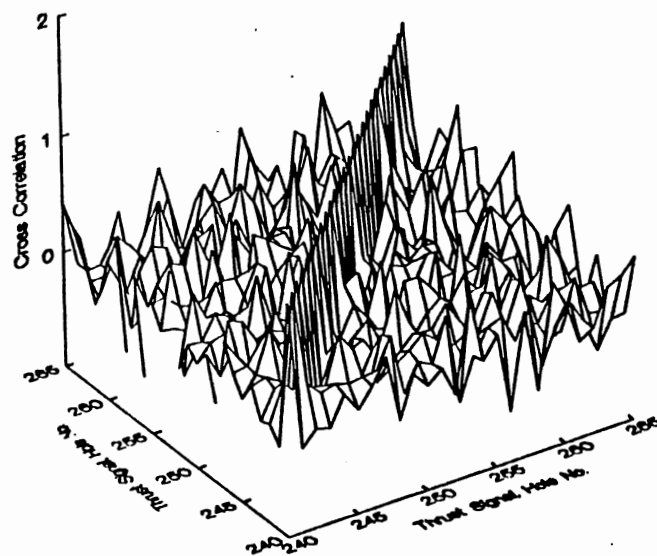


(IX) Strain in the X Direction and Strain in the Y Direction

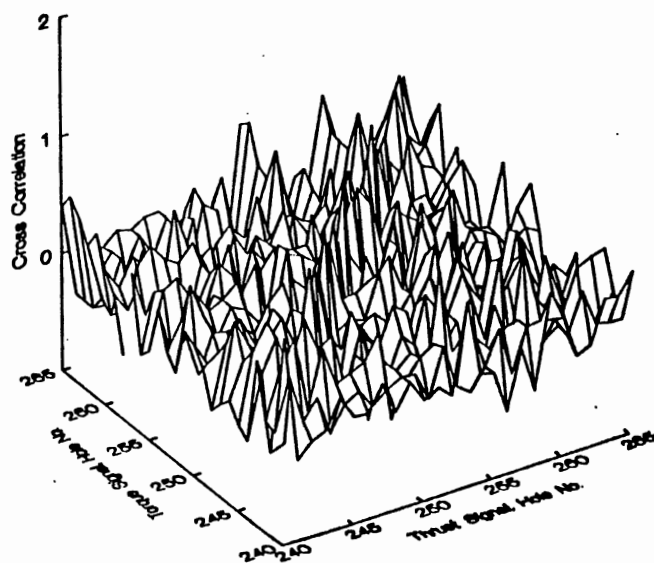


(X) Strain in the Y Direction and Strain in the Y Direction.

Figure 6.2 (Continued) (IX) Strain in the X Direction and Strain in the Y Direction  
(X) Strain in the Y Direction and Strain in the Y Direction.

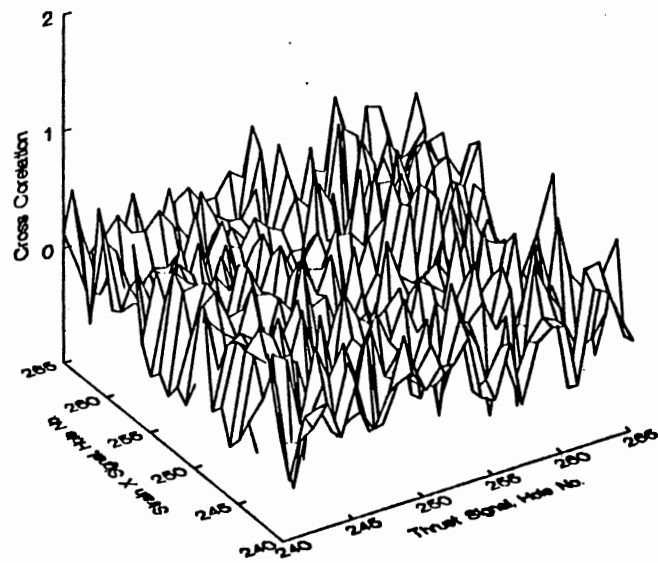


(I) Thrust and Thrust

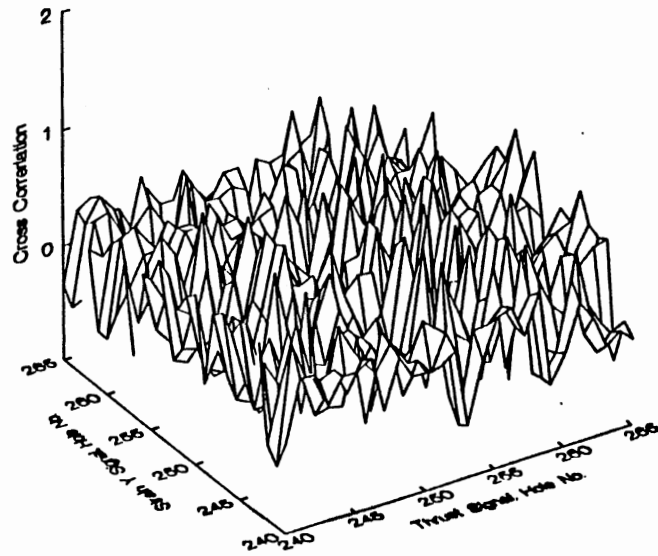


(II) Thrust and Torque

Figure 6.3 Cross Correlation of Sensor Signals in the Time Domain Between Holes 240 and 264 for Drill BO. (I) Thrust and Thrust, (II) Thrust and Torque. For 3/8 in. drill bit, Cutting speed 50 ft/min (500 rpm spindle speed), Feed rate 0.005 in/rev (2.5 in./min), Work material AISI 1045 Steel (230 BHN).

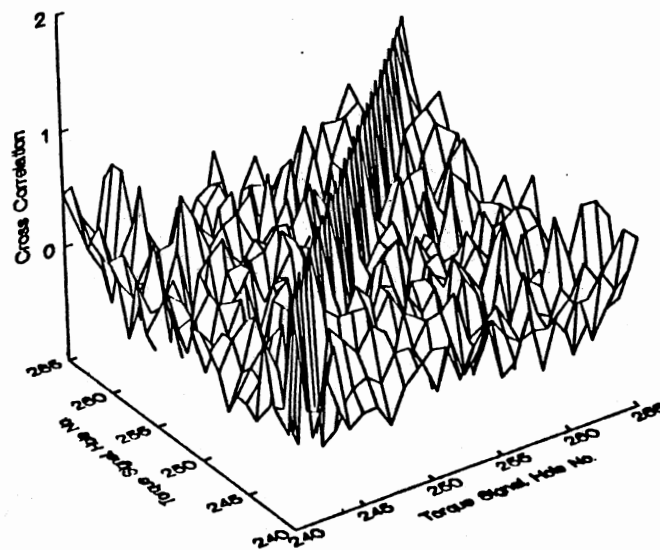


(III) Thrust and Strain in the X Direction

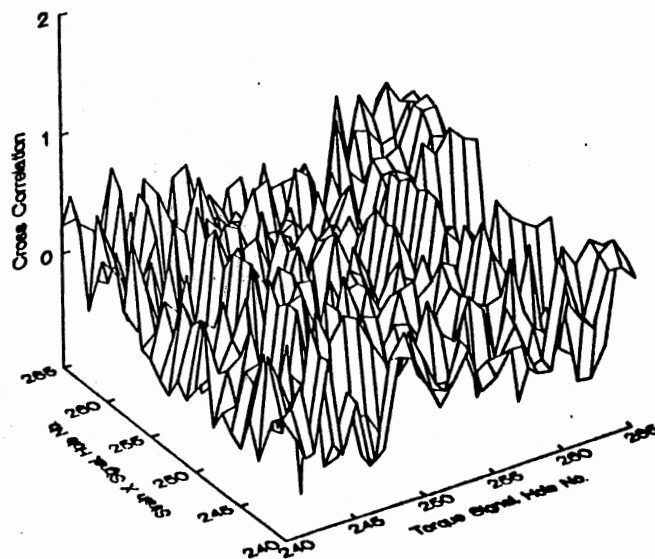


(IV) Thrust and Strain in the Y Direction.

Figure 6.3 (Continued) (III) Thrust and Strain in the X direction (IV) Thrust and Strain in the Y direction.

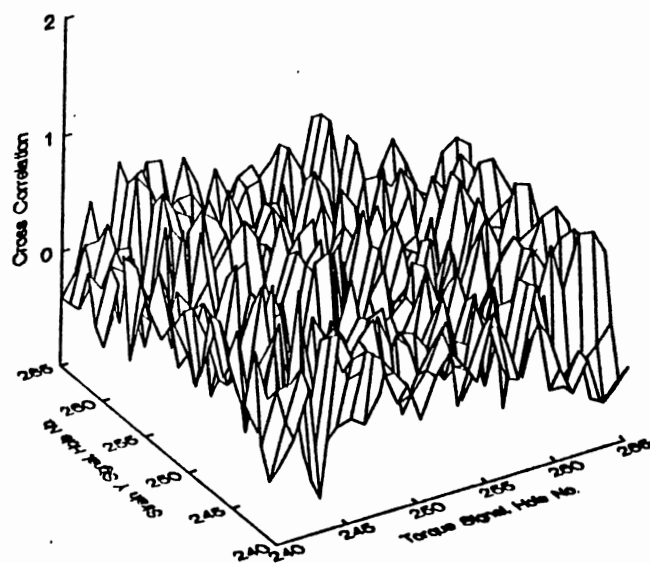


(V) Torque and Torque

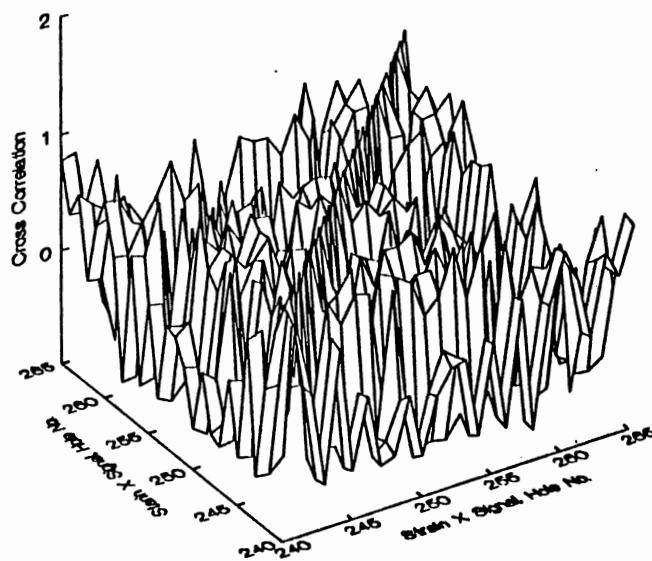


(VI) Torque and Strain in the X Direction.

Figure 6.3 (Continued) (V) Torque and Torque (VI) Torque and Strain in the X direction.

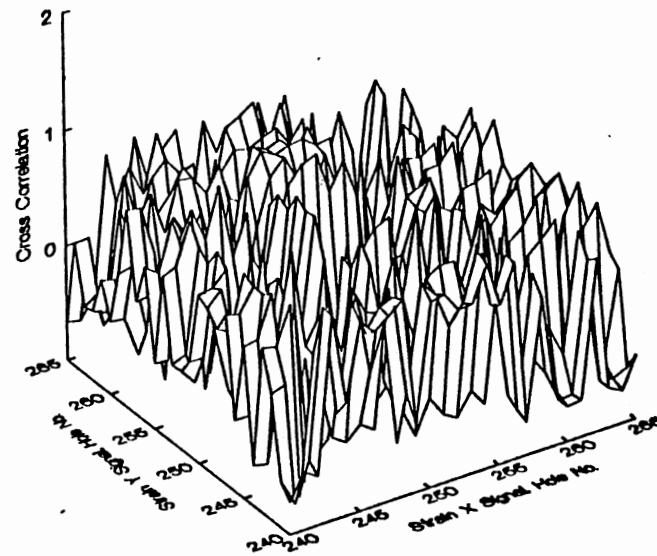


(VII) Torque and Strain in the Y Direction

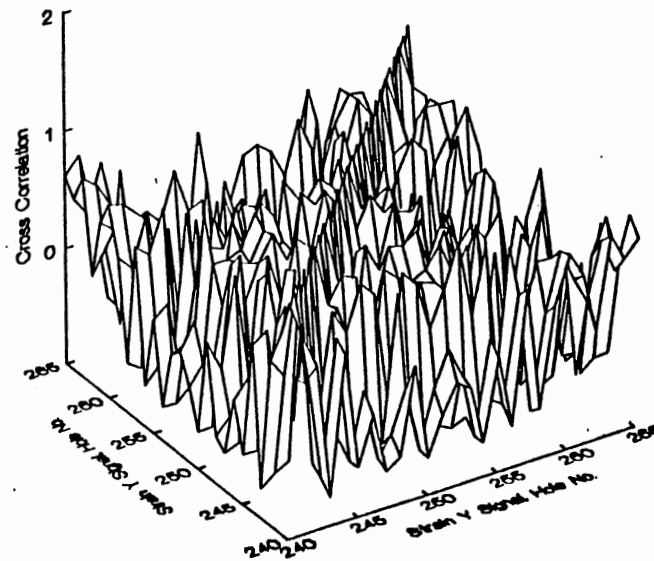


(VIII) Strain in the X Direction and Strain in the X Direction.

Figure 6.3 (Continued) (VII) Torque and Strain in the Y Direction  
 (VIII) Strain in the X Direction and Strain in the X Direction.



(IX) Strain in the X Direction and Strain in the Y Direction



(X) Strain in the Y Direction and Strain in the Y Direction.

Figure 6.3 (Continued) (IX) Strain in the X Direction and Strain in the Y Direction  
(X) Strain in the Y Direction and Strain in the Y Direction.



$$A_{cw} = g(T, M) \quad (6.2)$$

Function  $g(T, M)$  can take many forms. Consider the following example: Let

$$g(T, M) = \frac{f_1(T) + cf_2(M)}{c+1} \quad c \neq -1 \quad (6.3a)$$

or in a more general form

$$g(T, M) = \left( \frac{f_1(T)^m + c^2 f_2(M)^m}{c^2 + 1} \right)^{\frac{1}{m}} \quad (6.3b)$$

Depending on the value of  $c$  and  $m$ , Equation 6.3b represents different surfaces in a three dimensional space. It is clear that in any sensor integration  $c$  and  $m$  are not one of the inputs. In other words, it can be stated that states  $c$  and  $m$  are not accessible from the input. In the control literature such systems are designated as ‘uncontrollable systems’. Therefore, independent of sensor integration method being used, in the absence of noise, modeling such a system is difficult, if not impossible, and in the presence of uncorrelated noises associated with each sensor signal it appears impossible. If the values of  $c$  and  $m$  are given as inputs to the modeling technique there are other equations similar to 6.3b that may represent integration of thrust and torque. For example

$$g(T, M) = \sinh^{-1} \left( \frac{\sinh(f_1(T)) + c^2 \sinh(f_2(M))}{c^2 + 1} \right) \quad (6.3c)$$

Equations 6.3a through 6.3c represent surfaces in three dimensional space that intersect along a line shown by Equations 6.1a and 6.1b. Let noisy thrust and torque signals be used for training BP network. For every value of thrust and torque signals (signal + noise)

at any state of drill wear some value for  $C$  and  $m$  can be found that satisfies the Equation 6.3b. i. e. any point in the three dimensional space can satisfy this equation or any similar equation such as 6.3c in the presence of noise. Therefore, are thrust and torque signals (signal + noise) at any state of drill wear are valid data for the BP network, and BP network converges to all data points if its topology is complex enough to do so.

If another sensor signal is added, the sensor integration becomes more complicated.

For example

$$A_{cw} = \left( \frac{f_1(T)^m + c_1^2 f_2(M)^m + c_2^2 f_3(S_x)^m}{c_1^2 + c_2^2 + 1} \right)^{\frac{1}{m}} \quad (6.4)$$

This equation has more unknown parameters in comparison with Equation 6.3b. Therefore, adding one more sensor signal makes the modeling of the system more difficult. The main problem is there are several equations similar to 6.3b and 6.3c that have one common intersection along the line represented by Equation 6.1.

Till now we considered the case when all sensor signals are correlated with tool wear. Let us assume that  $S_y$  has no correlation with tool wear. Integration of this sensor signal with thrust signals gives

$$A_{cw} = f_1(T) + cS_y \quad (6.5)$$

For any value of the thrust signal  $T$  (signal plus noise), strain in the  $Y$  direction  $S_y$ , and tool wear  $A_{cw}$  there will be a value of  $C$  that can satisfy the above equation. Therefore, if one of the sensor signals do not correlate well with tool wear, the integration of that sensor with others will result in the deterioration of the sensor integration technique and hence it cannot model the system.

To illustrate the shortcomings of the neural network in sensor integration, the following computer simulation was made. Assume the correlation between the sensor signals thrust  $T$  and torque  $M$  and the drill wear  $w$  be given by the following equations.

$$w = 0.2 + 0.775\sqrt{T - 0.2} \quad (6.6a)$$

$$w = 0.2 + 0.85\sqrt{M - 0.2} \quad (6.6b)$$

The nature of these equations are similar to that shown in Figure 5.16. A uniformly distributed random noise (-0.25 to 0.25) with zero mean and standard deviation equal to 0.14 were added to  $T$  and  $M$  for training, but exact values of  $w$  was used for tool wear. If the standard deviation of the noise (0.14) is compared with the magnitude of  $T$  and  $M$ , it can be seen that it is between 0.7 ( $T = 0.2$ ) and 0.17 ( $T = 0.8$ ) which is much smaller than the standard deviation of the noise of the estimate of power of the signals in the current study. For some 51  $w$  values between 0.2 and 0.8, corresponding  $T$  and  $M$  values were obtained using the Equations 6.6 (a) and (b). To these  $T$  and  $M$  values, the above mentioned noises were added in order to prepare data for training a BP neural network with 2 inputs, 2 hidden nodes, and one output ( $2 \times 2 \times 1$ ). Figure 6.4 shows this neural network. Another 51 set of data points were used to test the network, using the same procedure, but with different values. After 40 iterations, the mean square error (MSE) was  $4.547 \times 10^{-3}$  which improved to  $4.353 \times 10^{-3}$  after 8741 iterations. The results of the computer simulation for training data on wear-thrust and wear-torque planes are shown in Figure 6.5aI and 6.5aII respectively. As can be seen, the trained BP network follows the training data (signal + noise) very closely but do not converge to the mean of the signal. Figures 6.5bI and 6.5bII show the function of a trained BP network for testing data set. It can be seen that the trained network can not follow the testing data (signal + noise) properly. These figures show that the output of the BP network covers almost the whole

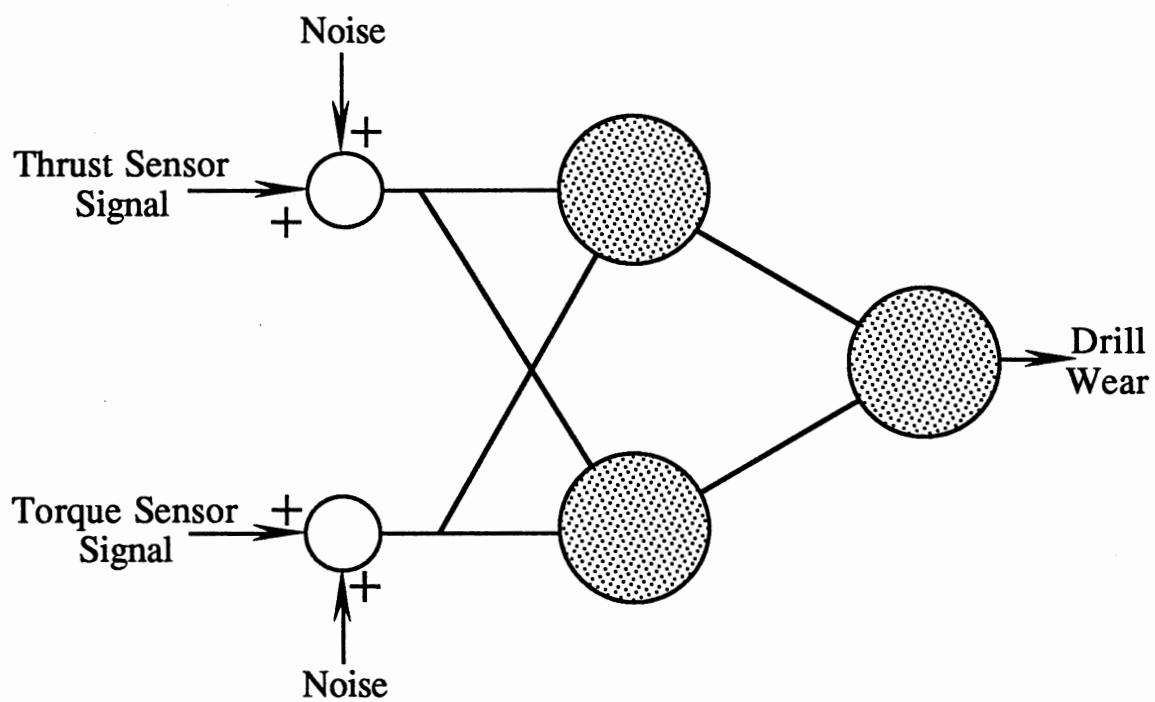
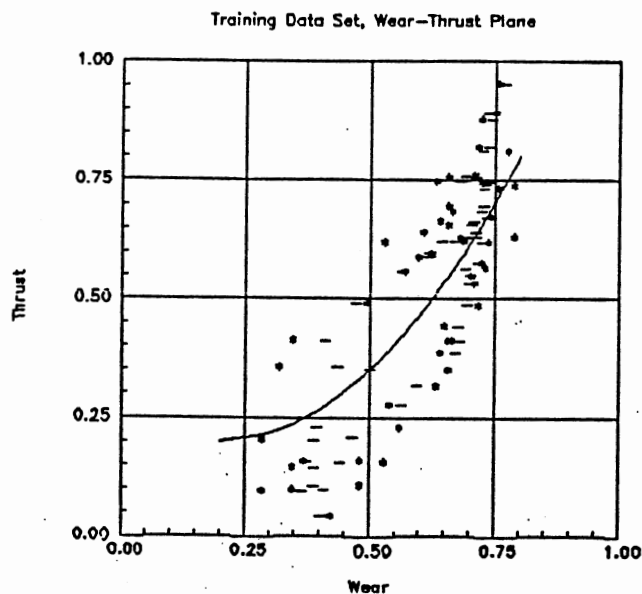
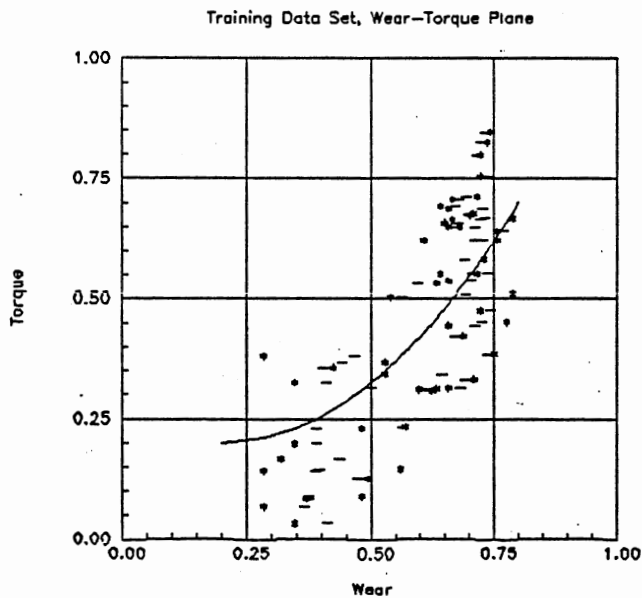


Figure 6.4 2x2x1 BP Neural Network Used for the Computer Simulation of Equations 6.6a and 6.6b.



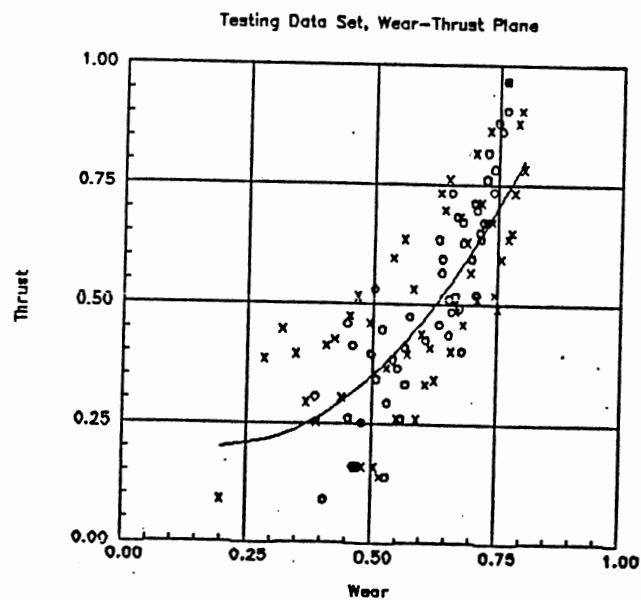
(I) Wear-Thrust Plane



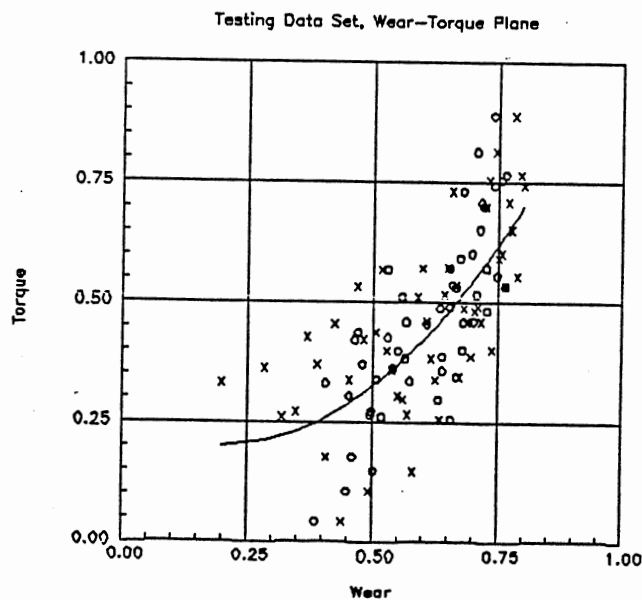
(II) Wear-Torque Plane

Figure 6.5a Simulation of Equations 6.6a and 6.6b Using  $2 \times 2 \times 1$  BP Neural Network for Training Data Set.

(I) Wear-Thrust Plane, (II) Wear-Torque Plane, (—) Equation 6.6a or 6.6b (\*) Training Data Set, (-) Response of Neural Network for Training Data Set.



(I) Wear-Thrust Plane



(II) Wear-Torque Plane

Figure 6.5b Simulation of Equations 6.6a and 6.6b Using  $2 \times 2 \times 1$  BP Neural Network for Testing Data Set.

(I) Wear-Thrust Plane, (II) Wear-Torque Plane, (—) Equation 6.6a or 6.6b (x) Testing Data Set, (o) Response of Neural Network for Training Data Set.

band of noise at any state of wear for training as well as testing data sets. This is because, as already mentioned, for any noisy values of thrust and torque signals at any state of drill wear, there are some values of  $C$  and  $m$  that can satisfy Equations 6.3b and 6.3c or other similar equations.

### 6.3 Possibility of Using Clustering, Decision Surfaces, and Mapping Techniques for Drill Wear Classification

Figure 6.6 shows two dimensional distribution of the estimate of power of thrust signal at 121.1 Hz and the estimate of power of torque signal at 101.6 Hz for each hole of Set 1, Set 4, and Set 7 of Figure 5.4. Set 1, Set 4, and Set 7 at three states of drill wear (total corner wear area: 0.076 mm<sup>2</sup>, 0.28 mm<sup>2</sup> and 0.43 mm<sup>2</sup> respectively) of drill BL (see Figure 5.4 and Section 5.5 for clarification). Estimate of the power of a sensor signal from one hole of each sensor is average of six periodograms of signals with a 50% overlap from that hole. In this section, for simplicity, whenever powers of thrust and torque signals of a hole is mentioned, they refer to the average of periodograms of six data segments of thrust and torque signals at the 121.1 Hz and 101.6 Hz respectively.

Figures 6.1a through 6.1c show that signal-to-noise ratio of powers of thrust and torque signals at all states of drill wear is about 2.2 for the average of six periodograms of sensor signals with a 50% overlap from one hole. This means that the standard deviation of the noise associated with the estimate of power of each sensor signal from one hole is about 0.48 times the mean of power of the sensor signal from each hole. Figure 6.2 shows that powers of thrust and torque are uncorrelated. If it is assumed that they are independent, then the joint probability distribution of powers of thrust and torque signals at each state of drill wear is a product of their probability distribution. For example, the joint probability distribution at 0.28 mm<sup>2</sup> total corner wear is

$$f_{0.28}(T,M) = f_{0.28}(T)f_{0.28}(M) \quad (6.7)$$

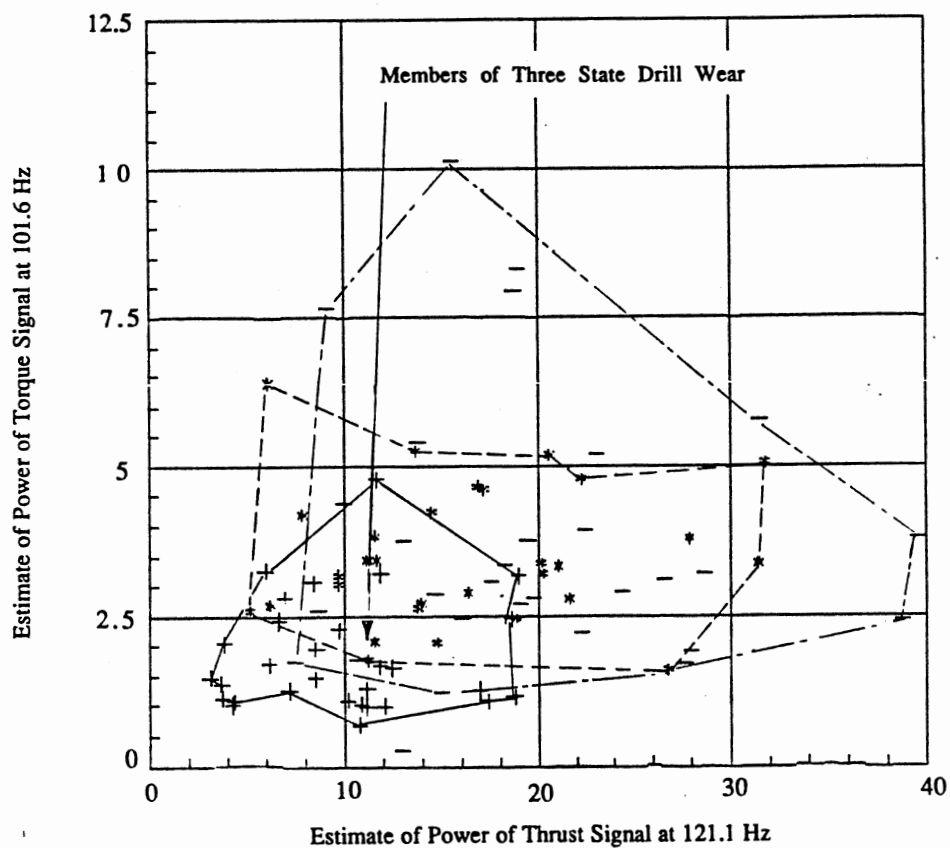


Figure 6.6 Two Dimensional Distributions of the Estimate of Power of Thrust Signal at 121.1 Hz and the Estimate of Power of Torque at 101.6 Hz for Each Hole of Set 1, Set 4, and Set 7 of Drill BL Shown in Figure 5.4. Estimate of Power of Sensor Signal is Average Periodograms of Six Data Segments with 50 % overlap from one Hole.

(+) Set 1,  $0.076 \text{ mm}^2$  total corner wear, (\*) Set 4,  $0.28 \text{ mm}^2$  total corner wear, (-) Set 7,  $0.43 \text{ mm}^2$  total corner wear. (—) Boundary of Set 1, (— —) Boundary of Set 4, (— · —) Boundary of Set 7.



where  $f_{0.28}(T)$ ,  $f_{0.28}(M)$ , and  $f_{0.28}(T,M)$  are probability distribution functions for thrust and torque signals and joint probability distribution function of thrust and torque signals at  $0.28 \text{ mm}^2$  total corner wear respectively. All three joint probability distribution functions at three states of drill wear cover the complete first quarter of the thrust-torque plane. In Figure 6.6, the outer elements of each set are connected together by straight lines. Definitely these lines are not the boundaries of three states of drill wear. The size of the three sets may reflect variance of the noise associated with each of them. Figure 6.6 shows Set 4 ( $0.28 \text{ mm}^2$  total corner wear) is larger than Set 1 ( $0.076 \text{ mm}^2$  total corner wear). And Set 7 ( $0.43 \text{ mm}^2$  total corner wear) is larger than the other two sets. This means that variance increases with increase in drill wear. It is expected, as shown earlier, the variance is about 0.48 mean of the power of thrust and torque.

Figure 6.6 shows that the any two sets among the three sets, namely Set 1, Set 4 and Set 7 have common domains. Therefore, it is not clear that a signal from a common domain of Set 4 and Set 7 belongs to which of these two sets. This is true also for the other domains that are common. Figure 6.6 illustrates a point that signals from all three states of drill wear are present. In this case, the state of drill wear can not be identified from the signal.

In the clustering technique no member of a subclass can be in the other subclass. Thus, each subclass may represent only one state of drill wear. Therefore, the common domains can not be divided into subclasses so that each subclass belongs to one state of drill wear.

In decision surfaces technique, all the members of one class must be bounded by a closed boundary and no member of the other class may be inside the closed boundary. The boundaries shown in Figure 6.6 contain elements from the other two sets.

Mapping technique cannot be used in drill wear classification because in common domain of all three states of drill wear, the target of the network should contain different values depending on the state of drill wear. For example, if we assume, the value  $a$  for Set

1, b for Set 4, and c for Set 7. The point shown in Figure 6.6 represents the signals from all three states of drill wear which imply all the three values a, b, and c to be the target of neural networks during training. But, only one value can be targeted at the same time during training which is explained in Section 3.3.2.

#### 6.4 Reevaluation of Some of the Previous Work on Sensor

##### Integration Using Neural Network

Application of neural networks to metal cutting was first proposed by Rangwala and Dornfeld [14, 15]. Work in this area was followed by other researchers, including Chryssolouris et al [38, 41] and others [43]. In this section, the results of Rangwala and Dornfeld [14,15] and Chryssolouris et al [38] will be discussed in line of the results of this research.

Rangwala and Dornfeld used BP network to classify sharp and worn tools in a turning operation on a lathe. The work material used was AISI 1060 steel bar 2 in. in diameter. Feed rate, depth of cut, and cutting speed were 0.002 ipr-0.008 ipr; 0.01-0.03 inch and 278-556 sfpm respectively. The state of tool wear was divided into two classes- sharp and worn tool. The wear land was considered to be 0-0.25 mm for a sharp tool, and for a worn tool 0.5-0.75 mm. No signal was collected between 0.25-0.5 mm wear land. Force and acoustic emission (AE) signals were sampled at the same time. Forces were sampled at a rate of 1 KHz for a length of 512 data points and AE at the rate of 5 MHz for a length of 1024 data points. PSD of the sensor signals (force and AE) was found by calculating the square of the absolute of FFT of the sensor signals. Therefore, the dimension of the force vector was 256 elements (with a resolution of 2 Hz) and for the AE vector 512 elements (with a resolution of 5 KHz). These two vectors were concatenated and made to a measurement vector of length of 768 elements.

As mentioned in Chapter IV, the square of the absolute of FFT of a sensor signal is not PSD, but a periodogram or a sample spectrum. As shown theoretically in Chapter IV

and experimentally in Chapter V, the standard deviation of the periodogram at each frequency is equal to or greater than the mean of periodograms of the same frequency. Mean of the periodograms at each frequency converges to PSD at that frequency. The author of investigation while not attempting to generalize this fact, introduces an element of doubt regarding the sampled data in Rangwala's work. As for the force signal, only one vector of length 512 elements and for the AE one vector of length 1024 data points were used at each state of the tool wear. One would expect a large standard deviation of the noise associated with periodograms of both of the signals. Therefore, it appears that these signals are not very reliable.

Rangwala [14] assumed that some frequencies of the measurement vector are more related to the tool wear than others. For selecting the most correlated signal, we attempted to minimize the interclass distance and maximize the distance of in-between classes, in an Euclidean space. The following cost function was used for this purpose

$$J = \text{trace} (S_w^{-1} S_b) \quad (6.8)$$

where  $S_w$  is within-class scattered matrix and  $S_b$  is between-classes scattered matrix.

If the average of the periodograms of AE and force signals of Rangwala's work have the same pattern as the results of the current investigation, i. e. the power is changing proportionately at all frequencies with change of wear, then, power at any one frequency has no particular advantage over the power at any other frequency with respect to change of drill wear, i. e. there is no need for feature selection.

Rangwala [14] collected 123 samples, each of length 768 frequencies of the periodograms of AE and force. Three sets of six features were selected, using the feature selection technique. For the first set, the concatenated vectors of force and AE were used and in the second set, three features from the force vector and three features from the AE vector were selected separately. In the third set, all the six features were selected from the

AE vector. To these six features, two more features were added, namely, cutting speed and feed. Therefore, the length of the feature vector came to 8. Out of the 123 total samples, 30 samples equally distributed between sharp and worn tools, were selected to train an  $8 \times 3 \times 1$  neural network. The remaining 93 samples were used for checking the neural network. During the training phase, the target of the output node was fixed at 0.01 for the fresh tool and 0.99 for the worn tool. A success rate of 95% was reported for the tool wear condition mentioned above and 100% when the network was trained to predict the actual wear (this case was not mentioned in Rangwala's Ph.D. Dissertation [14] but mentioned in a paper published in 1987 [15]).

As mentioned before, there appears to be no need for feature selection. A linear transformation applied in feature selection technique cannot reduce the variance of noise associated with the periodograms of sensor signals. As discussed in Section 6.3, integration of the noisy estimate of power at different frequencies of periodograms of sensor signals may not be possible because of presence of common regions of sensor signals that should be simultaneously mapped to 0.01 for sharp and 0.99 for worn tool respectively. As can be seen, Rangwala and Dornfeld mapped the signals from a sharp (0.01) to a worn tool (0.99). During testing of the network these values were changed to below 0.5 and above 0.5 for sharp and worn tool respectively. In their work wear land for a sharp tool is between 0 and 0.25 mm for a worn tool between 0.5 and 0.75 mm however, no signal was collected for the wear land between 0.25- 0.5 mm. If the output is between 0 and 0.5, they considered the signal to be associated with a sharp tool and if the output is greater than 0.5 then the signal is associated with a worn tool. i. e. there is no signal available for 0.25 to 0.5 mm tool wear. In practice it is impossible to separate the regions from a sharp to a worn tool. By imposing such extreme impractical constraints for the separation of noisy signals from a sharp to worn tool region, i. e. absence of signals from 0.25 to 0.5 mm tool wear, and change of mapping values during testing Rangwala claimed

a success rate of 95%. It is difficult to implement such a strategy in actual production conditions.

Chryssolouris and Domroese [38] made a computer simulation for the integration of the estimates of tool wear from three models based on three sensors, namely, force, temperature, and AE. In one of the simulations, they assumed that the models estimated appropriate tool wear except with some random noises which are represented by the following i. e.

$$x_i = y + \text{random} \quad i= 1, 2, 3 \quad (6.9)$$

where:

$x_i$  = estimate of tool wear by the model based on sensor i.

$y$  = actual tool wear

random = random noise.

The sensor integration can, then, be represented as (see Section 6.2 for details)

$$y = \frac{x_1 + c_2x_2 + c_3x_3}{1 + c_2 + c_3} \quad (6.10)$$

There are some noise associated with  $x_1$ ,  $x_2$ , and  $x_3$ . As mentioned in Section 6.2 there is no access to  $c_2$  and  $c_3$  from input. During training, for any values of  $y$ ,  $x_1$ ,  $x_2$ , and  $x_3$  some there will be some values for  $c_2$  and  $c_3$  that can satisfy the above equation. It means that neural network can converge to any values of  $y$ ,  $x_1$ ,  $x_2$ , and  $x_3$ . Such a sensor integration introduces redundancy in the sensor integrator and in presence of noise causes tool wear estimation to deteriorate.

## 6.5 Conclusion

In this section the necessity and possibility of sensor integration for drill wear monitoring was investigated. It was shown that PSD of three sensor signals, namely thrust, torque and strain in the X-direction have equally good correlation with drill wear. Therefore, there is no need for sensor integration and one sensor would be adequate for monitoring and controlling the drill wear.

The possibility of the application of three classification techniques, namely, classification using mapping, clustering and decision surfaces technique were examined. Integration of the sensor signals can introduce redundancy in the sensor integration technique and in the presence of noise, results in the deterioration of the estimation of drill wear. Periodograms of sensor signals at different states of drill wear are mixed and therefore it is difficult to apply the clustering technique. Also, it was shown that inside the closed boundary of any one state of drill wear there are signals from the other states of drill wear. Hence application of the decision surface technique may not be possible.

## CHAPTER VII

### CONCLUSIONS

In this thesis, the correlation between four sensor signals, namely, thrust, torque, and strains on the machine tool table in the cutting direction (X-direction) and perpendicular to the drill bit axis (Y-direction) in drilling had been investigated. This involved the study of sensor signals in the time and frequency domains. In the time domain, the mean and the variance of the signals were calculated. In the frequency domain, the power spectral densities (PSD's) of sensor signals were calculated using the Welch method. To find the most reliable frequencies of the sensor signals, signal-to-noise ratio analysis was carried out. From the PSD plots, power at frequencies with the highest signal-to-noise ratio (the most reliable frequencies) were used for the analysis. This chapter summarizes major conclusions of this study.

#### 7.1 Drill Wear

This investigation has reinforced the validity of the corner wear as the predominant mode of drill wear and can be used for drill life criterion, as proposed by other researchers [17-21]. This is due to the high temperatures generated in drilling (above the secondary hardening zone ( $>600^{\circ}\text{C}$ )), as reported by Thangaraj and Wright [19]. We have observed that in many cases one side of the drill to wear more than the other which was also noticed by Braun et al [32]. This might be due to geometrical errors in the manufacture of the drill bit as well as uneven hardness variation of the drills. Uneven hardness of drill bit, i. e. one side of the drill bits harder than the other can be due to the problems associated with heat treatments of a intricate shaped of drill bits. In this investigation, it was found that total

corner wear area, i. e. the summation of corner wear areas of both sides of the drill bit showed better correlation with the sensor signals than the width of the margin wear.

## 7.2 Correlation of the Sensor Signals With Total Corner Wear of the Drill

In the time domain, the mean and the variance of the sensor signals for each hole were calculated and plotted against the hole number (see Figures 5.6 and 5.7). Figure 5.4 shows that total corner wear for hole number 50 and hole number 250 are  $0.076 \text{ mm}^2$  and  $0.43 \text{ mm}^2$  respectively (see Section 5.6 for details of the calculation of total corner wear area). But, from Figures 5.6 and 5.7 no significant differences can be found in the mean and the variance of sensor signals for these two holes. Therefore, it can be concluded that sensor signals in the time domain do not show any correlation with drill wear.

To obtain the estimate of PSD, of one sensor signal from a hole, the average of periodograms of six data segments of the sensor signals with a 50% overlap was calculated. estimates of PSD of all sensor signals from one hole was found to be rather noisy. It was observed that had recommended cutting speed was used, wear development would be negligible over a number of holes (no significant change of wear was observed for 100 holes at least). The data for 100 holes, over which change of wear was negligible, was divided into three sets: set one for, the first 30 holes; set two for the next 40 holes; and set three for last 30 holes. To obtain the estimate of PSD, periodograms of all the holes for each of the mentioned sets were averaged for each sensor signal. To demonstrate the repeatability, the estimates of PSD of all the three sets for each sensor was plotted on the same graph for each sensor signal. It was observed that for each sensor, the estimate of PSD plots of all three sets are coincident. This procedure was repeated for various states of drill wear and a similar result was obtained.

To find the most reliable frequencies of the sensor signal, signal-to-noise ratio in the frequency domain for each frequency was calculated. It was observed that signal-to-



noise ratio is maximum for frequencies between 50 to 300 Hz for all sensor signals, and its magnitude is about 2.2. This value compares favorably with the theoretical value calculated for the average of periodograms of six data segments with a 50% overlap.

It was observed that estimate of power of the sensor signals between 50 and 300 Hz (shown on the estimate of PSD plots) increases with increase in drill wear. It is well known that integration decreases the error. Therefore, the change of area under the PSD plots for all sensor signals was plotted against the total corner wear for a given drill bit. These plots showed that change of area under the PSD plots of three sensor signals, namely, thrust, torque, and strain in the X-direction all had good correlation with the drill wear. Correlation between the change of area under the PSD plots of the strain in the Y-direction and drill wear was found to be not as good as the other three sensors.

### 7.3 Parameters of the System

The estimates of PSD of the sensor signals for the three sets of holes at different states of drill wear were plotted on the same plot. Examination of each plot indicated that there should be proportional change of estimate of PSD at each frequency for all sensor signals. The estimate of PSD plots of all four sensors at different states of drill wear were normalized for each sensor. This is accomplished by proportional change of the estimate of power at each frequency, by considering the area under each PSD plot between 20 to 380 Hz as unity. It was observed that the normalized PSD plots of each sensor signal for all three sets of holes at different states of drill wear were coincident. This indicates that all parameters of the system, except for the gain of the system, are the same at different states of drill wear. The proportional change at each frequency can be attributed a change in the gain of the system or inputs to the drilling process, namely, the actual cutting speed and the feed rate.

## 7.4 Sensor Integration

In this investigation potential problems associated with sensor integration were investigated from two different view points- necessity and possibility of sensor integration.

As observed, the PSD's of three sensor signals, namely, thrust, torque, and strain in the X-direction all showed good correlation with drill wear. It, therefore, appears that information from one sensor signal would be adequate for drill wear estimation and hence there may not be any need for multiple sensors and their integration.

Cross correlations in the frequency domain were found, at two different frequencies for one sensor or for two different sensors at any two frequencies (0-425 Hz). The results showed that noises at any two different frequencies of the same sensor or different sensors at two different frequencies are uncorrelated. Signal-to-noise ratio analyses in the frequency domain at different states of drill wear were also carried out. It was found that at different states of drill wear, the signal-to-noise ratio for all sensor signals to be about 2.2. As mentioned in Section 7.2, power at each frequency increases with increase of drill wear. Therefore, noise in the frequency domain increases with increase of drill wear.

The possibility of sensor integration by these methods, and classification using mapping, clustering, and decision surfaces techniques were also investigated. Integration of the sensor signals using a mapping technique (for classification of sharp and worn tool) adds redundancy to the sensor integration technique. It was shown that in the presence of redundancy and high variance (the same order as mean of the signal) uncorrelated noise results in deterioration of the correct estimation of drill wear. The same problem was observed for estimation of drill wear using the mapping technique.

Clustering technique was not found to be applicable for the present investigation. In Chapter 3, Section 3.3.1 the principles of clustering technique were discussed. When two signals, such as thrust and torque were plotted for a sharp, a worn, and a fractured tool, it was assumed that within a class of each state of wear subclasses (clusters) may be

formed separate from the signals for the other states of wear. Figure 6.6 shows a plot of the experimental results. It can be seen that points corresponding to each state of drill wear was not clearly separated. A point in this graph may, therefore, belong to any state of drill wear. The same problem was observed for the estimation of drill wear using the clustering technique. Decision surfaces technique did not also work because it was not possible to separate signals by a boundary from two states of drill wear.

## CHAPTER VIII

### FUTURE WORK

Based on the results of this investigation the following research is proposed for future investigation.

#### 8.1 Characteristics of the Actual Cutting Speed and Feed in the Time and Frequency Domains

As discussed in Section 5.1.1 and shown in Figure 5.3, the actual cutting speed and feed during drilling can be lower than the reference cutting speed and feed due to resisting torque and thrust respectively. As mentioned in Section 5.5, the powers at all frequencies are increasing proportionally with respect to the increase in drill wear. Therefore, all the parameters of the system are constant, the increase in power can be due to the combined effect of input signals to the drilling process and change in the gain of the system. Based on the literature review, it appears that the characteristics of the input signals (actual cutting speed and feed) have not been investigated. The time and frequency domains characteristics of actual cutting speed and feed may show a much better correlation to drill wear than the output signals, such as torque and thrust, and other signals such as strains in the X- and Y-directions on the table of the machine tool.

#### 8.2 Transfer Function of the Drilling Process

As shown in Figure 5.3, the drilling process has two inputs- actual feed and cutting speed, and two outputs- thrust and torque. As mentioned in the last section, only the outputs of this process have been investigated. Therefore, transfer function of this process

between inputs and outputs has not been studied due to lack of information regarding the actual cutting speed and feed signals. Transfer function of the drilling process can be obtained using the power spectral density (PSD) of the inputs, namely, actual cutting speed, and feed, and outputs, namely, torque and thrust of the drilling process. The effect of any of the inputs- actual cutting speed and feed, on both outputs- torque and thrust, can be studied. This study should provide a better appreciation of cutting in the drilling process and the effect of drill wear on the process parameters.

### 8.3 Drill Wear Pattern at Recommended Cutting Conditions

In this investigation high speed cutting (twice the recommended cutting speed) was used for accelerating drill wear. Therefore, data presented in this report regarding the patterns of tool wear are valid for the wear pattern obtained using high cutting speed. Wear patterns in drilling for normal cutting speed need to be studied. This has not been documented in the open literature because drill life would be of the order of thousands of holes which may not be feasible in a laboratory environment.

In this study we observed uneven wear on the two sides of the drill at high cutting speed (during accelerated drill wear). A similar observation was reported by other researchers also [32] for high speed drilling. It is not clear if a similar phenomenon is present at the recommended cutting conditions. The temperature distribution on the corner of the drill was obtained by Thangaraj and Wright [19] for the cases where the cutting speed was 40 to 66 m/min, which is approximately two to three times the recommended cutting speed (23 m/min) given in the Machining Data Hand Book [45]. Therefore, for recommended cutting conditions, no information regarding the distribution of temperature on the corner of the drill bit is available. Temperature plays a very significant role in tool wear of HSS tools. This is especially so when the temperature exceeds the secondary hardening temperature ( $600^{\circ}\text{C}$ ) of the HSS tool material. Such a study is necessary because even if the margin on one side of the drill wears, the drill bit has to be replaced.

#### 8.4 Monitoring Sensor Signals at Conventional Drilling Speed

In this investigation monitoring of sensor signals was done at the conventional drilling speeds but wear was accelerated intentionally to accomplish different levels of wear by increasing the drilling speed to twice the recommended value. This approach was taken to limit the number of holes to be drilled and consequently the cost of the work material. However, wear under accelerated conditions will be different from gradual wear. In practice, drilling is conducted at the recommended speeds and the wear will be under more normal conditions. It would, therefore, be useful to investigate the correlation of drill wear with sensor signals at the recommended drilling speeds. This could be cost limited in an university setting. Hence, such a study should be conducted in an industrial environment, e. g. aerospace industry, where they routinely drill literally millions of holes.

## REFERENCES

1. Shaw, M. C., "Metal Cutting Principles", Calrendom Press, Oxford, (1984).
2. -----, "Metalworking Trends", American Machinist, 128/8 (1984), 29.
3. Groover, M. P., "Automation, Production Systems, and Computer Aided Manufacturing", Prentice-Hall, Inc., Englewood Cliffs, NJ, (1980).
4. Koren, Y., "Computer Control of Manufacturing Systems", McGraw Hill Book Company, New York, N .Y., (1983).
5. Merchant, M. E., "Mechanics of the Metal Cutting Process. I. Orthogonal Cutting and a Type 2 Chip.", Journal of Applied Physics, 16/5 (1945),
6. Subramanian, K. and N. H. Cook, "Sensing of Drill Wear and Prediction of Drill Life", J of Engg. for Ind., 101 (1977), 295-301.
7. -----, "Sensors: the Eyes and Ears of CIM", American Machinist, 127/7 (1983), 109-124.
8. Micheletti, G. F., "In Process Tool Wear Sensors for Cutting Operations", Annals of the CIRP, 25/2 (1976),
9. Tlusty, J. and G. C. Andrews, "A Critical Review of Sensors for Unmanned Machining", Annals of the CIRP, 32/2 (1983), 563-572.
10. Kannatey-Asibu, E., "On the Application of the Pattern Recognition Method to Manufacturing Process Monitoring", NAMRC-X, (1982), 487-492.
11. Dornfeld, D. and C. S. Pan, "Determination of Chip Forming States Using a Linear Discriminant Function With Acoustic Emission", NAMRC-XIII, (1985), 299-303.
12. Emel, E. and E. Kannatey-Asibu, "Characterization of Tool Wear and Breakage by Pattern Recognition Analysis of Acoustic Emission Signals", NAMRC-XIV, (1986), 266-276.
13. Emel, E. and E. Kannatey-Asibu, "Tool Failure Monitoring by Pattern Recognition Analysis of AE Signals", J of Engg. for Ind., 110 (May 1988), 137-145.
14. Rangwala, S., "Machining Process Characterization and Intelligent Tool Condition Monitoring Using Acoustic Emission Signal Analysis", Ph.D. Dissertation, University of California at Berkeley, (1988).

15. Rangwala, S. and D. Dornfeld, "Integration of Sensors via Neural Networks for Detection of Tool Wear States", Intelligent and Integrated Manufacturing Analysis and Synthesis, ASME Winter Annual Meeting, (Dec 13-18 , 1987), 109-120.
16. Brinksmeier, E., "Prediction of Tool Fracture in Drilling", Annals of CIRP, 39/1 (1990), 97-100.
17. Soderberg, S., Vingsbo, O. and M. Nissle, "Performance and Failure of High Speed Steel Drills Related to Wear", Proceedings of the International Conference Wear and Materials, San Francisco, (March-April 1981), 456-467.
18. Kanai, M. and Y. Kanda, "Statistical Characteristics of Drill Wear and Drill Life for the Standardized Performance Tests", Annals of the CIRP, 27/1 (1978), 61-66.
19. Thangaraj, A., Wright, P. K. and M. Nissle, "New Experiments on the Temperature Distribution in Drilling", J of Engg. for Ind., 106 (July 1984), 242-247.
20. Lenz, E., Mayer, J. E. and D. G. Lee, "Investigation in Drilling", Annals of CIRP, 27/1 (1978), 49- 53.
21. Kaldor, S. and E. Lenz, "Investigation in Tool Life of Twist Drills", Annals of CIRP, 29/1 (1980), 23-27.
22. Yee, K. W., "On the Use of Drill-Up for On-Line Determination of Drill Wear", NAMRC-XIII, (1985), 33-39.
23. Yee, K., W. and D. S. Blomquist, "Checking Tool Wear by Time Domain Analysis", J of Manuf. Engg., 88 (May 1982), 74- 76.
24. Thangaraj, A. and P. K. Wright, "Modeling Computer-Assisted Prediction of Drill-Failure Using In-Process Measurements of Thrust Force", Sensing and Control of Manufacturing Processes, ASME Winter Annual Meeting, (1986), 303-322.
25. Williams, R. A., "A Study of the Drilling Process", J of Engg. for Ind., 98 (1974), 1207-1215.
26. Armarego, E. J. A. and R. H. Brown, "The Machining of Metals", Prentice Hall, Englewood Cliffs, New Jersey, (1969).
27. Eggleston, D. M., Herzog, R. and E. G. Thomsen, "Observation on the Angle Relationships in Metal Cutting", J of Engg. for Ind., 81 (1959), 263-279.
28. Boothroyd, G., "Fundamentals of Metal Machining and Machine Tools", McGraw Hill, New York, NY, (1975).
29. Wright, P. K. and E. M. Trent, "Metallographic Methods for Determining Temperature Gradient in Cutting Tools", Journal of the Iron and Steel Institute, 211 (1973), 364-368.
30. Liu, T. I., "Automated Visual Inspection of Drill Wear", Proceedings of Manufacturing International, 5 (1990), 115- 119.



31. Amini, E. and R. H. S. Winterton, "Measurement of Wear of Twist Drills", Proceedings of Institution of Mechanical Engineers, 195 (1981), 241-249.
32. Braun, S., Lenz, E. and C. L. Wu, "Sensing of Drill Wear and Prediction of Drill Life", J of Engg. for Ind., 104 (April 1982), 268-276.
33. Moriwaki, T., "Detection of Cutting Tool Fracture by Acoustic Emission Measurement", Annals of CIRP, 29/1 (1980), 35.
34. Radhakrishnan, T. and S. M. Wu, "On-Line Hole Quality Evaluation for Drilling Composite Material Using Dynamic Data", J of Engg. for Ind., 103 (1981), 119-125.
35. Fabris, N. S. and P. K. Podder, "Optimization of Drill Life: Part 1: Influence of Cutting Conditions on Tool Wear", NAMRC-X, (1982), 337- 341.
36. Nedess, C. and T. Himburg, "'Drilling Dynamics - A Fundamental Base for Drill-Life Monitoring.'", NAMRC-XVI, (1988), 300-306.
37. Chryssolouris , G., Guillot, M. and M. Domroese, "An Approach to Intelligent Machining", Proceedings of the American Control Conference, 1 (1987), 152-160.
38. Chryssolouris, G. and M. Domroese, "Sensor Integration for Tool Wear Estimation in Machining", Sensors And Controls for Manufacturing, ASME Winter Annual Meeting, (Nov. 27- Dec. 2 1988), 115-123.
39. Chryssolouris, G. and M. Guillot, " An A. I. Approach to Selection of Process Parameters in Intelligent Machining", Sensors and Controls for Manufacturing, ASME Winter Annual Meeting, (Nov. 27- Dec 2 1988), 199-206.
40. Chryssolouris, G., Domroese, M. and P. Beaulieu, "Sensor Synthesis for Control of Manufacturing Processes", Automation of Manufacturing Processes, ASME Winter Annual Meeting, (Nov. 25-30,1990),
41. Tansel, I. N. and C. Mclaughlin, "On Line Monitoring of Tool Breakage With Unsupervised Neural Network", (1991), 364-370.
42. Elanayar, V. T., Shin, Y. C. and S. Kumara, "Machining Condition Monitoring for Automation Using Neural Networks", ASME Winter Annual Meeting, PED-VOL 44 (1990), 85-95.
43. Kamarthi, S. V., Sankar, G. S., Pool, H., Cohen, S. and R. T. Kumara, "On-Line Tool Wear Monitoring Using a Kohonen's Feature Map", in "Intelligent Engineering Systems Through Artificial Neural Networks", Dogli, C. H., Kumara, R. T. and Shin, Y. C. Eds., (1991), ASME press,
44. Lippmann, R. P., "An Introduction to Computing With Neural Nets", IEEE ASSP Magazine, (April 1987), 4- 22.
45. -----, "Machining Data Hand Book", METCUT Research, Cincinnati, OH, (1980).

46. Liang, S. Y. and D. A. Dornfeld, "Detection of Cutting Tool Wear Using Adaptive Time Series Modeling of Acoustic Emission Signal", Proceedings, Symposium on Sensor for Manufacturing, ASME Winter Annual Meeting, Boston,, (December 1987), 27-38.
47. Takata, S., Ogawa, M., Bertok, P., Ootsuka, J., Matushima, K. and T. Sata, "Real-Time Monitoring of Tool Breakage Using Kalman Filtering.", Robotics and Computer Integrated Manufacturing, 2/1 (1985), 33-40.
48. Astrom, K. J. and B. Wittenmark, "Computer Controlled Systems", Prentice Hall, Inc., Englewood Cliffs, N. J., (1984).
49. Tou, J. T. and R. C. Gonzalez, "Pattern Recognition Principles", Addison-Wesley, Reading, Massachusetts, (1981).
50. Carpenter, G. and S. Grossberg, "ART2: Self-Organization of Stable Category Recognition Codes for Analog Input Pattern", Applied Optics, 26 (1987), 4919-4930.
51. Grossberg, S., "Adaptive Pattern Classification and Universal Recording: II. Feedback, Oscillation, Olfaction and Illusions", Biological Cybernetics, 23 (1976), 188-207.
52. Hartigan, J. A., "Clustering Algorithms", John Wiley and Sons, New York, NY, (1975).
53. Simpson, P. K., "Artificial Neural Network", Pergamon Press, New York, N. Y., (1990).
54. Rumelhart, D. E., Hinton, G. E. and R. J. Williams, "Learning Internal Representations by Error Propagation", in "Parallel Distributed Processing: Explorations In Microstructure Of Cognition. Vol. 1: Foundations", Rumelhart, D. E. and J. L. McClelland Eds., (1986), MIT Press,
55. Hecht-Nielsen, R., "Neurocomputing", Addison-Wesley, Reading, Massachusetts, (1990).
56. Papoulis, A., "Probability, Random Variables and Stochastic Processes", 2nd ed., McGraw-Hill Book Company, New York, NY, (1984).
57. Oppenheim, A. V. and R. W. Schaffer, "Discrete-Time Signal Processing", Prentice Hall, Englewood Cliffs, New Jersey, (1989).
58. Welch, P. D., "The Use of Fast Fourier Transform for the Estimation of Power Spectra: A Method Based on Time Averaging Over Short, Modified Periodograms", IEEE Transactions on Audio and Electroacoustics, AU-15 (June 1967), 70-73.
59. Bartlett, M. S., "An Introduction to Stochastic Processes with Special Reference to Methods and Applications", 2nd ed., Cambridge University Press, Cambridge, (1966).
60. Welch, P. D., "A Direct Digital Method of Power Spectrum Estimation", IBM J of Res. and Dev., 5 (1961), 141-156.

61. Rotberg, J., Lenz, E. and S. Braun, "Vibration Based Drill Wear Monitoring", *ASME Manufacturing Review*, 3/1 (1990),
62. Balakrishnan, P., Trabelisi, H., Kannaty-Asibu, E. and E. Emel, "A Sensor Function Approach to Cutting Tool Monitoring", 101-108.
63. Chryssolouris, G. and M. Domroese "An Experimenting Study of Strategies for Intelligent Sensor Information in Machining", *Annals of CIRP*, 38/1 (1989), 425-428.

## APPENDIX

### EQUIPMENT SPECIFICATIONS

#### A.1 Machine Tool

Type	Interact 412 Bridgeport CNC Vertical Machining Center
Working Surface	840 mm X 320 mm
Travel Along the X Axis (Table)	450 mm
Travel Along the Y Axis (Saddle)	310 mm
Travel Along the Z Axial (Spindle)	300 mm
Feed Rate Range (Z Axis)	1 to 7.5 m/min
Feed Rate Range (XY Axis)	1 to 12 m/min
Spindle Motor Power	3.7 KW
Spindle Speed Range	40 to 4000 rpm
Spindle Diameter	65 mm
Taper	BT 40
Control	Heidenhain TNC 151P

#### A.2 Two Component (Thrust and Torque)

##### Drilling Dynamometer

Type	Kistler 9271A
Thrust Range	-5 to 20 KN

Torque Range	-100 to 100 Ncm
Linearity	$\leq \pm 1 \%$
Natural Frequency	$\geq 3$ KHz
Axial Rigidity (Thrust Direction)	4 KN/ $\mu$ m
Torsional Rigidity (Torque Direction)	50 Ncm/ $\mu$ rad
Axial Sensitivity (Thrust Direction)	-1.8 pC/N
Torsional Sensitivity (Torque Direction)	-1.5 pC/Ncm

### A.3 Piezoelectric Strain Element

Type	Kistler 9233B
Range (Relative Strain)	-300 to 300 $\mu$ $\epsilon$
Linearity	$\leq \pm 1 \%$
Natural Frequency	$\geq 4$ KHz
Rigidity	$\sim 1.5$ N/ $\mu$ $\epsilon$
Torsional Sensitivity (Torque Direction)	$\sim 6$ pC/ $\mu$ $\epsilon$

### A.4 Charge Amplifiers

Type	Kistler 5004
Input Impedance	70 Ohms
Output Voltage	$\pm 10$ V
Output Current	$\leq \pm 5$ mA
Output Impedance	100 Ohms
Frequency Range	0 to 180 KHz
Time Constant	1000 to 100000 sec (Long) 1 to 5000 sec (Medium) 0.01 to 50 sec (Short)
Accuracy of Ranges	$\leq \pm 1 \%$

Linearity  $\leq \pm 0.05\%$

#### A.5 Data Acquisition Board

Type	MetraByte DAS-16
Sampling Rate	50000 Sample/Second
No. of A/D Channels	16 Single Ended/8 Differential Analog Input.
A/D Resolution	12 Bits
A/D Input Rang	$\pm 10\text{ V}$ , $\pm 5\text{ V}$ , $\pm 2.5\text{ V}$ , $\pm 1\text{ V}$ 0-10 V, 0-5 V, 0-2 V
Input Current	250 $\mu\text{A}$ max. at 25° C
Accuracy	0.01% of Reading, $\pm 1\text{ Bit}$
No. D/A Channels	2
D/A Resolution	12 Bits
D/A Output Range	0-5 V
Maximum Output Current	5 mA
No. Digital I/O Channels	8 (4 Input, 4 Output)

~  
VITA

Ali Noori-Khajavi

Candidate for the Degree of

Doctor of Philosophy

**Thesis:** FREQUENCY AND TIME DOMAIN ANALYSES OF SENSOR SIGNALS IN A DRILLING PROCESS AND THEIR CORRELATION WITH DRILL WEAR

**Major Field:** Mechanical Engineering

**Biographical:**

**Personal Data:** Born in Isfahan, Iran, April 21, 1952, The son of Jafar and Gohar Noori-Khajavi

**Education:** Graduated from Hadaf High School, Tehran, Iran, In June 1970, received Bachelor of Science Degree in Mechanical Engineering and Master of Science Degree in Structural Engineering from Amirkabir University of Technology (Tehran Polytechnic) in Feb, 1975 and Feb. 1982 respectively; completed requirements for the Doctor of Philosophy at Oklahoma State University in Dec., 1992

**Professional Experience:**

- 5/90-12/92 Research Assistant at Oklahoma State University.
- 1/88 - 5/90 Teaching Assistant at Oklahoma State University for "Mechanisms".
- 2/82 - 6/86 Design Engineer at Iranian Research Organization for Science and Technology (IROST). Projects: Design of Unit Type Machine Tools (Drilling, Tapping, Milling Units) Indexing Tables and Transfer Lines for Small Machine Parts.
- 2/82 - 6/86 Part Time Teaching at Tehran School of Aeronautic Engineering. Subjects: Statics, Strength of Materials and Theory of Machine (Kinematic and Dynamic of Machine.)
- 5/77 - 6/79 Design Engineer at Jovan Consultant Engineering Co. Projects: Piping Engineering projects including Gachsaran Gas Gathering System, Tehran Rasht Piping System for Transferring of Products of Tehran Refinery to Rasht, and Maron Production Unit